Design of Biomimetic Compliant Devices for Locomotion in Liquid Environments

by

Pablo Valdivia y Alvarado

B.S., Mechanical Engineering
Massachusetts Institute of Technology, 1999

M.S., Mechanical Engineering
Massachusetts Institute of Technology, 2001

Submitted to the Department of Mechanical Engineering
in partial fulfillment of the requirements for the degree of

Doctor of Philosophy in Mechanical Engineering

at the

MASSACHUSETTS INSTITUTE OF TECHNOLOGY
[February 2007]
January 2007

Author .....
Department of Mechanical Engineering
January 11, 2007

Certified by .....
Kamal Youcef-Toumi
Professor of Mechanical Engineering
Thesis Supervisor

Accepted by .....
Lallit Anand
Chairman, Department Committee on Graduate Students

Design of Biomimetic Compliant Devices for Locomotion in Liquid Environments

by

Pablo Valdivia y Alvarado

Submitted to the Department of Mechanical Engineering
on January 11, 2007, in partial fulfillment of the
requirements for the degree of
Doctor of Philosophy in Mechanical Engineering

Abstract

Presently, there is a need for devices capable of autonomous locomotion in liquid environments. Humanitarian, industrial and defense applications are numerous and include examples such as search and rescue missions, ocean exploration, and de-mining operations. Due to the nature of the environments involved, the required devices must overcome several challenges. The main challenges are related to hardware performance in terms of propulsion efficiency, mechanical robustness, maneuverability, adaptability, stealth and autonomy.

Current traditional approaches that use propeller driven devices have limited success in addressing these challenges. As a result devices that mimic fish-like swimming techniques have emerged as a promising alternative that can provide additional maneuvering features and the promise of improved performance. However, the inherent problems of current biomimetic devices have been identified as: (i) mechanical complexity due to the use of discrete and rigid components, and (ii) lack of a systematic design approach. These problems limit the practical implementation of biomimetic techniques in real mission environments.

This thesis presents an alternative approach for implementing biomimetic fish-like swimming techniques by exploiting natural dynamics of compliant bodies. The resultant devices are simpler and more mechanically robust than traditional biomimetic devices. Models are developed to express both the swimming kinematics and the corresponding swimming performance of the proposed devices, in terms of material, actuation and geometry design parameters. Design methodologies that identify the required prototype design parameters for a given target performance are proposed. The designs for caranguiform and thunniform type swimming devices are presented and their performance is characterized experimentally. Predictions based on an elongated body theory model that uses a second order approximation for the body kinematics display good agreement with prototype performance. Finally, the performance limits and the sensitivity to changes in design parameters are shown to be related to the

second order system approximation of the body kinematics.

Thesis Committee Members:
Woodie C. Flowers, Pappalardo Professor of Mechanical Engineering
Julio Guerrero, Senior Research Scientist, Schlumberger-Doll Research
Michael S. Triantafyllou, Professor of Mechanical and Ocean Engineering
Kamal Youcef-Toumi, Professor of Mechanical Engineering (Chairman)

Thesis Supervisor: Kamal Youcef-Toumi
Title: Professor of Mechanical Engineering

Acknowledgments

I would like to thank my thesis supervisor, Professor Kamal Youcef-Toumi, for his advice, support, guidance and friendship during my time at the Mechatronics Research Laboratory.

I thank the members of my thesis committee: Prof. W. Flowers, Dr. J. Guerrero, and Prof. M. Triantafyllou for providing invaluable insight during the preparation of this thesis. I am also extremely grateful to Prof. E. Blanco for his continuous help, encouragement, and advice.

My time at the Mechatronics Research Laboratory has been both enjoyable and stimulating, and for this I would like to thank my lab mates: Osamah El Rifai, Namik Yilmaz, Pradya Prempraneerach, Dan Burns, Mauricio Gutierrez, Vijay Shilpiekandula and Khalid El Rifai. I would also like to acknowledge two great UROP students: Anirban Mazumdar and Adam Kaczmarek, for their help, contributions, and for sharing my excitement for the project.

I am thankful to Schlumberger and the MIT Singapore Alliance (SMA) for partially funding this project, without their support the project could not have started.

I thank Mark Belanger and Gerry Wentworth for their support in the LMP shop, I am grateful for their patient and thorough instruction.

Most of all, I thank my parents Pablo and Jenny, my sister Paula, and my brother Miguel for their continuous support and encouragement. Belita y Gladis, gracias por haberme ayudado a crecer.

Finally, I thank Chiara for her constant love and for the happiness she has brought to my life.

Para mis Padres

Contents

1 Introduction **19**

1.1 Need and Challenges of Autonomous Locomotion in Liquid Environments 19

1.2 Why Biomimetic Locomotion Using Compliant Mechanisms? 21

1.3 Objectives, Scope and Overview of the Thesis 24

2 Background **27**

2.1 Fish Swimming Performance 27

2.2 Modeling Fish Swimming Performance 30

2.2.1 Fish Swimming Kinematics 30

2.2.2 Fish Swimming Dynamics 31

2.3 Biomimetic Mechanisms 35

2.3.1 Fish-like Devices 35

2.3.2 Foil Propelled Devices 37

2.4 Limitations of Current Approaches 37

2.5 Summary 38

3 Compliant Biomimetic Devices **39**

3.1 Exploiting Natural Vibrations 39

3.2 Lateral Vibrations of Slender Bodies 41

3.2.1 Internal Dynamics 42

3.2.2 Coupling to External Fluid Mechanics 45

3.2.3 Analysis 47

3.3 Swimming Performance 50

3.4 Performance Limits and Sensitivity to Parameter Changes 52
3.5 Model Refinements 54
3.6 Summary 55

4 Design Methodologies **57**
4.1 Objectives and Problem Definition 57
4.2 Target Performance 59
4.2.1 Thunniform Swimmers 60
4.2.2 Caranguiform Swimmers 62
4.2.3 Target Performance Summary 63
4.3 Design Methodologies 64
4.3.1 Approach 1: Bulk Approximation 64
4.3.2 Approach 2: Computed Rigidity 65
4.3.3 Approach 3: Lumped Parameters 73
4.4 Summary 75

5 Prototype Designs and Fabrication **77**
5.1 Prototype Designs 77
5.1.1 Actuation Mechanism 79
5.1.2 Compliant Bodies 81
5.1.3 Control Hardware 86
5.2 Fabrication Techniques 88
5.3 Summary 92

6 Performance Characterization **93**
6.1 Objectives 93
6.2 Material Properties 94
6.3 Prototype Kinematics 98
6.3.1 Experimental Setup 98
6.3.2 Measurements 100
6.4 Prototype Swimming Performance 105

6.4.1 Experimental Setup 105
6.4.2 Measurements 108
6.4.3 Performance Sensitivity 118
6.5 Summary 120

7 Conclusions and Recommendations **121**
7.1 Thesis Contributions 123
7.2 Recommendations for Future Work 125

A Elongated body theory **127**
A.1 Derivations 127
A.1.1 Assumptions 127
A.1.2 Performance 127

B Beam theory **133**
B.1 Viscoelastic Timoshenko beam theory (VTBT) 133
B.2 Green function solutions 135

C Matlab code **143**

D Parts and Materials Suppliers **159**
D.1 RC Components 159
D.2 Control Hardware 159
D.3 Elastomer materials 159
D.4 Sensors and Machine Elements 160

List of Figures

1-1 Typical long range AUV example (inspired by [3, 4]): (a) Front view, (b) Side view, (c) Back view, (d) Characteristic turning radius. 21

1-2 Highly maneuverable AUV example (inspired by [5]): (a) Side view, (b) Front view, (c) Top view, (d) Maneuvering capabilities. 22

1-3 Vegetation and debris challenges in natural liquid environments: Propeller driven vehicles risk tangling when moving through environments with debris and vegetation. 22

1-4 Biomimetic devices design problem. 24

2-1 Fish swimming velocity scaled to body length (data from [6]). 29

2-2 Reference frame and variables used to describe fish swimming kinematics. 30

2-3 Traditional biomimetic fish design. Body mechanism is composed of a hyper-redundant manipulator. The body links are driven either in a direct drive configuration or through pulleys and cables connected to actuators (not shown) located at a particular section in the body (inspired by [34, 35]): (a) Skin covering internal mechanism. (b) Hyper-redundant manipulator spine. 36

3-1 Using body natural modes of vibration: (a) Compliant visco-elastic fish-like body at rest. (b) Compliant visco-elastic fish-like body exited by a concentrated moment. 40

3-2 Top and side views of fish-like compliant body of length ℓ. Geometry and material properties are defined by depth $b(x)$, cross-sectional area $A(x)$, second moment of inertia $I(x)$, modulus of elasticity $E(x)$, viscosity $\mu(x)$, and density $\rho(x)$ which are all functions of x. A concentrated moment of magnitude M and frequency Ω is applied at a distance a from the nose. As a result body undulations of wavelength λ travel from nose to tail at a velocity V. Body undulations propel the body at an average velocity U. 41

3-3 Lumped parameter model of posterior body section. 49

3-4 Elongated-body swimmer subsystems. 52

3-5 Addition of concentrated masses in the body model. 54

4-1 Relations between unknown design parameters E, μ, M, a, swimming kinematics variables H, κ, and corresponding swimming performance parameters U, T, η. 59

4-2 Scaled amplitude envelope $\left(\frac{H}{\ell}\right)$ for thunniform swimming kinematics (based on experimental results from [14, 15]). 61

4-3 Scaled amplitude envelopes $\left(\frac{H}{\ell}\right)$ for caranguiform swimming kinematics at different swimming velocities (based on experimental results from [16]). 62

4-4 Curve fitting approach. The lateral body deflections $h(x,t)$ of a compliant fish-like body can be expressed in terms of actuation, material, and geometric properties. This model of lateral body deflections can then be compared to the required lateral body deflections $h_{fish}(x,t)$. The required actuator, material, and geometrical properties can then be found by minimizing the errors between the lateral deflection and required deflection. 65

4-5 Required bulk material properties E and μ versus swimming frequency f and body length ℓ. Uninform geometry case. 66

4-6 Geometries of thunniform and caranguiform bodies based on models in Equations (4.7) and (4.8). 69
4-7 Required material distribution for thunniform fish ($\kappa = \frac{2\pi}{1.1\ell}$). 69
4-8 Required material distribution for caranguiform fish ($\kappa = \frac{2\pi}{1.1\ell}$). 70
4-9 Graphical representation of inequality system defining the conditions for real positive values for $E(x)$ and $\mu(x)$. Gray region defines acceptable solutions. Scaled values for N and G are included to visualize the inequality sign changes. 71
4-10 Vector relationship in forced vibration of fish-like elongated body. (a) Small phase lag. (b) Resonance, 90° phase. (c) Increasing phase lag. . 71
4-11 Cross-sectional area A, second moment of inertia I, and added mass m for caranguiform type swimmer of Figure 4-6 (left). Amplitude H and phase ϕ from required kinematics (right). 72
4-12 Lumped parameter model. 73
4-13 Required head and tail phases. 74

5-1 Fish geometries: (a) Caranguiform swimmers side and top views, (b) Thunniform swimmers side and top views. The geometries are based on illustrations and photographs from biological samples [42, 43]. . . 78
5-2 Cable torque transmission. 79
5-3 Flexure 4-bar torque transmission. 80
5-4 Location of embedded transmission and RC servos used for actuation. 80
5-5 Basic caranguiform swimmer design: compliant body with embedded cable actuation transmission. Power and control signal are carried by umbilical cord (not shown). 82
5-6 Basic thunniform swimmer design: compliant body with embedded cable actuation transmission. Power and control signal are carried by umbilical cord (not shown). 83
5-7 Tuna inspired swimmer with individually controlled side fins. Power and control signal are carried by umbilical cord (not shown). 84

5-8 Shark inspired swimmer with individually controlled side fins. Power (batteries) and control hardware (microcontroller) are embedded inside the body. 85

5-9 Traditional radio control components: receiver (left), servo (center), and transmitter (right). A standard transmitter can be modified to drive RC servos dynamically, by connecting a function generator or timing circuit to the channel inputs instead of the traditional potentiometers. 87

5-10 *Plugapod*^{TM} microcontroller chip (left), *ZigBee*^{TM} wireless components (center), and board assembly (right) used to control prototypes. 87

5-11 Casting procedure: (a) Actuation mechanisms and other required hardware are positioned inside a two part wax mold. (b) Mold is closed and elastomer compounds used to cast the compliant fish-like body can be poured through mold openings. 89

5-12 Tuna fabrication example: Actuation mechanism with cable transmission and individually controlled side fins is assembled using rapid prototyped parts (left). Hardware components are positioned inside mold (center). Finished prototype is taken out of mold after elastomer compounds are cured (right). 89

5-13 Tuna inspired prototype views of side fins, embedded cable transmission, and caudal fin. Body surface grooves are due to mold finish. . . 90

5-14 Shark fabrication example. 90

5-15 Prototypes: (a) Big bass, (b) Tuna, (c) Shark 3, (d) Hybrid tuna, (e) Yellow bass, (f) Orange bass, (g) Green bass, (h) Clear bass, (i) White bass, (j) Hybrid bass 1, (k) Hybrid bass 2. 91

6-1 Dynamical mechanical analyzer experimental results. 95

6-2 Linear fit of experimental data for EcoFlex 0010 sample without pigmentation. 96

6-3 Acrylic tank and supporting hardware. 99

6-4 Tank with camera setup. 99
6-5 Tank with linear slide and low friction carriage setup. 99
6-6 Linear slide and carriage assembly features. 100
6-7 Low-friction carriage details. 101
6-8 Free swimming Hybrid bass movie frame (left image). Superposition of MATLAB processed frames: prototype contours appear in black, body markers for head, mid body, and caudal end appear in blue, green, and red respectively (right image). 101
6-9 Hybrid bass kinematics: Time history of amplitude variations for head (blue), mid body (green), and caudal end (red). 102
6-10 Lateral body oscillation amplitudes at caudal end. 102
6-11 Body wave number. 103
6-12 Thrust measurement hardware: (a) Low-friction carriage. (b) Fixture for small prototypes. 107
6-13 Static thrust fixture: Side view showing flexure connection to prototype and tension compression load cell (left image), top view showing anchoring structure and fixture submerged inside tank (right image). 107
6-14 Servo efficiency test setup. 108
6-15 Raw experimental measurements of voltage (blue traces), current (red traces), and static thrust (green traces) for a prototype swimming at frequencies between $1Hz$ and $5Hz$. 109
6-16 Average voltage, current and static thrust values versus swimming frequency. 110
6-17 Static thrust measurements and thrust estimates versus swimming frequencies. 111
6-18 Thrust measurements for caranguiform and thunniform prototypes. . 112
6-19 Swimming velocity measurements, swimming velocity estimates, and target swimming performance versus swimming frequencies. 113
6-20 Swimming velocity measurements for caranguiform and thunniform prototypes. 114

6-21 Total propulsive efficiency measurements and propulsive efficiency estimates versus swimming frequencies. 115
6-22 Subsystem 1: servomotor efficiency versus swimming frequencies. . . . 116
6-23 Subsystems 2 and 3: Combined body and hydrodynamics efficiency versus swimming frequencies. 117
6-24 Subsystem 3: Hydrodynamic efficiency versus swimming frequencies. . 117
6-25 Subsystem 2: Body efficiency versus swimming frequencies. 118
6-26 Swimming performance sensitivity to changes in modulus E. 119
6-27 Swimming performance sensitivity to changes in viscosity μ. 119

B-1 Fish-like compliant body model parameters. 134

List of Tables

4.1 Design problem Variables. 58

4.2 Scalings of kinematic parameters for both thunniform and caranguiform swimmers. 64

4.3 Scalings for geometry parameters derived from fish morphology in [42, 43]. 68

4.4 Variations of A, I, m, H, ϕ, and M from examples in Figures 4-9 and 4-11 and corresponding variations of E and μ ($i' \equiv \frac{\partial i}{\partial x}$). 73

5.1 Prototype material, geometric, and actuation parameter values. . . . 91

6.1 Measured material Properties. 97

Chapter 1

Introduction

This thesis presents new contributions to the area of design and mechanism synthesis of biomimetic devices for locomotion in liquid environments. This chapter motivates the need for autonomous locomotion in liquid environments and reviews the main challenges of the field. The work in the area of biomimetics is motivated by an interest on alternative, more efficient, locomotion techniques for exploration of liquid environments. Simplicity and improved mechanical robustness motivate the use of compliant mechanisms. The scope and objectives are presented and an outline of the thesis is provided.

1.1 Need and Challenges of Autonomous Locomotion in Liquid Environments

Exploration of liquid environments is of interest in several humanitarian, industrial and defence applications. Search and rescue, inspection of environmental accidents such as oil spills, de-mining, ocean sensing and mapping [1] are a few examples where a mission is enabled by the use of a device capable of moving within liquid environments. Furthermore, several mission environments are either physically inaccessible or too dangerous for human operators. Therefore, often, mission tasks must be accomplished by remotely operated or autonomous mechanical devices.

Several factors contribute to the success of autonomous exploration in liquid environments, yet hardware performance is perhaps the most influential. Autonomous devices should be able to move and survive in the required liquid environments in addition to perform the task characteristic to the mission. Hardware requirements include high locomotion efficiencies, high maneuverability, adaptability, mechanical robustness, stealth and autonomy. An efficient use of supply energy for locomotion allows longer mission ranges and smaller power supplies. This is critical for large scale persistent ocean sensing with applications ranging from weather statistics to natural disaster forecasting and prevention which requires devices able to convey appropriate sensors and survive for long time periods and navigate long ranges in ocean environments. Maneuvering capabilities, enabled by the number of degrees of freedom, are needed for navigation in complex geometries. Several environments involve crowded surroundings or require highly convoluted trajectories. Such is the case in de-mining and search and rescue operations where distances between objects of interest can be of the same order of magnitude as the device's body lengths, and where the scanning of particular areas can require closely tight and convoluted trajectories. In addition, environment properties such as density, viscosity or the surrounding geometry can change over the course of a mission. In such situations, mechanism adaptability is required in order to maintain a target locomotion performance. This is particulary true during reconnaissance of an oil spill where devices move through ocean water and oil while performing sensitive measurements. Furthermore, several liquid environments, including oceans, are extremely harsh and often require mechanisms to withstand high pressures, high temperatures, corrosive chemicals, and debris [2]. Therefore, appropriate mechanical robustness would prolong the life of a device. Moreover, stealth and blending well with the surroundings are important in tactical missions that require avoiding detection. Finally, navigation in real environments requires appropriate control techniques to achieve tasks autonomously.

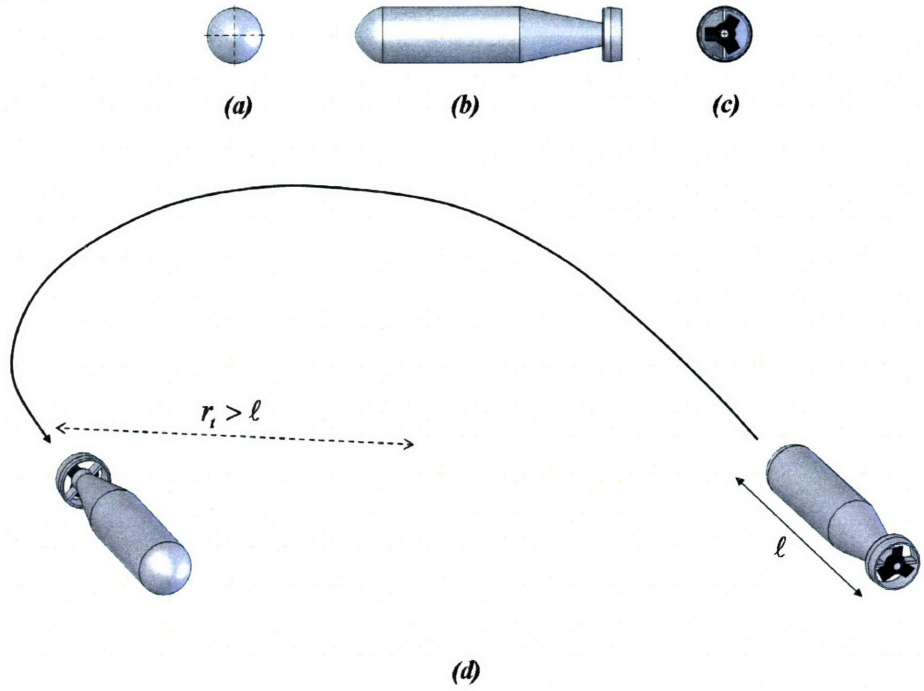

Figure 1-1: Typical long range AUV example (inspired by [3, 4]): (a) Front view, (b) Side view, (c) Back view, (d) Characteristic turning radius.

1.2 Why Biomimetic Locomotion Using Compliant Mechanisms?

The traditional approach for locomotion in liquid environments is to use propeller driven vehicles. Boats, submarines and other autonomous or remotely operated underwater vehicles use screw propellers to generate the thrust required for locomotion [3, 4, 5]. However, the ranges and complexities of liquid environment applications require devices that can combine both good maneuverability and high cruising speeds. Propeller driven vehicles are not capable of combining both [10].

Figures 1-1 and 1-2 illustrate typical limitations of propeller driven vehicles. As shown in Figure 1-1, turning radii of long range underwater vehicles are usually several body lengths. A typical more maneuverable underwater vehicle is shown in Figure 1-2. However, improving maneuverability by increasing the number and orientation of propeller axes also increases the vehicle volume and renders difficult to achieve a

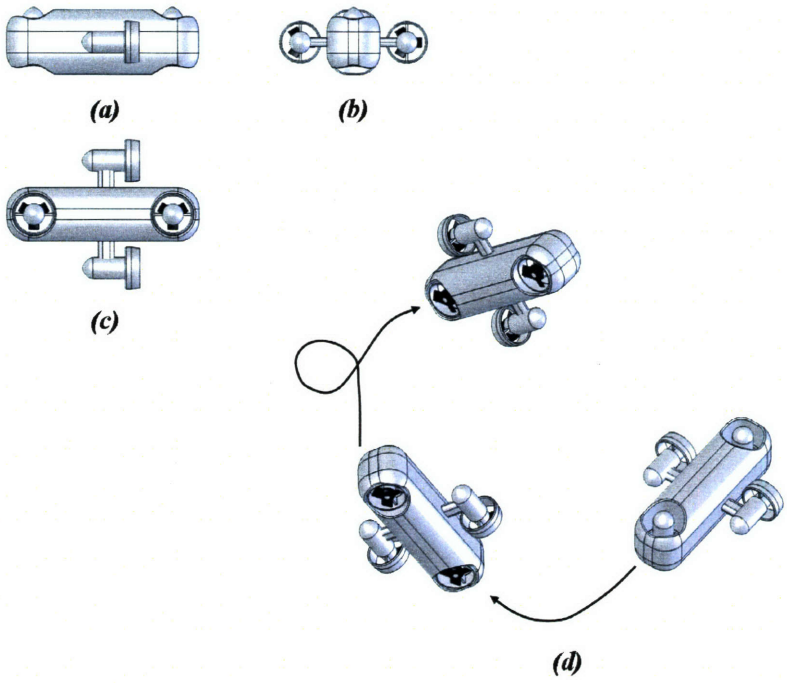

Figure 1-2: Highly maneuverable AUV example (inspired by [5]): (a) Side view, (b) Front view, (c) Top view, (d) Maneuvering capabilities.

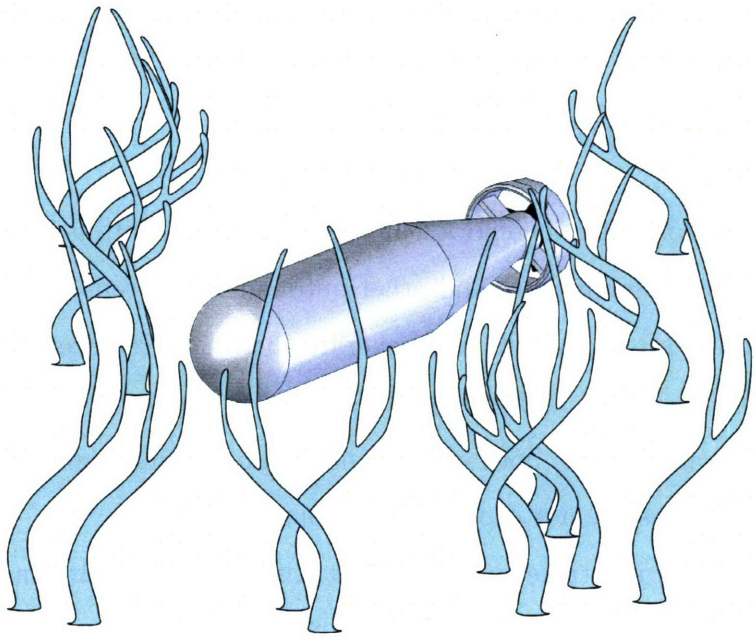

Figure 1-3: Vegetation and debris challenges in natural liquid environments: Propeller driven vehicles risk tangling when moving through environments with debris and vegetation.

streamlined projected area which ultimately affects cruising speeds through increased drag coefficients. In addition, scientific applications often require the observation of natural habitats or ocean life. The unnatural flow patterns and unsteadiness brought by propellers constitute a problem since these can disturb the environments through which they navigate. Finally, littoral environments, lakes, rivers and other natural shallow water environments are populated by a wide variety of vegetation where propelled vehicles risk tangling as shown in Figure 1-3.

Work on biomimetic approaches to locomotion in liquid environments, in particular fish-like propulsion, evolved in response to the need for mechanical mobile platforms that could achieve both maneuverability and good cruising speeds. In addition, fish-like propulsion techniques also hold the potential for improving propulsion performance [12]. Among the various biological locomotion techniques in liquid environments, fish appear to combine the most attributes in a single embodiment. Devices implementing such natural locomotion techniques could achieve cruising speeds in the order of $5\ell/s$ (body lengths per second), turning radii of less than a body length while not disturbing unnaturally the environments through which they navigate. However, the potential impact of biomimetic approaches is limited by the standard discrete and stiff mechanisms used to implement them [10, 33, 34, 35]. Most motions displayed by nature's creatures are kinematically complex. Therefore, there is an inherent disadvantage when trying to mimic these motions with discrete mechanisms since large numbers of degrees of freedom are required, making the resultant structures very complex. The resultant complexity can diminish internal mechanical efficiencies mostly through frictional losses. In addition, the large number of parts hinders mechanical robustness and the flexibility required in biomimetic vehicles increases the challenges of sealing and protecting sensitive parts [34]. Furthermore, the number of degrees of freedom also increases the sophistication of control techniques needed [33, 35].

Finally, different applications require different vehicle scales and performance. Nevertheless, a methodology to design and scale biomimetic devices for target performance goals does not exist. These features limit practical implementations of biomimetic approaches and constitute a barrier for a viable commercialization of this approach.

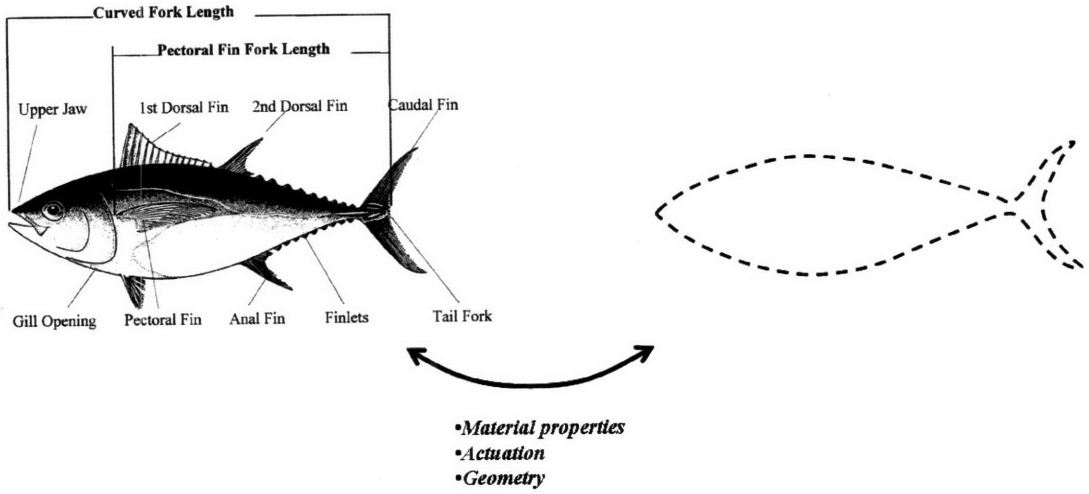

Figure 1-4: Biomimetic devices design problem.

A more robust embodiment and a rigorous and unified design approach are needed. To this end, a new mechanical paradigm is required, in particular, this thesis proposes the use of continuous compliant devices. Compliant mechanisms have an infinite number of degrees of freedom and a single self-contained structure can achieve complex motions that would require a very complex discrete chain to implement. Therefore, compliance reduces the number of discrete components needed. In addition, a continuous self-contained body does not require seals and extra components needed to protect complex assemblies from the environment. If a single compliant body could be designed to achieve the required complex kinematics, the resultant device would be simpler and as a result more mechanically robust.

1.3 Objectives, Scope and Overview of the Thesis

Figure 1-4 displays the side view of a fish, in this case a tuna, and a yet unknown device whose objective is to mimic the fish's performance. Tunas, like any other fish, are capable of achieving a given swimming performance due to their geometry and particular motions. An understanding of the dynamics that govern both the target fish motions and the proposed mechanical approach is essential in order to design

a device capable of approaching its biological target performance. Therefore, the objectives of the thesis are:

- Develop the required theoretical background required to establish guidelines for the design of compliant devices that implement biomimetic fish-like propulsion.
- Propose designs that translate the analytical results into practical devices.

The theoretical analysis and experimental work will concentrate on fish swimming techniques that display superior performance at the high Reynolds numbers since most current practical applications fall in this regime. This thesis does not attempt to synthesize geometries nor motions for "optimal swimming". Optimization studies in this area, using both finite differences and genetic algorithms, have achieved solutions that approach fish geometries and motions [10, 11]. Although such studies do not represent an absolute proof that fish geometries and swimming techniques constitute the optimal approach in regards to locomotion through high Reynolds numbers liquid environments, they do suggest that the geometries and kinematics used by fish must provide some advantage. Their reoccurrence in simulations and even across different species [15] further reinforces this idea. Therefore, the scope of the thesis is to develop devices that are simpler and mechanically better suited to implement fish swimming techniques than the current state of the art.

The thesis has been organized into 7 chapters. The motivation, objectives, and scope presented in the previous sections constitute the first chapter. Chapter 2 presents a review of the previous work in the fields of fish locomotion, bio-fluid-mechanics and biomimetics. Chapter 3 outlines the analysis of compliant devices that implement fish-like swimming motions. Chapter 4 presents scalings for the target performance and explains the proposed design methodologies. Chapter 5 describes the design features and fabrication techniques employed for the prototypes developed in this thesis. Chapter 6 details the performance characterization techniques and experimental results achieved by compliant biomimetic prototypes. Chapter 7 summarizes the thesis contributions and proposes future work enabled by the work presented in this thesis.

Chapter 2

Background

This chapter reviews the work related to the performance, physical understanding, and mechanical implementation of fish-like propulsion in liquid environments. A summary of the current knowledge regarding fish swimming performance is presented. Relevant mathematical models of fish swimming performance are then reviewed. The main types of mechanical approaches taken so far in biomimetics are described and their performance discussed. Finally, the main problems that remain unsolved are listed.

2.1 Fish Swimming Performance

A brief historical overview of the study of fish propulsion can be found in Videler's "Fish Swimming" [6]. The understanding of fish locomotion started with studies of body motions during swimming. In this thesis these characteristic body motions will be also referred to as *swimming kinematics*. Houssay [7] used time series photographs to show how a lateral wave of body curvature travels from head to tail during fish swimming. Breder [8] classified fish swimming techniques in two groups. A first group, where motions of body and or caudal fin (BCF) where at the basis of propulsion, contained the subgroups of anguilliform, subcarangiform, carangiform, thunniform, and ostraciiform swimmers. A second group where movements of appendages, median and or paired fins (MPF), provided the forces for locomotion contained as

many as seven subgroups such as rajifrom, diodontiform, amiiform, gymnotiform, balistiform, tetraodonttiform, and labriform. Present kinematics studies have shown the ill-definition of some of these classifications in terms of precise kinematic analysis [6]. However, these categories are still widely used as guidelines for fish classification. Gray [9] discovered four important general features in steady fish swimming:

- The speed of the body wave that travels down the length of the fish body is faster than the fish forward swimming speed.
- The amplitude of lateral motions varies for different parts of the body with a maximum reached near the tail tip.
- Due to inextensibility, each point on the body follows an undulating "figure of eight" path through the water as the fish moves forward.
- For anguilliform swimmers, the wavelength of the body wave is smaller than the fish body length.

Body waves are generated by muscles, called myotomes, distributed along the fish body. A detailed study of the characteristics of fish muscle can be found in [6].

Environments where fish can move freely and imaging techniques that monitor the flow and the fish body are required to study fish locomotion. In addition to large tanks, the means to experimentally measure fish performance include fish wheels and stationary flume tanks. Fish wheels are circular tanks that can be rotated at controlled angular velocities. Flume tanks, or flow loops, are tanks in which the flow can be circulated at controlled flow rates. For swimming studies, fish are trained, using food or other stimuli, to swim steadily along a given path. The advantage of large tanks with static water is that fish can move freely without the interference of flow or limited space. Imaging is accomplished with flow markers, such as dye, in conjunction with high speed cameras. More advanced techniques include digital particle imaging velocimetry (DPIV). Experimental results for several species are summarized by Videler [6]. Figure 2-1 displays the data for fish swimming velocities compiled in

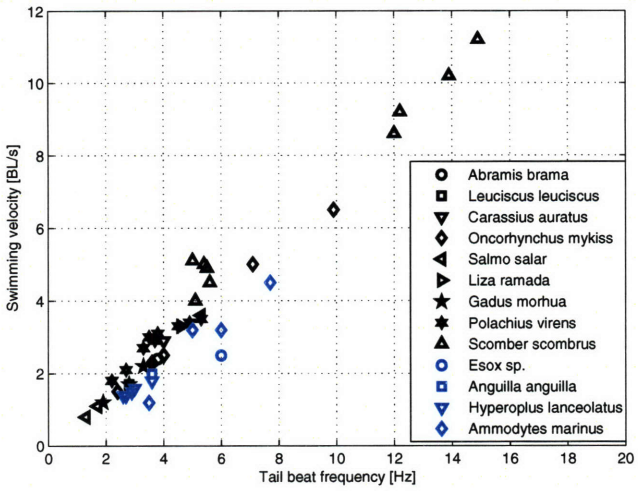

Figure 2-1: Fish swimming velocity scaled to body length (data from [6]).

[6]. An important feature to notice is that by expressing swimming velocities in body lengths per second a linear relation with tail beat frequency can be observed.

Variations of swimming kinematics related to speed or other parameters have also been explored. Jayne [16] studied the speed effects on the body kinematics of caranguiform type fish. His analysis of high speed video showed significant effects of both swimming speed and longitudinal location on variables describing amplitude, phase and wave length. Alternatively, Donley [14] studied the swimming kinematics of thunniform fish with similar techniques but found no noticeable changes in amplitudes and wavelengths due to speed. Furthermore, recent studies suggest that fish change their swimming kinematics when they encounter particular flow patterns. Liao and Beal studied the kinematics of trout, a caranguiform fish, swimming through the vortices shed by a cylinder placed ahead in an oncoming flow. They observed that the euthanized body of a trout placed on the wake of a particular cylinder can achieve forward motion [17]. They concluded that the trout's body passively tunes its motions to the oncoming flow vortices and can eventually achieve forward motion, which suggests that the body mechanical properties could actually facilitate locomotion.

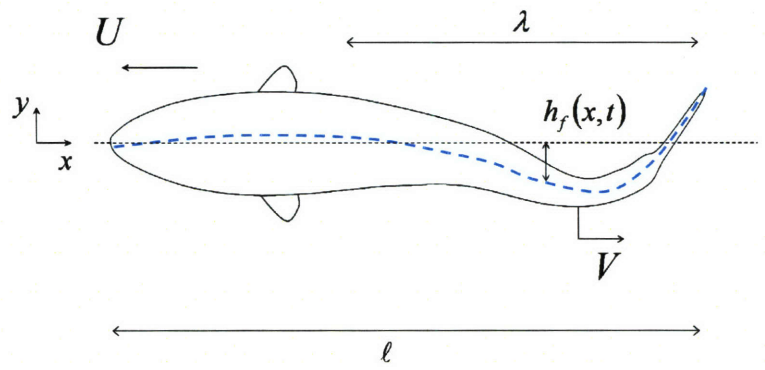

Figure 2-2: Reference frame and variables used to describe fish swimming kinematics.

2.2 Modeling Fish Swimming Performance

The theoretical study of fish swimming performance can be divided in two areas: The study of fish swimming motions or fish swimming kinematics, and the study of the forces involved in fish swimming dynamics.

2.2.1 Fish Swimming Kinematics

Since caranguiform and thunniform fish move by using their bodies and or fin motions to achieve the forces required for propulsion, the study of these motions is essential to the understanding of swimming performance. Figure 2-2 displays relevant parameters for the study of swimming kinematics and the corresponding coordinate system used to describe these motions. The dorsal (top) view of a fish of length ℓ swimming at an average velocity U is shown. The reference frame (xy) is fixed to the fish's nose $(x = 0)$ and moves at the same speed. Lateral deflections $h_f(x,t)$ of the body centerline result in a backward propagating (positive x-direction) body wave of velocity V and body wavelength λ. For steady straight swimming, fish tend to minimize their projected area by folding in against their bodies their pectoral, pelvic and anal fins. In addition, the motions of the body centerline are confined to the (xy) plane with some exceptions in species that can control the curvature of their caudal or dorsal fins. In general the body waves increase in amplitude from head to tail. As explained in the previous section, a standard experimental approach to identify the nature of the body motions

is to use high-speed film sequences showing top views of fish steadily swimming along a straight path. Body outlines and particular points along the body length are digitized, and linear regressions are used to identify appropriate models capable of describing their displacements. Videler [6] proposed a model that could describe the lateral body motions h_f using six fourier coefficients a_j and b_j,

$$h_f \approx \sum_{j=1,3,5} [a_j(x)cos(2j\pi t/\tau) + b_j(x)sin(2j\pi t/\tau)] \tag{2.1}$$

where τ is the period of the motions and only the first three odd Fourier terms are used because the body motions are laterally symmetric. In addition, the contributions of the third and fifth Fourier frequencies in both magnitude and phase are small in comparison to the contributions of the first Fourier frequency [6]. Alternatively, Barrett [10] proposed a simpler model for the fish body lateral motions h_f consisting of a sinusoidal traveling wave with an amplitude envelope,

$$h_f \approx (c_1 x + c_2 x^2)sin(\omega t - kx) \tag{2.2}$$

where ω is the tail beat frequency, and $k = \omega/V = 2\pi/\lambda$ is the body wave number. The constants c_1 and c_2 define the amplitude envelope of the fish motions. Barrett's simplification represents mainly the first fourier frequency in Videler's regression model, and assumes the amplitude of head oscillations are negligible (amplitude envelope is zero at $x = 0$). Lighthill [18] and Wu [23] also suggested models consisting of a sinusoidal traveling wave with an amplitude envelope on their theoretical studies of fish swimming. As a result, most modern theoretical studies of fish swimming utilize analogous models of body deformations as the basis for the dynamic studies of swimming performance.

2.2.2 Fish Swimming Dynamics

The study of fish swimming dynamics benefited from developments in the mathematical theory of locomotion at high Reynolds numbers. Sir James Lighthill's seminal

paper "Note on the swimming of a slender fish" [18] proposed a theory that considered the flow of the fluid outside the thin boundary layer on a fish's body. This consideration allows the inertial effects to be dominant and justifies the use of an inviscid fluid model. The theory, in which the force due to the water interaction is of a reactive nature, was supported by Wu's work on "Swimming of a waving plate" [23] published shortly after Lighthill's work. Lighthill's theory considers elongated bodies that are laterally symmetric, with small body surface slopes, and zero cross-sectional areas at both ends. In addition, the lateral perturbations due the motions of the body should be small in comparison to the forward motion, mainly,

$$\left|\frac{\partial h}{\partial x}\right| \ll 1, \quad \left|\frac{\partial h}{\partial t}\right| \ll U$$

The theory is also applicable to slender fish-like swimmers with a sharp downstream edge, and the constraints of the body slope can be relaxed at the nose of the fish and close to the caudal fin provided the changes occur over a small fraction of a body length. However, slender-body theory fails to be applicable for propulsion with high aspect ratio caudal fins. In thunniform fish, for example, the slope of the upstream or leading edge can not be considered small and the elongated body theory brakes down.

This section summarizes the main results of the theory. For detailed mathematical derivations the reader should refer to Appendix A. The theory defines the y-component of the velocity of a cross section, $w(x,t)$, seen by the moving water slice, as the approximate material derivative of the body lateral displacement $h(x,t)$,

$$w(x,t) = \frac{\partial h}{\partial t} + U\frac{\partial h}{\partial x} \equiv Dh \tag{2.3}$$

In addition, the apparent mass $m(x)$ of a cross-section at x is approximated by the expression,

$$m(x) \simeq \frac{1}{4}\beta\pi s(x)^2\rho_f \tag{2.4}$$

where β is a geometry dependent constant whose value is close to unity, $s(x)$ is the

body depth at x, and ρ_f is the density of the liquid medium. The units of m are of mass per unit length. The lateral force L_y exerted by the body on the water slice is modeled by the material derivative of $m(x)w(x,t)$.

$$L_y = D(m(x)w(x,t)) = \left(\frac{\partial}{\partial t} + U\frac{\partial}{\partial x}\right)\left[m(x)\left(\frac{\partial h}{\partial t} + U\frac{\partial h}{\partial x}\right)\right] \tag{2.5}$$

In a frame of reference moving with the body, the rate of work $P(t)$ of the lateral motions is given by,

$$P(t) = \int_0^\ell L_y \frac{\partial h}{\partial t} dx = \int_0^\ell D(mw)\frac{\partial h}{\partial t} dx \tag{2.6}$$

which can be rearranged as,

$$P(t) = \frac{\partial}{\partial t}\int_0^\ell \left(\frac{1}{2}mw^2 - Umw\frac{\partial h}{\partial x}\right) dx + U\left[mw\frac{\partial h}{\partial t}\right]_{x=\ell} \tag{2.7}$$

In the frame of reference where the water far from the fish is at rest, the rate of working $P(t)$ is instead given by,

$$P(t) = UT + U\left[\frac{1}{2}mw^2\right]_{x=\ell} + \frac{\partial}{\partial t}\int_0^\ell \left(\frac{1}{2}mw^2\right) \tag{2.8}$$

where the first term is the work done by the fish in moving at velocity U in the direction of the thrust T. The second term represents the rate at which kinetic energy of water movements per unit length of fish is shed into the wake at the trailing edge (wasted energy). The third term represents the rate of change of the total kinetic energy ahead of the trailing edge. From Equations (2.7) and (2.8), an expression for the thrust T is found,

$$T = \left[mw\left(\frac{\partial h}{\partial t} - \frac{1}{2}w\right)\right]_{x=\ell} - \frac{\partial}{\partial t}\int_0^\ell \left(mw\frac{\partial h}{\partial x}\right) dx \tag{2.9}$$

and the average thrust is simply,

$$\langle T \rangle = \left\langle \left[mw \left(\frac{\partial h}{\partial t} - \frac{1}{2} w \right) \right]_{x=\ell} \right\rangle \tag{2.10}$$

where $\langle i \rangle$ stands for average value of i. Therefore, the theory predicts that the mean thrust depends only on kinematic and geometry conditions at the edge of the caudal fin ($x = \ell$)[18]. The propulsion efficiency is defined as the ratio of useful propulsion power UT and the total power spent P,

$$\eta = \frac{U\langle T \rangle}{\langle P \rangle}$$

From Equation (2.7),

$$\langle P \rangle = \left\langle U \left[mw \frac{\partial h}{\partial t} \right]_{x=\ell} \right\rangle \tag{2.11}$$

therefore,

$$\eta = \frac{U \left\langle \left[mw \left(\frac{\partial h}{\partial t} - \frac{1}{2} w \right) \right]_{x=\ell} \right\rangle}{\left\langle U \left[mw \frac{\partial h}{\partial t} \right]_{x=\ell} \right\rangle} = \frac{\left\langle \left[\frac{\partial h}{\partial t} w - \frac{1}{2} w^2 \right]_{x=\ell} \right\rangle}{\left\langle \left[w \frac{\partial h}{\partial t} \right]_{x=\ell} \right\rangle}. \tag{2.12}$$

Subsequent work [19, 20, 21, 22] extended the applicability of this theory to large amplitude lateral motions. In addition the effects of vortex shedding from the body and fins can also be included as explained in [28].

Lighthill's elongated body theory relates propulsion performance in terms of thrust and swimming efficiency to kinematic and geometric variables at the fish's posterior end. This simplification proves very useful to gain intuition on the relevant physics that govern fish-like locomotion. Several alternative theories have been developed to increase the accuracy of predictions regarding fish locomotion performance. The three-dimensional waving plate theory developed by Cheng [29] is an example. In this theory, the incompressible potential flow past a flexible thin plate of finite aspect ratio performing a small-amplitude undulatory motion is treated by a linear unsteady vortex ring panel method in the frequency domain. The plate and its wake are replaced

by a suitable distribution of vortex rings in a way to satisfy the appropriate boundary conditions and solve for the resulting body and fluid dynamic forces. However, Lighthill's elongated body theory remains the simplest, most intuitive, and elegant alternative. More complex models often sacrifice physical intuition for small gains in accuracy.

2.3 Biomimetic Mechanisms

Experimental work on fish swimming performance played a key role in motivating engineers to explore mechanical alternatives for locomotion in liquid environments. In particular, Gray's paradox, which originated from experimental measurements by Gray that seemed to indicate that the thrusts required by dolphins to swim at observed speeds far exceeded estimations of available mammal muscle power. This observation was in general interpreted as and indication that fish motions achieved particular hydrodynamic effects that tended to minimize drag forces. This paradox stimulated several experimental studies aimed at finding a solution. In this context, the first experimental biomimetic mechanical devices were built. Two types of devices were developed, devices designed to mimic both fish morphology and kinematics, and devices inspired by the underlaying physics of fish locomotion. The following section summarizes the work in both approaches.

2.3.1 Fish-like Devices

Fish-like devices mimic the geometry and motions of a real fish. A good example is the mechanical tuna or"Robotuna" built by Barrett [10] which possessed enough degrees of freedom to emulate the lateral body motions of a real tuna. Barrett used available experimental data on real fish to single out a number of variables relevant for propulsion and used a genetic algorithm to search the variable space for configurations that would minimize drag and optimize other performance metrics. However, the Robotuna was not a free-swimming device, the mechanism was towed inside a towing tank while drag and energy consumption were recorded. Barrett's conclusions

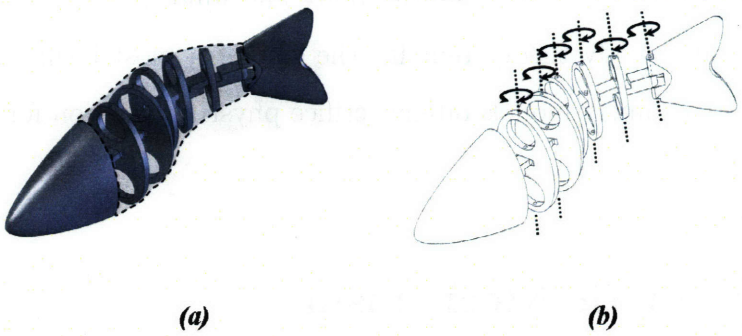

Figure 2-3: Traditional biomimetic fish design. Body mechanism is composed of a hyper-redundant manipulator. The body links are driven either in a direct drive configuration or through pulleys and cables connected to actuators (not shown) located at a particular section in the body (inspired by [34, 35]): (a) Skin covering internal mechanism. (b) Hyper-redundant manipulator spine.

where that implementing fish like motions could in fact achieve drag reduction.

Following on Barrett's steps several groups proposed free swimming mechanical devices. Some examples include: Anderson's vorticity control unmanned undersea vehicle (VCUUV) which was also modeled on a tuna (thunniform swimmer) [33], Kumph's robotic pike (anguilliform swimmer) [34], and Yu's caranguiform robots [35]. Despite years of development, the performance of these devices has not been able to match real fish performance. Anderson's robotic tuna achieved a maximum velocity of $1.2m/s$ $(0.6\ell/s)$(*Body lengths per second*) [33], Kumph's robotic pike achieved a maximum velocity of $0.09m/s$ $(0.1\ell/s)$ [34], and Yu's carangiform swimmer achieved a maximum velocity of $0.32m/s$ $(0.8\ell/s)$ [35]. In contrast, experimental data such as the one presented in Figure 2-1 shows that real fish can swim at speeds as high as $11\ell/s$ depending on the species [6]. The standard design paradigm used in current fish-like devices is shown in Figure 2-3 where a hyper-redundant manipulator can be seen acting as the body spine. Body links are driven either in a direct drive configuration or using pulleys and cables connected to actuation located at a particular section inside the body.

2.3.2 Foil Propelled Devices

An alternative biomimetic approach is to implement into a device only relevant physical and dynamic characteristics from nature without actually fully mimicking the biological source. Such is the case of foil propelled vehicles in which the fish-like swimming performance is pursued by implementing mechanisms that move foils in a way to recreate physical phenomena present during fish swimming. Anderson [32] studied the performance of heaving and pitching foils. The parameters controlled included angle of attack, Strouhal number (non-dimensional frequency) and heave to cord ratio. Features associated with optimal propulsive performance included moderately large angles of attack, formation of two vortices per cycle in the wake and the existence of small and moderated leading edge vortices. Read [36] identified high propulsive efficiencies in his study of oscillating foils. In addition, Bandyopadhyay [37], and Czarnowski [38] explored the feasibility of propelling rigid hull vehicles with foils, and Licht et al. [39] built and tested a foil propelled vehicle. So far, however, this type of mechanical implementations have also been unsuccessful in achieving similar performance to its biological counterparts.

2.4 Limitations of Current Approaches

The impact and potential for practical and commercial implementations of biomimetic approaches are limited by the standard discrete and stiff mechanisms currently used. Most motions displayed by nature's creatures are kinematically complex. Therefore, there is an inherent disadvantage when trying to imitate these motions with discrete mechanisms since large numbers of degrees of freedom are required, making the resultant structures very complex. The resultant complexity can diminish internal mechanical efficiencies mostly through frictional losses. Locomotion efficiency data suggests values as high as 80% for fish-like swimming mechanisms [12, 13]. However, these numbers exclude mechanical transmission and actuator losses. Most fish considered fast swimmers achieve steady speeds with body oscillations ranging from $3Hz$ to $5Hz$ [6] while Barrett [10] measured transmission losses already in the order of 10%

at a driving frequency of $1Hz$ for his mechanical tuna based on a hyper-redundant manipulator design. In addition, the large number of parts hinders mechanical robustness since the flexibility required in biomimetic vehicles increases the challenges of sealing and protecting sensitive parts [34]. Finally, the number of degrees of freedom increases the sophistication of control techniques needed [33, 35]. The data presented in the previous section clearly suggests that these limitations influence the performance displayed by current biomimetic mechanisms. In addition, it is not clear how the present hardware would perform and what design changes would be needed when implemented at different scales.

Simpler, more robust mechanisms are the key to the incorporation of biomimetic devices in applications where propeller driven mechanisms are currently the standard. Therefore, there is a need for a new design approach that guaranties these features and provides design guidelines to scale design features.

2.5 Summary

This chapter reviewed the main work in fish swimming studies, modeling, and the state of the art in mechanical implementations of fish-like swimming techniques. Over the years, fish swimming studies have revealed how the body motions (referred to as swimming kinematics in this thesis) can be represented by a traveling sinusoidal wave combined with an amplitude envelope. In addition, the elegant approach of elongated body theory allows the computation of average propulsive thrust and locomotion efficiency through simple relations involving geometric and kinematic variables evaluated at the tail tip. Finally, the current mechanical implementations display important limitations regarding mechanical robustness and efficiency due to their complexity.

Chapter 3

Compliant Biomimetic Devices

The previous chapter summarized the relevant experimental and theoretical work concerning fish swimming and biomimetic devices. Two major limitations where identified in current biomimetic approaches: complexity and lack of a structured design process. This chapter introduces an alternative mechanical implementation of fish-like mechanisms for locomotion in liquid environments that eliminates the limitations of current biomimetic devices. The proposed approach is based on the use of natural dynamics as means to reduce required actuation and mechanism complexities. The objectives of this chapter are to present the mathematical models needed to evaluate the feasibility of the new approach and to portray its advantages.

3.1 Exploiting Natural Vibrations

When a mechanical structure is exited by an input force or displacement the input energy is stored by inertia and elastic body components and dissipated through resistive body components resulting in structural motions [40]. In order to achieve particular motions, a device can then use a proper distribution of passive energy storage and dissipation along its body in combination with a single input as an alternative to actively controlling a discrete number of body locations. Figure 3-1 displays two images that illustrate this idea. A continuous fish-like body made of a visco-elastic material is shown at rest in Figure 3-1(a), and after it has been exited with a harmonic

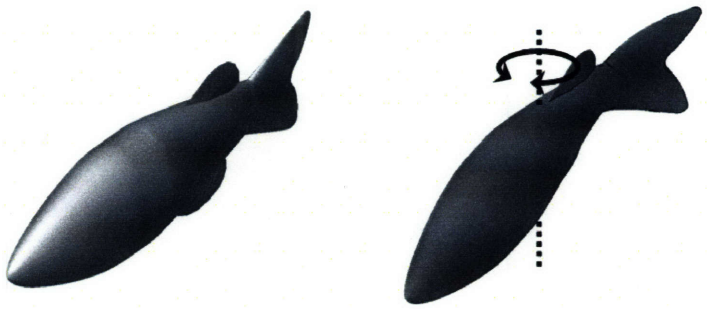

(a) *(b)*

Figure 3-1: Using body natural modes of vibration: (a) Compliant visco-elastic fish-like body at rest. (b) Compliant visco-elastic fish-like body exited by a concentrated moment.

input in Figure 3-1(b). As a result of compliance and resistance the body displays complex motions even though only one input is applied. Therefore, required complex motions can be achieved by a single self contained body which would eliminate the need for complex mechanisms and seals. As a result, the survival capabilities of a device in harsh environments, or its mechanical robustness, depends predominantly on the endurance of the materials used through the body. A proper choice of material properties can then both reduce complexities and achieve improved mechanical robustness. The proposed approach and its advantages rest on two hypotheses whose validity can be proven through mathematical analysis and experimentation.

Hypothesis 1. *The natural dynamics of a compliant visco-elastic fish-like body actuated by a single input can be designed to mimic biomimetic swimming motions through the proper distribution of energy storage and dissipation.*

Hypothesis 2. *A continuous self-contained fish-like body with proper material composition has superior mechanical robustness in harsh liquid environments than a device composed of several discrete components.*

The following sections present the theoretical background required to analyze the first hypothesis. Models that describe the motions of fish-like slender bodies

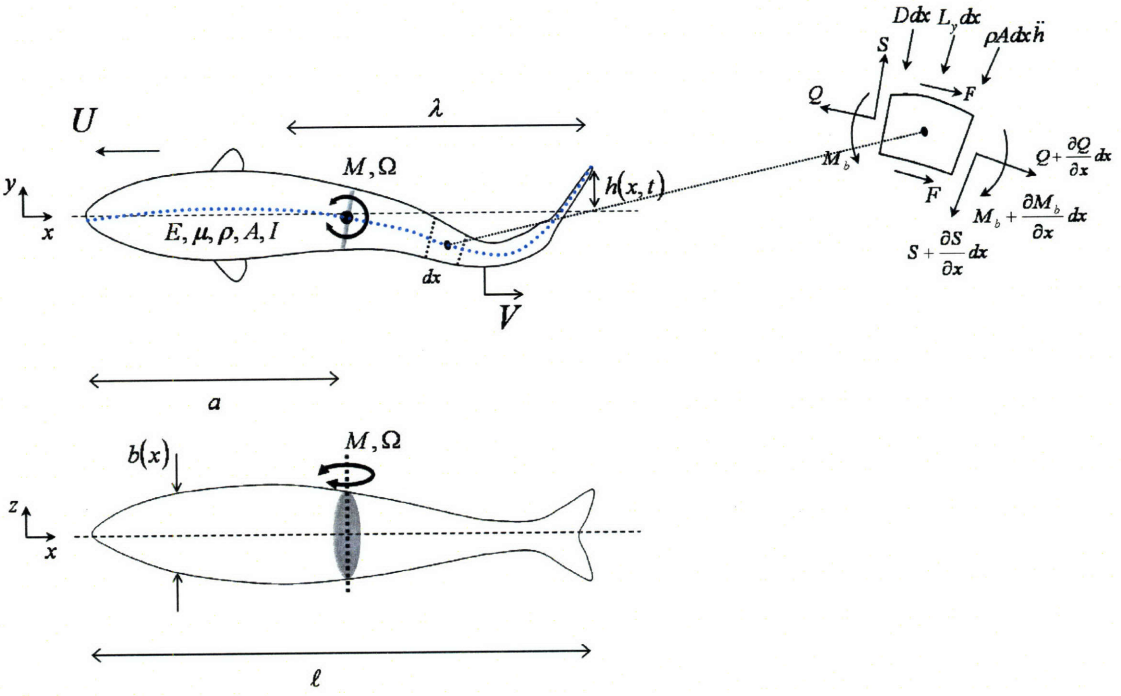

Figure 3-2: Top and side views of fish-like compliant body of length ℓ. Geometry and material properties are defined by depth $b(x)$, cross-sectional area $A(x)$, second moment of inertia $I(x)$, modulus of elasticity $E(x)$, viscosity $\mu(x)$, and density $\rho(x)$ which are all functions of x. A concentrated moment of magnitude M and frequency Ω is applied at a distance a from the nose. As a result body undulations of wavelength λ travel from nose to tail at a velocity V. Body undulations propel the body at an average velocity U.

submerged in a liquid environment are developed, and the limits of propulsion performance and its sensitivity to parameter variation are also analyzed. The actual approaches to prove the validity of the first hypothesis are outlined in Chapter 4. The second hypothesis will be analyzed in the context of the experimental results detailed in Chapter 6.

3.2 Lateral Vibrations of Slender Bodies

In this thesis the term "slender body" is used to describe symmetrical bodies whose longitudinal dimensions are larger than their width and thickness. Caranguiform and thunniform fish bodies can be characterized as slender.

3.2.1 Internal Dynamics

Figure 3-2 displays top and side views of a fish-like slender body of length ℓ that is exited by a concentrated harmonic moment of magnitude M and frequency Ω located at a distance $x = a$ from the anterior end. The forces per unit length acting on a body element dx include the longitudinal component of shear and pressure forces $F(x,t)$, the longitudinal tension $Q(x,t)$ induced by $F(x,t)$, the lateral force $L_y(x,t)$ exerted by the liquid medium, the transversal viscous force $D(x,t)$, a shear force $S(x,t)$, and a bending moment $M_b(x,t)$. It is assumed the body is composed of a material with anisotropic modulus of elasticity $E(x)$, anisotropic material viscosity $\mu(x)$, and anisotropic density $\rho(x)$. The body geometry is defined by a cross-sectional area $A(x)$, a second moment of area $I(x)$, and a depth $b(x)$. The resulting lateral motions $h(x,t)$ of the body centerline are assumed to lie in the xy plane. A body traveling wave of wavelength λ and velocity V in the positive x-direction propels the body at an average forward velocity U in the negative x-direction [18]. For small centerline deflections, $h(x,t) \leq 0.1\ell$, the plane cross-sections initially perpendicular to the body centerline remain plane and perpendicular to the neutral axis during bending [40, 41]. For a body element in Figure 3-2 the balance of forces in the x-direction yields,

$$\frac{\partial Q}{\partial x} + F = 0 \tag{3.1}$$

in the y-direction,

$$-\frac{\partial S}{\partial x}dx - L_y dx - D dx = \rho A dx \frac{\partial^2 h}{\partial t^2} - \frac{\partial}{\partial x}\left(Q\frac{\partial h}{\partial x}\right) \tag{3.2}$$

and neglecting the rotational inertia effects, the moment equilibrium yields,

$$-S dx + \frac{\partial M_b}{\partial x}dx \approx 0 \tag{3.3}$$

In addition, the effects of tension and lateral viscous forces can also be neglected [24, 31]. Therefore, combining Equations (3.2) and (3.3) yields,

$$\frac{\partial^2 M_b}{\partial x^2} = -L_y - \rho A \frac{\partial^2 h}{\partial t^2} \tag{3.4}$$

The total bending moment M_b is a combination of the actuation moment $M(x,t)$ and the moment due to the body resistance to bending. Energy storage and dissipation are present through the visco-elasticity of the materials used. Therefore, assuming a uniaxial stress configuration, the simplest constitutive relations for elastic and viscous stresses are respectively,

$$\sigma_e = E\epsilon = E\frac{y}{\zeta} \tag{3.5}$$

$$\sigma_v = \mu\frac{\partial \epsilon}{\partial t} = \mu y \frac{\partial}{\partial t}\left(\frac{1}{\zeta}\right) \tag{3.6}$$

where ζ is the local body radius of curvature and ϵ is the local strain. For small deflections, $\frac{1}{\zeta} \approx \frac{\partial^2 h}{\partial x^2}$. The corresponding bending moments are,

$$M_e = \int_A y\sigma_e dA = EI\frac{\partial^2 h}{\partial x^2} \quad and \quad M_v = \int_A y\sigma_v dA = \mu I \frac{\partial}{\partial t}\frac{\partial^2 h}{\partial x^2} \tag{3.7}$$

the total bending moment can be found by adding all the components,

$$M_b = -M + M_e + M_v$$

Therefore, the lateral motions $h(x,t)$ are governed by the following equation,

$$\frac{\partial^2}{\partial x^2}\left(-M + EI\frac{\partial^2 h}{\partial x^2} + \mu I \frac{\partial}{\partial t}\frac{\partial^2 h}{\partial x^2}\right) = -L_y - \rho A\frac{\partial^2 h}{\partial t^2} \tag{3.8}$$

where the first term in the left hand side is the input moment, the second term represents capacitive energy storage, and the third term represents energy dissipation through viscosity. The terms in the right hand side represent the fluid resistance and the body inertia respectively. Wu [24] proposed a similar modeling approach but failed to include energy dissipation through a viscous term. Cheng [31] proposed a

similar model with dissipation that accounted for the composite nature of fish bodies, in particular, the radial anisotropies resulting from the differences in bone, muscle, and skin material properties of fish. However, neither Wu's model nor Cheng's accounted for anisotropies along the length of the body as in the present case.

Alternatively, incorporating the rotational inertia terms and the deformations of the cross-sections that Equation (3.8) neglects, the governing dynamic equation becomes,

$$\begin{aligned}\frac{\partial^2 M}{\partial x^2} - \frac{\partial^2}{\partial x^2}\left(\frac{EIL_y}{AG\kappa_s}\right) - \frac{\partial^2}{\partial x^2}\left(\frac{EI\rho}{G\kappa_s}\frac{\partial^2 h}{\partial t^2}\right) - \frac{\partial^2}{\partial x^2}\left(EI\frac{\partial^2 h}{\partial x^2}\right) \\ - \frac{\partial^2}{\partial x^2}\left(\mu I\frac{\partial}{\partial t}\left(\frac{L_y}{AG\kappa_s}\right)\right) - \frac{\partial^2}{\partial x^2}\left(\mu I\frac{\partial}{\partial t}\left(\frac{\rho}{G\kappa_s}\frac{\partial^2 h}{\partial t^2}\right)\right) - \frac{\partial^2}{\partial x^2}\left(\mu I\frac{\partial^3 h}{\partial t \partial x^2}\right) \\ - L_y - \rho A\frac{\partial^2 h}{\partial t^2} = \rho I\frac{\partial^2}{\partial t^2}\left(\frac{L_y}{AG\kappa_s}\right) + \rho I\frac{\partial^2}{\partial t^2}\left(\frac{\rho}{G\kappa_s}\frac{\partial^2 h}{\partial t^2}\right) + \rho I\frac{\partial^4 h}{\partial t^2 \partial x^2} \quad (3.9)\end{aligned}$$

where G is the shear modulus and κ_s is a deformation factor that depends on cross-section geometries. A detailed derivation of Equation (3.9) can be found in Appendix B. Equations (3.8) and (3.9), without viscous terms, are usually referred to as Bernoulli-euler beam equation and Timoshenko beam equation respectively [40, 41]. However, including the energy dissipation in the system, through the viscous terms, is central to the realization of the appropriate fish-like motions as it will be shown in the next sections. Equation (3.9) is more general and as such is more appropriate to the analysis of large lateral body deformations. However, for steady forward swimming the assumption of small amplitude lateral body deformations allows the simplifications yielding Equation (3.8). Equation (3.9) can be analyzed to better understand the physical and geometrical implications that support this argument. The orders of

magnitude of terms in Equation (3.9) are,

$$O: \frac{M}{(\ell^\star)^2} - \frac{E^\star I^\star L_y}{A^\star G^\star \kappa_s (\ell^\star)^2} - \frac{E^\star I^\star \rho^\star H^\star (\omega^\star)^2}{G^\star \kappa_s (\ell^\star)^2} - \frac{E^\star I^\star H^\star}{(\ell^\star)^4}$$
$$- \frac{\mu^\star I^\star L_y \omega^\star}{A^\star G^\star \kappa_s (\ell^\star)^2} - \frac{\mu^\star I^\star H^\star (\omega^\star)^3 \rho^\star}{G^\star \kappa_s (\ell^\star)^2} - \frac{\mu^\star I^\star H^\star \omega^\star}{(\ell^\star)^4}$$
$$- L_y - \rho^\star A^\star H^\star (\omega^\star)^2 = \frac{\rho^\star I^\star L_y (\omega^\star)^2}{A^\star G^\star \kappa_s} + \frac{(\rho^\star)^2 I^\star H^\star (\omega^\star)^4}{G^\star \kappa_s} + \frac{\rho^\star I^\star H^\star (\omega^\star)^2}{(\ell^\star)^2}$$

where $E^\star, G^\star, \mu^\star, \rho^\star, A^\star, I^\star, \omega^\star, \ell^\star$, and $H^\star$ are characteristic material, geometry and kinematic variables. Each term in Equation (3.9) has units of force per unit length (N/m). The conditions that justify neglecting shear and inertia terms are,

$$\frac{E^\star I^\star H^\star}{(\ell^\star)^4} \gg \frac{E^\star I^\star L_y}{A^\star G^\star \kappa_s (\ell^\star)^2}, \quad \frac{E^\star I^\star H^\star}{(\ell^\star)^4} \gg \frac{E^\star I^\star \rho^\star H^\star (\omega^\star)^2}{G^\star \kappa_s (\ell^\star)^2} \tag{3.10}$$

$$\frac{\mu^\star I^\star H^\star \omega^\star}{(\ell^\star)^4} \gg \frac{\mu^\star I^\star L_y \omega^\star}{A^\star G^\star \kappa_s (\ell^\star)^2}, \quad \frac{\mu^\star I^\star H^\star \omega^\star}{(\ell^\star)^4} \gg \frac{\mu^\star I^\star H^\star (\omega^\star)^3 \rho^\star}{G^\star \kappa_s (\ell^\star)^2} \tag{3.11}$$

$$\rho^\star A^\star H^\star (\omega^\star)^2 \gg \frac{\rho^\star I^\star L_y (\omega^\star)^2}{A^\star G^\star \kappa_s}, \quad \rho^\star A^\star H^\star (\omega^\star)^2 \gg \frac{(\rho^\star)^2 I^\star H^\star (\omega^\star)^4}{G^\star \kappa_s},$$
$$\rho^\star A^\star H^\star (\omega^\star)^2 \gg \frac{\rho^\star I^\star H^\star (\omega^\star)^2}{(\ell^\star)^2} \tag{3.12}$$

Equations (3.10) imply that bending forces due to elasticity dominate over the shear forces due to elasticity. Equations (3.11) imply that bending forces due to viscosity are higher than shear forces due to viscosity. Finally, Equations (3.12) imply that forces due body mass lateral acceleration dominate over the inertia forces due to angular acceleration. For small lateral body deflections the above conditions hold true and the body dynamics area accurately represented by Equation (3.8). The remainder of the analysis will therefore use the simplified dynamics.

3.2.2 Coupling to External Fluid Mechanics

Equation (3.8) shows how the body dynamics are influenced by the system interaction with the liquid environment through the force L_y. If the cross-flow caused by

transverse motion of the body is approximately two-dimensional along planes perpendicular to the axis of the body, and the flow does not separate, Lighthill's elongated body theory [18] predicts that L_y can be modeled by the material derivative of the lateral momentum,

$$L_y = \left(\frac{\partial}{\partial t} + U\frac{\partial}{\partial x}\right)[m(x)w(x,t)] = m(x)\frac{\partial^2 h}{\partial t^2} + 2Um(x)\frac{\partial \partial h}{\partial t \partial x} + U\frac{\partial m(x)}{\partial x}\frac{\partial h}{\partial t} + U^2\frac{\partial m(x)}{\partial x}\frac{\partial h}{\partial x} + U^2 m(x)\frac{\partial^2 h}{\partial x^2} \quad (3.13)$$

where the values of the velocity $w(x,t)$ of lateral pushing of a vertical water slice by the element dx, and the added mass per unit length $m(x)$ are as defined in the previous chapter. If shedding of vorticity occurs at sections along the contracting part of the body, the expression of the force L_y can be further simplified by assuming a constant added mass m [27]. Therefore,

$$L_y = m\left(\frac{\partial}{\partial t} + U\frac{\partial}{\partial x}\right)^2 h = m\frac{\partial^2 h}{\partial t^2} + 2Um\frac{\partial \partial h}{\partial t \partial x} + U^2 m\frac{\partial^2 h}{\partial x^2}. \quad (3.14)$$

The terms in Equation (3.13) and (3.14) represent inertial forces due to the different component of lateral velocity of the body centerline. The orders of magnitude of the terms in L_y are,

$$O : m^\star H^\star (\omega^\star)^2 + U^\star m^\star \frac{H^\star \omega^\star}{\ell^\star} + (U^\star)^2 \frac{m^\star H^\star}{(\ell^\star)^2}$$

where $m^\star$ is a characteristic added mass, $H^\star$ is a characteristic lateral deflection amplitude, $\ell^\star$ is a characteristic body increment, $\omega^\star = \frac{1}{\tau}$ is the characteristic frequency of the system, and $U^\star$ is characteristic swimming velocity. Performance experiments on fish have shown the existence of a linear relation between swimming speed and tail beat frequency. For fast swimmers, such as caranguiform type swimmers this relation is of the form [6],

$$\frac{U}{\ell} \sim 0.1\omega$$

Therefore, $\frac{U}{\ell}$ is at least an order of magnitude smaller than ω. As a result, the magnitude contribution of the U terms to the total lateral force can be neglected in comparison to the contribution of the ω term. The orders of magnitude being,

$$O : m^{\star}H^{\star}(\omega^{\star})^2 + 0.1m^{\star}H^{\star}(\omega^{\star})^2 + 0.01m^{\star}H^{\star}(\omega^{\star})^2$$

where the first inertial term, $m^{\star}H^{\star}(\omega^{\star})^2$, corresponding to $m\frac{\partial^2 h}{\partial t^2}$ is the dominant term. Therefore,

$$L_y \sim m\frac{\partial^2 h}{\partial t^2}.$$

Equations (3.8) and (3.13) model the dynamic behavior of a slender body moving in a liquid environment in terms of material properties, geometry, actuation properties, and fluid interaction.

3.2.3 Analysis

Equation (3.8) is a partial differential equation with variable coefficients, therefore it can not be solved analytically using standard techniques. However, solving the constant coefficient equivalent can provide physical intuition into the system dynamics. Assuming E, μ, ρ, A, I and m have constant values through the length of the body and approximating the lateral force L_y as in the previous section, Equation (3.8) becomes,

$$EIh'''' + \mu I\dot{h}'''' + (m(x) + \rho A)\,\ddot{h} = \delta'(x-a)Msin(\Omega t) \tag{3.15}$$

where the short hand notation $h' = \frac{\partial h}{\partial x}$ and $\dot{h} = \frac{\partial h}{\partial t}$ has been used to simplify the notation. An approximate solution to Equation (3.15) in terms of series can be found using modal expansion techniques. However, in this case an exact solution can be found using Green functions. For a complete derivation the reader can refer to Appendix B. The procedure assumes a solution of the form $w = H(x)e^{i\Omega t}$, where $h(x,t) = Re\{w(x,t)\}$. For a prototype swimming freely in a liquid environment, the boundary conditions should prescribe zero shear and moment at both ends [22],

hence,

$$\begin{aligned}
\left[-M + EIh'' + \mu I\dot{h}''\right]_{x=0} &= 0 \qquad \left[-M' + EIh''' + \mu I\dot{h}'''\right]_{x=0} = 0 \\
\left[-M + EIh'' + \mu I\dot{h}''\right]_{x=\ell} &= 0 \qquad \left[-M' + EIh''' + \mu I\dot{h}'''\right]_{x=\ell} = 0
\end{aligned} \tag{3.16}$$

The solution found for this case is of the form,

$$\begin{aligned}
h(x,t) = Re\Bigg\{ \frac{Me^{i\Omega t}}{\kappa^3(EI + i\mu I\Omega)} \Big[& \kappa\phi_3(x-a)u(x-a) \\
& + \phi_4(x-a)\delta(x-a) - Q_3(a)\phi_1(x) - Q_4(a)\phi_2(x)\Big]\Bigg\}
\end{aligned} \tag{3.17}$$

where $u(x)$ is the unit step function and $\delta(x)$ is the dirac delta function and,

$$\kappa^4 = \frac{(m(x) + \rho A)\Omega^2}{(EI + i\mu I\Omega)}$$

$$\phi_3(x) = \frac{1}{2}(cosh(\kappa x) - cos(\kappa x))$$

$$\phi_4(x) = \frac{1}{2}(sinh(\kappa x) - sin(\kappa x))$$

$$Q_3 = -\frac{\kappa(-\phi_4(\ell - a)\phi_4(\ell) + \phi_1(\ell - a)\phi_3(\ell))}{\phi_2(\ell)\phi_4(\ell) - \phi_3(\ell)^2}$$

$$Q_4 = -\frac{\kappa(-\phi_1(\ell - a)\phi_2(\ell) + \phi_4(\ell - a)\phi_3(\ell))}{\phi_2(\ell)\phi_4(\ell) - \phi_3(\ell)^2}$$

Equation (3.17) describes the lateral body deflections $h(x,t)$ of a uniform cross-section swimmer in terms of material, geometrical and actuation properties. In order to estimate the dominant dynamics, an order of magnitude approximation can again be used. Assuming a solution of the form $h \sim He^{i(\omega t + \phi)}$, the orders of magnitude of the terms in Equation (3.15) are,

$$\left(\frac{EI}{(\ell - a)^4} - (\rho A + m)\omega^2\right)He^{i(\omega t+\phi)} + i\left(\frac{\mu I\omega}{(\ell - a)^4}\right)He^{i(\omega t+\phi)} = \frac{M}{(\ell - a)^2}e^{i(\omega t)}$$

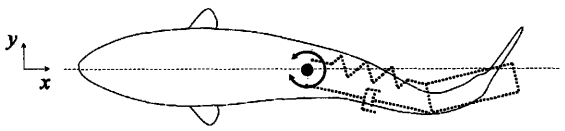

Figure 3-3: Lumped parameter model of posterior body section.

Therefore, the amplitude H and phase ϕ can be shown to have the following orders of magnitude,

$$H \sim \frac{\frac{M}{(\ell-a)^2}}{\sqrt{\left(\frac{EI}{(\ell-a)^4} - (\rho A + m)\omega^2\right)^2 + \left(\frac{\mu I \omega}{(\ell-a)^4}\right)^2}} \tag{3.18}$$

$$\phi \sim tan^{-1}\left(\frac{\frac{\mu I \omega}{(\ell-a)^4}}{\frac{EI}{(\ell-a)^4} - (\rho A + m)\omega^2}\right) \tag{3.19}$$

and $k(x) = \phi/x$. This approximation for estimating the amplitude and phase of lateral motions is equivalent to modeling the posterior body section with a spring-mass-damper lumped parameter model. Figure 3-3 portrays this idea by superimposing the equivalent lumped parameter model on the fish-like elongated body. The validity of these approximations can be later confirmed through experiments. However, this order of magnitude simplification reveals two very important properties. First, since the actuation moment M appears only in Equation (3.18) it can only influence the magnitude of body oscillations. In addition, Equation (3.19) shows the direct dependence of the body phase ϕ on the body viscosity μ. The required body traveling waves are achieved through phase differences between subsequent points in the body. Therefore, when using a single actuation input, the proper timing of the body wave cannot be achieved without the energy dissipation associated with the body viscosity μ since for a material with zero viscosity the phase through the body would always be zero resulting in standing waves.

Proposition 1. *To achieve body traveling waves, a key feature of fish-like kinematics, a compliant body must display visco-elastic material properties.*

3.3 Swimming Performance

This section uses Elongated body theory (see Appendix A for derivations) to predict a prototype's swimming performance in terms of thrust, swimming speed and total swimming efficiency. The fish swimming kinematics model used is of the form,

$$h(x,t) = H(x)sin(wt - \kappa x) \tag{3.20}$$

where $\kappa = w/V$. Elongated body theory predicts an average thrust of the form,

$$\langle T \rangle = \frac{m(\ell)}{4}\left(H(\ell)^2\left(w^2 - \kappa^2 U^2\right) - U^2 H'(\ell)^2\right) \tag{3.21}$$

the average swimming velocity is obtained from the balance between thrust and drag at steady state,

$$T = Drag = \frac{1}{2}\rho_f C_d A U^2$$

where C_d is the drag coefficient for a particular prototype. Therefore,

$$U = \sqrt{\frac{\frac{m(\ell)}{4}w^2 H(\ell)^2}{\left(\frac{1}{2}\rho_f C_d A + \frac{m(\ell)}{4}\left(\kappa^2 H(\ell)^2 + H'(\ell)^2\right)\right)}} \tag{3.22}$$

To estimate the average swimming velocity U, a model for the drag coefficient C_d is also needed. The standard empirical models are not appropriate since the body undergoes motions that result in changes in the projected area and the fluid dynamics surrounding the body. Therefore, an expression for the drag should be derived from basic principles. Since thrust and drag are dynamically related, and estimate of drag coefficient can be derived from Equation (3.21). Elongated body theory neglects the contributions from motions of the body's anterior end since the area at $x = 0$ is negligible. In addition, for caranguiform and thunniform fish swimmers $H(0) \ll H(l)$. However, for biomimetic swimming devices this might not be the case as errors in mimicking swimming motions could yield considerable amplitudes at the anterior end and should be taken into account. Therefore, the drag coefficient model used is of

the form,

$$C_d \sim \left(H'(\ell) - H'(0)\right).$$

To study the total propulsion efficiency η it is useful to decompose the system in three subsystems. Figure 3-4 displays a side view of an elongated body swimmer and indicates the locations of 3 subsystems. Subsystem 1 consists of the actuator which converts electrical energy input from a battery or power supply to mechanical energy applied to the body as a concentrated moment. Therefore,

$$\eta_1 = \frac{M\dot{h}'_a}{vi} \tag{3.23}$$

where v and i are the voltage and current supplied to the actuator by the power supply and $\dot{h}'_a$ is the angular velocity of the body at the point $x = a$ where the actuation M is applied. Subsystem 2 consists of the elongated body which converts the mechanical energy supplied by the actuator to the mechanical energy applied to the liquid environment. Hence,

$$\eta_2 = \frac{\int_0^\ell (\dot{h}L_y)dx}{M\dot{h}'_a} = \frac{\frac{1}{2}Um\omega^2 H(\ell)^2\left(1-\frac{U}{V}\right)}{\frac{1}{2}Msin(ka)\dot{h}'_a} \tag{3.24}$$

Subsystem 3 consists of the body interactions with the liquid environment. The elongated body applies a mechanical energy to the liquid that surrounds it, and as a result a thrust T is generated that allows the elongated body to move forward at a speed U [30] thus,

$$\eta_3 = \frac{UT}{\int_0^\ell (\dot{h}L_y)dx} = \frac{1}{2}\left(1+\frac{U}{V}\right) - \frac{1}{2}\left(\frac{U}{\omega}\right)^2\left(1-\frac{U}{V}\right)^{-1}\left(\frac{H'(\ell)}{H(\ell)}\right)^2 \tag{3.25}$$

The total propulsion efficiency is given by,

$$\eta = \eta_1 \times \eta_2 \times \eta_3 \tag{3.26}$$

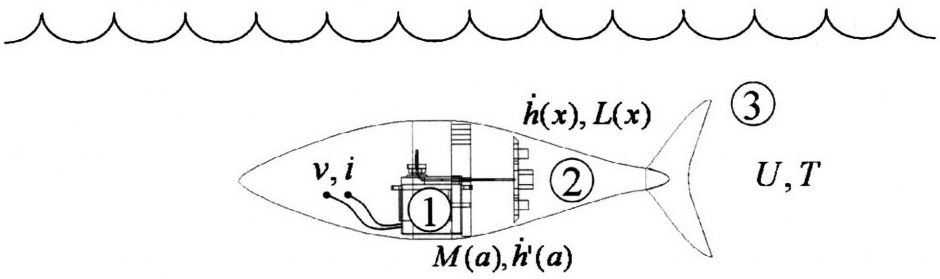

Figure 3-4: Elongated-body swimmer subsystems.

The propulsion performance described by Equations (3.21),(3.22) and (3.26) is related to the body kinematics through the variables $H(\ell)$ and κ (or V since they are equivalent). The most important feature of elongated body theory is the simplicity and physical intuition achieved in the expressions defining propulsion performance. Using the order of magnitude approximations in Equations (3.18) and (3.19) would allow similar simplicity and physical intuition for the expressions defining body kinematics.

3.4 Performance Limits and Sensitivity to Parameter Changes

The ability to predict the maximum performance that can be delivered by a system as well as how changes in design parameters would affect the resulting performance is invaluable. Design parameters for compliant biomimetic devices include material properties (E, μ, ρ), geometrical properties $(A(x), I(x), \ell)$, and actuation properties (M, Ω, a). In this study, swimming performance is defined by three parameters: propulsive thrust T, swimming velocity U, and propulsion efficiency η. Equations (3.21)through (3.25) illustrate the propulsion performance parameter dependence, which can be summarized as follows,

$$T \propto \left(H(\ell), \kappa, m(\ell)\right)$$

$$U \propto \left(H(\ell), \kappa, m(\ell), C_d\right)$$

$$\eta \propto \left(H(\ell), \kappa, m(\ell), C_d, v, i\right)$$

The added mass value $m(\ell)$ is constrained when mimicking a particular target and as discussed in the previous section the drag coefficient C_d is proportional to swimming kinematics variables. As a result swimming kinematics, defined by body lateral amplitude H and wave number κ (proportional to phase ϕ), control the resulting swimming performance. To find how the design parameters ultimately influence swimming performance the swimming kinematics parameter dependance needs to be explored. To this purpose, the order of magnitude approximations in Equations (3.18) and (3.19) are useful as they define, with simple relations, how the design parameters control swimming kinematics, mainly,

$$H(x) \propto (E, \mu, \rho, A, I, \ell, M, \Omega, a)$$

$$\phi \propto (E, \mu, \rho, A, I, \ell, \Omega, a)$$

The performance limits of compliant fish-like elongated body swimmers can then be found by plugging in Equations (3.18) and (3.19) into Equations (3.21)through (3.25) and looking for maximum values. The design methodologies presented in Chapter 4 outline a set of bounds on these values. In principle the maximum performance should occur for a set of design parameters that guaranties perfect tracking of target fish swimming kinematics.

The sensitivity of swimming performance to changes in design parameters can be explored by analyzing changes in performance to perturbations in design parameter values. For example, let U_M be the maximum swimming velocity achieved for a set of design parameters $(DP_1, ..., DP_n)$. The sensitivity of U to a change in a given design parameter DP_i can be defined as,

$$Z_U(DP_i) = U_M - U(DP_i + \Delta)$$

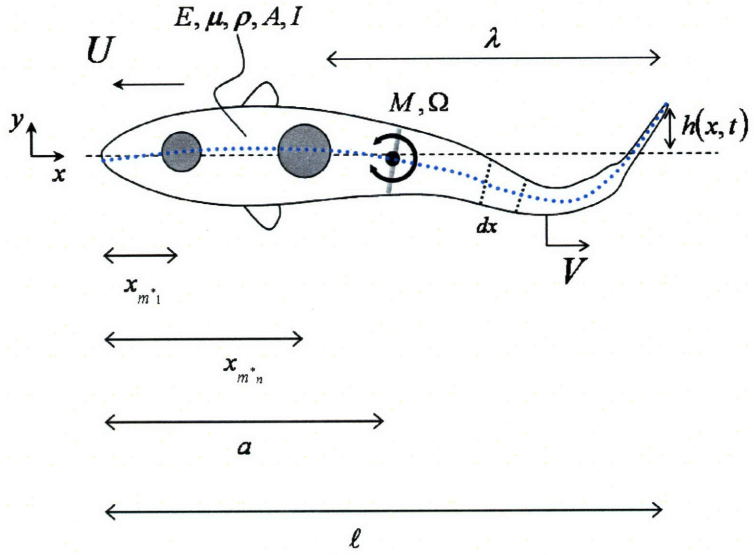

Figure 3-5: Addition of concentrated masses in the body model.

where $U(DP_i + \Delta)$ is the new value of U when all design parameters remain the same except for DP_i whose value is changed to $DP_i + \Delta$. Experimental validation of these concepts will be carried through in Chapter 6.

3.5 Model Refinements

Additional hardware such as actuators and sensors will affect the lateral dynamics of compliant fish-like elongated bodies. As an example, Figure 3-5 shows a modified model of the lateral body motions that includes two discrete masses $m_1^\star$ and $m_n^\star$ (e.g. one actuator and one sensor) embedded inside the body at distances $x_{m_1^\star}$ and $x_{m_n^\star}$ from the anterior end. The contribution of concentrated masses can be easily included in the existing dynamic model. Equation (3.8) becomes,

$$\frac{\partial^2}{\partial x^2}\left(-M + EI\frac{\partial^2 h}{\partial x^2} + \mu I\frac{\partial}{\partial t}\frac{\partial^2 h}{\partial x^2}\right) = -L_y - \rho A\frac{\partial^2 h}{\partial t^2} - \sum_{i=1}^{n}\delta(x - x_{m_i^*})m_i^*\frac{\partial^2 h}{\partial t^2} \quad (3.27)$$

where the contribution of n concentrated masses is reflected by the summation term. Concentrated masses are assumed to lie in the body center axis.

3.6 Summary

This chapter presented the models used to predict the swimming kinematics and resulting swimming performance of compliant elongated body swimmers. The swimming motions can be found by solving the dynamic equation that governs the body dynamic behavior. Alternatively, the parameters of interest, amplitude H and phase ϕ, can be estimated using and order of magnitude analysis. Propulsion performance is estimated using elongated body theory. The propulsive thrust T, swimming velocity U, and resulting propulsion efficiency η are dependent on swimming kinematics at the tail tip ($x = \ell$). Performance limits and performance sensitivity to changes in design parameters can be analyzed using the developed models. Finally, the body lateral vibrations model can also account for extra dynamic effects brought by actuators and sensors.

Chapter 4

Design Methodologies

This chapter describes three approaches for the design of compliant biomimetic swimming devices. The target performance is scaled using data from biological studies. Conditions on the kinematic and actuation inputs which are necessary and sufficient for realistic physical solutions are derived. The designs that meet these conditions constitute a new class of biomimetic mechanisms.

4.1 Objectives and Problem Definition

The parameters involved in the design problem are listed in Table 4.1 along with a brief description and corresponding units. The goal of the design methodologies is to identify the prototype's design parameters $(E, \mu, \rho, A, I, m, \ell, M, \Omega, a)$ that would result in a particular target propulsion performance. The propulsion performance is defined by three parameters: propulsive thrust T, swimming velocity U, and total propulsion efficiency η. For the biomimetic devices presented in this thesis,

$$\eta = \frac{UT}{vi}$$

where v and i are the voltage and current consumed during swimming. The analysis developed in the previous chapter reveals how performance parameters T, U, and η depend on the swimming kinematics defined by the amplitude envelope H, and the wave

Variable	Description	Units
E	Modulus of elasticity	$[N/m^2]$
μ	Viscosity	$[Ns/m^2]$
ρ	Density	$[kg/m^3]$
A	Cross-sectional area	$[m^2]$
I	Second moment of inertia	$[m^4]$
m	Added mass per unit length	$[kg/m]$
ℓ	Body length	$[m]$
M	Actuation moment	$[Nm]$
Ω	Actuation angular frequency	$[rad/s]$
a	Concentrated moment location	$[m]$
H	Amplitude of lateral motion	$[m]$
κ	Body wave number	$[rad/m]$
T	Propulsive thrust	$[N]$
U	Average swimming velocity	$[m/s]$
η	Total propulsion efficiency	$[-]$

Table 4.1: Design problem Variables.

number κ (proportional to phase ϕ) and how in turn these parameters are related to material, geometrical, and actuation design parameters $(E, \mu, \rho, A, I, m, \ell, M, \Omega, a)$. Therefore, instead of expressing the target performance in terms of T, U, and η the corresponding kinematic variables can be used as the target variables for the methodology. In this sense, the kinematic variables can be though of as intermediate variables or a change of variables that would simplify calculations. The design methodologies can then simply solve for the material properties (E,μ,ρ), the geometrical properties (A, I, m, ℓ), and the actuation properties (M, Ω, a) that would yield required kinematics values H and κ responsible for a given performance set T, U, and η. However, fish-like morphology is required to achieve fish-like swimming performance while implementing fish-like motions. In addition, a neutrally buoyant body is more convenient for depth control purposes. A negatively buoyant body would required constant motions to generate lift and avoid sinking and a positively buoyant body would required more thrust effort for diving. Hence, the composite density of a prototype should match the density of the liquid environment. For the prototypes proposed in this thesis, the bulk of the density is defined by the density of the materials used in the body. Finally, assuming the system is linear, the input

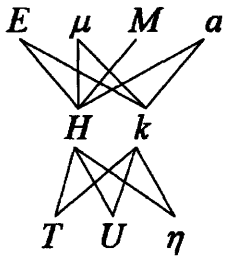

Figure 4-1: Relations between unknown design parameters E, μ, M, a, swimming kinematics variables H, κ, and corresponding swimming performance parameters U, T, η.

actuation frequency must correspond to the target swimming frequency. Therefore, the resulting constraints are,

$$A(x) = A_{fish}(x), \quad I(x) = I_{fish}(x), \quad m(x) = m_{fish}(x),$$
$$\ell = \ell_{fish}, \quad \rho = \rho_{fluid}, \quad \Omega = \omega \quad (4.1)$$

As a result, the design methodologies must solve only for four design parameters, namely: E, μ, M, a. Figure 4-1 displays the dependence among the unknown design parameters and the target performance based on Equations (3.18),(3.19),(3.21),(3.22), and (3.26). Note that the values of E,μ, and a influence the propulsion performance through both H and κ while the moment M only affects the performance through H. For designs where the material and actuation location are not dynamically controllable this implies that the phase is fixed and only the amplitude can be used for swimming performance control. The consequences of this feature will be discussed in the next chapter.

4.2 Target Performance

The target performance is that of caranguiform and thunniform fish. From the three parameters chosen to define propulsion performance, experimental data for swimming velocity U is more widely available since it is relatively easier to measure on real fish than both thrust T and total propulsion efficiency η. For real fish $\eta = \frac{UT}{\frac{\partial \varepsilon}{\partial t}}$, where ε

is the amount of energy consumed by a fish and eventually used for propulsion. The relation between fish swimming velocity and tail beat frequency $f = \frac{\omega}{2\pi}$ is given by [6],

$$\frac{U}{\ell} \sim s_0 f \tag{4.2}$$

where s_0 is a constant that varies depending on the type of swimming technique. The previous art, both theoretical [18, 30, 12] and experimental [6, 10], suggests that to achieve such swimming performance fish implement body kinematics of the form,

$$h_{req} = H(x)sin(\omega t - \kappa x)$$

where $H(x)$ is an amplitude envelope, ω is the tail beat frequency and κ is the wave number. Both the target amplitude envelope H and the target wave number κ can vary for different swimming techniques, different swimming speeds, and fish body lengths [6, 14, 15, 16]. Therefore, in order to establish a generalized target kinematics model it would be useful to identify the scaling laws relating H and κ to identifiable variables. The following subsections identify such scalings for both thunniform and caranguiform swimmers.

4.2.1 Thunniform Swimmers

For thunniform swimmers, body wave number κ is proportional to body length ℓ,

$$\kappa = \frac{2\pi}{\lambda} = \frac{2\pi}{s_1 \ell}$$

where λ is the body wave length and $s_1 \sim 1.1$ [6]. Figure 4-2 displays the characteristic amplitude envelope of the body motions for a thunniform swimmer scaled to its body length $\left(\frac{H}{\ell}\right)$. The tail beat frequency, representative of swimming velocity, does not appear to have an effect over the amplitude envelope since this last remains unchanged for a wide range of swimming speeds [14, 15]. The shape of the amplitude envelope

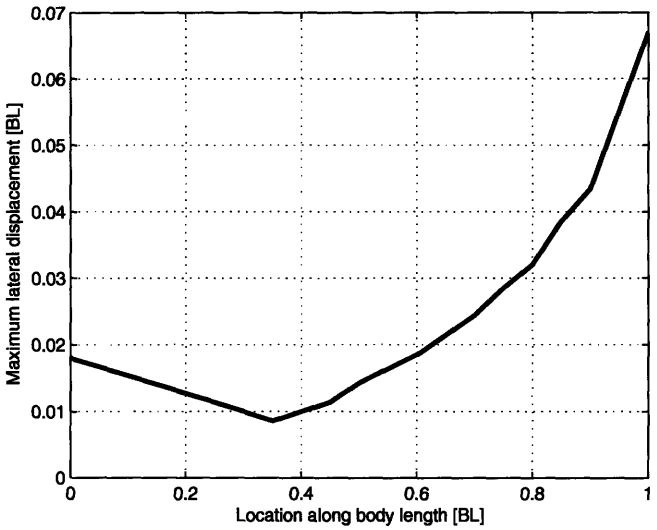

Figure 4-2: Scaled amplitude envelope $\left(\frac{H}{\ell}\right)$ for thunniform swimming kinematics (based on experimental results from [14, 15]).

in Figure 4-2 can be accurately modeled by a second order polynomial,

$$H(x) = a_1 + a_2 x + a_3 x^2$$

In addition, the amplitudes at both the head ($x = 0$) and tail ($x = \ell$) ends are constant,

$$H(0) = a_1 + a_2 0 + a_3 0^2 = a1 = s_2 \ell$$

$$H(l) = a_1 + a_2 \ell + a_3 \ell^2 = s_3 \ell$$

where $s_2 \sim 0.02$ and $s_3 \sim 0.1$ [14]. Moreover, the minimum amplitude occurs at a location $x = s_4 \ell$, where $s_4 \sim 0.3$, hence,

$$\left(\frac{\partial H}{\partial x}\right)_{s_4 \ell} = a_2 + 2 a_3 s_4 \ell = 0$$

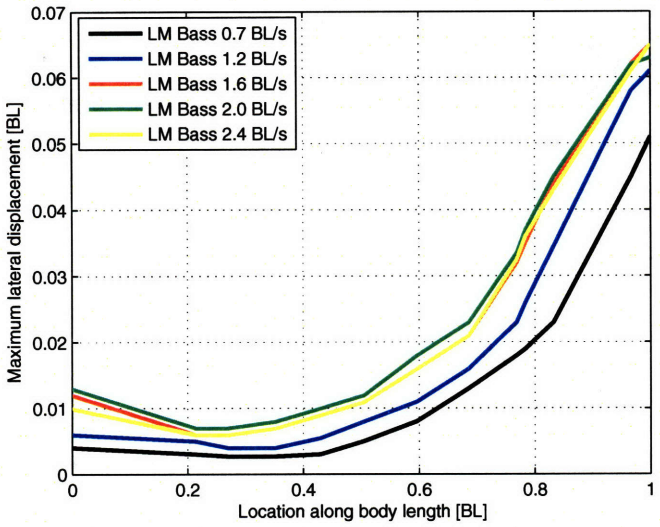

Figure 4-3: Scaled amplitude envelopes $\left(\frac{H}{\ell}\right)$ for caranguiform swimming kinematics at different swimming velocities (based on experimental results from [16]).

Therefore, the parameters defining the amplitude envelope can be found by solving the system conformed by the above equations. For thunniform swimmers,

$$a_1 = s_2\ell, \quad a_2 = \frac{-2s_4(s_3 - s_2)}{(1 - 2s_4)}, \quad a_3 = \frac{s_3 - s_2}{(1 - 2s_4)\ell}$$

4.2.2 Caranguiform Swimmers

For caranguiform swimmers, the steady swimming speed is related to tail beat frequency [6],

$$\frac{U}{\ell} \sim s_5 f$$

where $s_5 \sim 0.78$, and the body wave number κ is,

$$\kappa = \frac{2\pi}{\lambda} = \frac{2\pi}{s_6\ell}$$

where $s_6 \sim 0.9$ [6, 16]. Figure 4-3 displays characteristic amplitude envelopes, scaled to the body length $\left(\frac{H}{\ell}\right)$, of the body motions in a caranguiform swimmer swimming at different speeds. For caranguiform fish, swimming velocity, and therefore tail beat

frequency, appears to have an effect over the swimming amplitude envelope [16]. The amplitude envelopes can again be modeled by second order polynomial, and from Figure 4-3 the maximum amplitudes at both ends of the body can be identified and related to swimming velocity. Therefore,

$$\frac{H(0)}{\ell} = \frac{a_1 + a_2 0 + a_3 0^2}{\ell} = \frac{a1}{\ell} = s_7 \frac{U}{\ell} = s_7 s_5 f$$

$$\frac{H(\ell)}{\ell} = \frac{a_1 + a_2 \ell + a_3 \ell^2}{\ell} = s_8 \frac{U}{\ell} = s_8 s_5 f$$

where $s_7 \sim 0.005$ and $s_8 \sim 0.024$. In addition, the minimum amplitudes occurs at a location $x = s_4 \ell$, where $s_4 \sim 0.3$, hence,

$$\left(\frac{\partial H}{\partial x}\right)_{s_4 \ell} = a_2 + 2 a_3 s_4 \ell = 0$$

Once more, the parameters defining the amplitude envelope can be found by solving the system conformed by the above equations. Therefore, for caranguiform swimmers,

$$a_1 = s_7 s_5 f \ell, \quad a_2 = \frac{-2 s_4 s_5 f (s_8 - s_7)}{(1 - 2 s_4)}, \quad a_3 = \frac{s_5 f (s_8 - s_7)}{(1 - 2 s_4) \ell}$$

4.2.3 Target Performance Summary

The scalings of kinematic parameters for thunniform and caranguiform swimmers are summarized in table 4.2. The parameters κ, a_1, a_2 and a_3 can be used to represent the kinematics of thunniform and caranguiform swimmers at different scales and swimming velocities. These scaled parameters provide a more general target kinematics model that can be used in the design methodologies. The next step is to develop guidelines for finding the appropriate design parameters that ensure a prototype achieves the performance summarized in Table 4.2. The following section presents three approaches that can be used to this end.

Parameter	Thunniform Swimmer	Carangiform Swimmer
κ	$\sim \frac{5.7}{\ell}$	$\sim \frac{7}{\ell}$
a_1	$\sim 0.02\ell$	$\sim 0.004f\ell$
a_2	~ -0.12	$\sim -0.02f$
a_3	$\sim \frac{0.2}{\ell}$	$\sim \frac{0.04f}{\ell}$

Table 4.2: Scalings of kinematic parameters for both thunniform and caranguiform swimmers.

4.3 Design Methodologies

The target performance used in the design methodologies is defined by swimming kinematics parameters. The analysis in this section outlines three approaches that can be taken to identify the required design parameters.

4.3.1 Approach 1: Bulk Approximation

The problem of finding appropriate design parameters for a given target swimming kinematics can be seen as a data fitting problem. The data in this case is the target swimming kinematics $h_{fish}(x,t)$ (lateral motions of real fish, $h_{fish} = h_{req}$) and a parametric model for the lateral motions $h(x,t)$ of a prototype can be used to fit this data. As discussed in the previous chapter $h(x,t)$ is a function of design parameters and can be found by solving Equation 3.8. Therefore, by minimizing the fitting errors, the appropriate design parameters that would enable an $h(x,t)$ similar to $h_{fish}(x,t)$ can be identified. However, a closed form solution for $h(x,t)$ can only be found easily for the special case where the coefficients in Equation 3.8 are constant. The approximate solution given by Equation (3.17) can then be used as a parametric model for a swimmer with constant cross-section and bulk material properties. The constraints in (4.1) can be added and the fit can be done in a least squares sense. Figure 4-4 illustrates this idea by using a block diagram. The diagram shows how an estimate of the body lateral deflection $h(x,t)$ can be compared to the required body lateral deflection $h_{fish}(x,t)$ in order to find the actuation, material, and geometric properties that minimize the error $h_e = h_{fish} - h$. Figure 4-5 displays the resulting

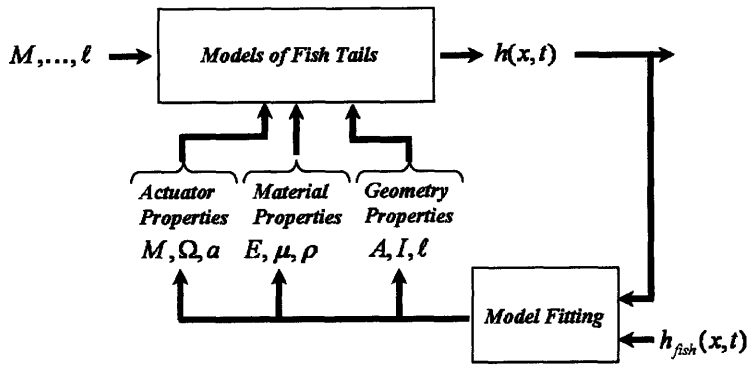

Figure 4-4: Curve fitting approach. The lateral body deflections $h(x,t)$ of a compliant fish-like body can be expressed in terms of actuation, material, and geometric properties. This model of lateral body deflections can then be compared to the required lateral body deflections $h_{fish}(x,t)$. The required actuator, material, and geometrical properties can then be found by minimizing the errors between the lateral deflection and required deflection.

bulk material properties E and μ, for the uniform geometry case ($A = cst, I = cst$), plotted versus body length ℓ and tail beat frequency f. Although the data in Figure 4-5 represents a bulk approximation, it provides a useful design tool since given a required body length (determined by load requirements) and tail beat frequency (determined by required average velocity), an engineer can find the approximate required material properties.

4.3.2 Approach 2: Computed Rigidity

A more accurate approach requires solving for the design parameters directly by inserting the target kinematics into the lateral dynamics governing equation. The lateral dynamics equation evaluated with the target kinematics can be rearranged as,

$$[EIh''_{req} + \mu I\dot{h}''_{req}]'' - \delta'(x-a)Msin(\omega t) = -(\rho A + m)\ddot{h}_{req} \tag{4.3}$$

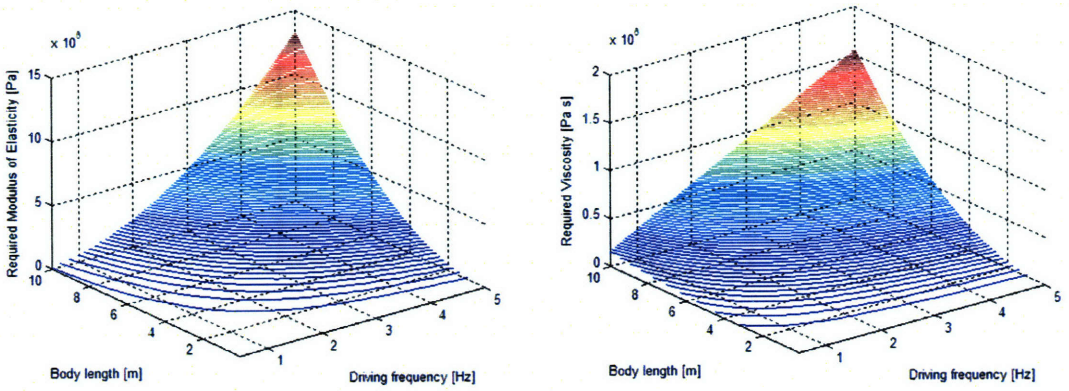

Figure 4-5: Required bulk material properties E and μ versus swimming frequency f and body length ℓ. Uninform geometry case.

For a given frequency $\omega = 2\pi f$, the only unknowns in the above equation are $E(x)$,$\mu(x)$,M, and a. Integrating once we find,

$$[EIh''_{req} + \mu I\dot{h}''_{req}]' - \delta(x-a)Msin(\omega t) = \int \Big[-(\rho A + m)\ddot{h}_{req} \Big] dxdx + C_1(t) \quad (4.4)$$

Integrating twice,

$$EIh''_{req} + \mu I\dot{h}''_{req} - u(x-a)Msin(\omega t) = \int\int \Big[-(\rho A + m)\ddot{h}_{req} \Big] dxdx + \int C_1(t)dx + C_2(t) \quad (4.5)$$

were C_1 and C_2 are non zero functions of time t that result from integration. The swimming kinematics model h_{req} is a low order approximation of the real motions of a fish, therefore, it is not sufficient to drive the right hand side of Equations (4.4) (shear) and 4.5(moment) to zero at the integration bounds ($x = 0$ and $x = \ell$). The swimming kinematics must be such that the moment and shear at both ends of the body are zero, as established by the boundary conditions of the problem. As noted by Lighthill [22], to address this issue rigid body motion components must be added to h_{req}. Mainly a component for rigid body translation and a component for rigid body rotation. Therefore, the real kinematics must be of the form,

$$h_R = h_{req} + (h_1 + h_3 x)cos(\omega t) + (h_2 + h_4 x)sin(\omega t)$$

where h_1, h_2, h_3, and h_4 should be chosen such that the right hand sides of Equations (4.4) and (4.5) vanish at $x = 0$ and $x = \ell$ [22]. Evaluating the derivatives of time and space h'', $\dot{h}''$, $\ddot{h}$, Equation (4.5) can be rearranged as,

$$sin(\omega t)\Big\{EIN + \mu I\omega G - u(x-a)M\Big\} + cos(\omega t)\Big\{ - EIG + \mu I\omega N\Big\} = sin(\omega t)S_1 - cos(\omega t)S_2 \quad (4.6)$$

where,

$$N = (H'' - Hk^2)cos(kx) - 2H'ksin(kx)$$

$$G = (H'' - Hk^2)sin(kx) + 2H'kcos(kx)$$

$$S_1 = \int_0^\ell \int_0^\ell \Big[(\rho A + m)H\omega^2 cos(kx)\Big]dxdx$$

$$S_2 = \int_0^\ell \int_0^l \Big[(\rho A + m)H\omega^2 sin(kx)\Big]dxdx$$

The cross sectional area A, second moment of inertia I, and added mass m can be represented as,

$$A(x) = \pi R(x)r(x), \quad I(x) = \frac{\pi}{4}R(x)r(x)^3 \quad m(x) = \pi\rho_f(2R(x))^2$$

where $R(x)$ and $r(x)$ are the major (z-direction) and minor (y-direction) radii of a given cross-section. For caranguiform and thunniform swimmers these geometrical features can be modeled by,

$$R(x) = R_1 sin(R_2 x) + R_3(e^{R_4 x} - 1) \quad (4.7)$$

$$r(x) = r_1 sin(r_2 x) + r_3 sin(r_4 x) \quad (4.8)$$

The values of the R_i and r_i constants can be found from real fish morphological characteristics obtained from [42, 43] and are listed in Table 4.3. Solving Equation

Parameter	Thunniform Swimmers	Caranguiform Swimmers
R_1	$\sim 0.1\ell$	$\sim 0.14\ell$
R_2	$\sim \frac{2\pi}{1.57\ell}$	$\sim \frac{2\pi}{1.6\ell}$
R_3	$\sim 0.00008\ell$	$\sim 0.0008\ell$
R_4	$\sim \frac{2\pi}{0.81\ell}$	$\sim \frac{2\pi}{1.1\ell}$
r_1	$\sim 0.055\ell$	$\sim 0.045\ell$
r_2	$\sim \frac{2\pi}{1.25\ell}$	$\sim \frac{2\pi}{1.25\ell}$
r_3	$\sim 0.08\ell$	$\sim 0.06\ell$
r_4	$\sim \frac{2\pi}{3.14\ell}$	$\sim \frac{2\pi}{3.14\ell}$

Table 4.3: Scalings for geometry parameters derived from fish morphology in [42, 43].

(4.6) is equivalent to solving the system,

$$\begin{cases} EIN + \mu I\omega G - u(x-a)M - S_1 = 0 \\ -EIG + \mu I\omega N + S_2 = 0 \end{cases} \tag{4.9}$$

Therefore, assuming M and a are known, for a given design frequency $\omega = 2\pi f$, the required material properties are given by,

$$\begin{aligned} E &= \frac{S_1N+S_2G+u(x-a)MN}{I(N^2+G^2)} \\ \mu &= \frac{S_1G-S_2N+u(x-a)MG}{I\omega(N^2+G^2)} \end{aligned} \tag{4.10}$$

However, it is also useful to know what are the conditions for which Equations (4.10) yield real physical values (i.e. $E \geq 0$, $\mu \geq 0$). The sign of both equations depends only on their numerator's signs. Therefore, the following inequality system,

$$\begin{cases} S_1F + S_2G + u(x-a)MN \geq 0 \\ S_1G - S_2F + u(x-a)MG \geq 0 \end{cases}$$

needs to be solved to find the conditions on H, κ, M and a that would ensure real physical solutions. Since the values for H and κ are constraint by the methodology, the only unknowns are M and a. The above equations assume a single concentrated moment, the general equations to solve for a generalized actuation moment distribu-

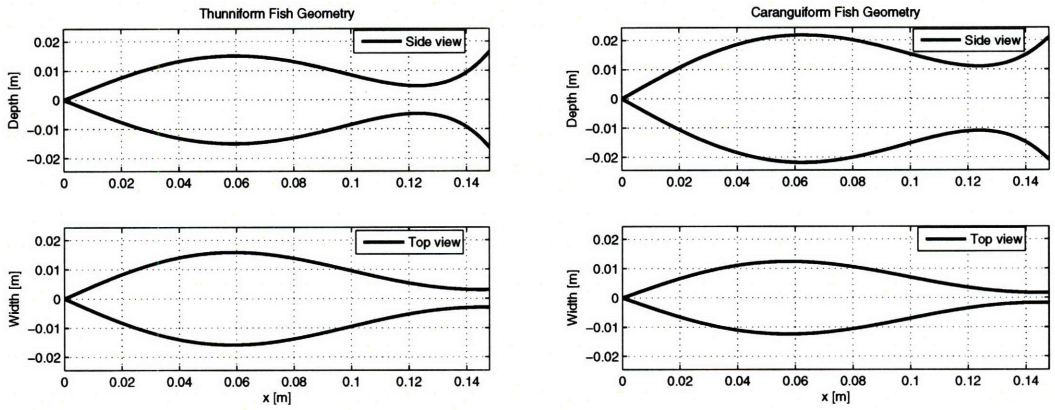

Figure 4-6: Geometries of thunniform and caranguiform bodies based on models in Equations (4.7) and (4.8).

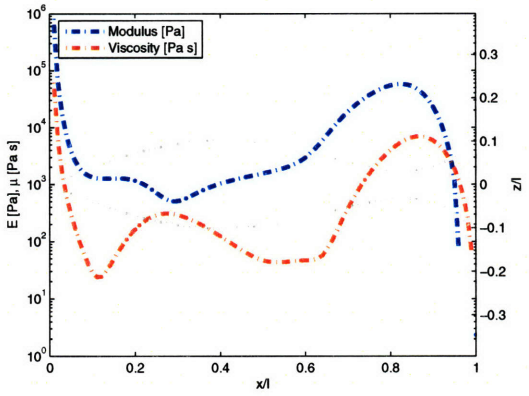

Figure 4-7: Required material distribution for thunniform fish ($\kappa = \frac{2\pi}{1.1\ell}$).

tion are,

$$\begin{cases} S_1F + S_2G + M(x)N \geq 0 \\ S_1G - S_2F + M(x)G \geq 0 \end{cases}$$

where $M(x)$ is the required moment distribution through the body which need not be a single concentrated moment. Figure 4-6 shows example geometries for thunniform and caranguiform swimmers used in the design methodologies. Figures 4-7 and 4-8 show the resultant material distributions for both examples. Figure 4-9 shows the graphical solution for the inequality system that defines conditions for real solutions. The grey region defines the actuation bounds that guaranty real physical solutions

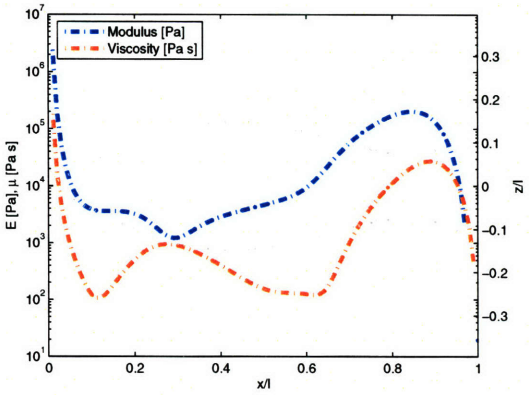

Figure 4-8: Required material distribution for caranguiform fish ($\kappa = \frac{2\pi}{1.1\ell}$).

for the material properties. The black solid line represents the particular actuation moment distribution $M(x)$ used to calculate material distributions shown in Figures 4-7 and 4-8. To understand and gain physical intuition on the results in Figures 4-7 and 4-8 it is useful to think of the force relations through the length of the body. Using the order of magnitude approximations in Equations (3.18) and (3.19) the dynamic behavior of any section of the fish-like body can be approximated by a mass-spring-damper system. The force relations of a given section can be characterized vectorially as shown in Figure 4-10. Figure 4-10 shows how local forces due to elasticity $\frac{EIH}{(\ell-x)^4}$, viscosity $\frac{\mu I\omega H}{(\ell-x)^4}$, and inertia $(\rho A + m)\omega^2 H$ balance with the local input force $\frac{M}{(\ell-x)^2}$ to satisfy the local amplitude H and phase ϕ. All the forces, except for the local input force, are related to local geometry through the values of $A(x)$ and $I(x)$. In addition, their vectorial balance changes as the required local amplitude H and phase ϕ change. The variations of A, I, m, H, ϕ, and M through the body length determine the required variations of E and μ. To visualize this an example can be studied. Figure 4-11 shows two graphs: the left graph shows the variations of $A(x)$, $I(x)$, and $m(x)$ through the body length of the caranguiform swimmer of Figure 4.6. The right graph displays the required amplitude $H(x)$ and phase $\phi(x)$. Table 4.4 summarizes the variations of A, I, m, H, ϕ, and M and corresponding variations of E and μ through the body length. The resulting material variations can be deduced from the vectorial force balance displayed in Figure 4-10 and the variations in the relevant

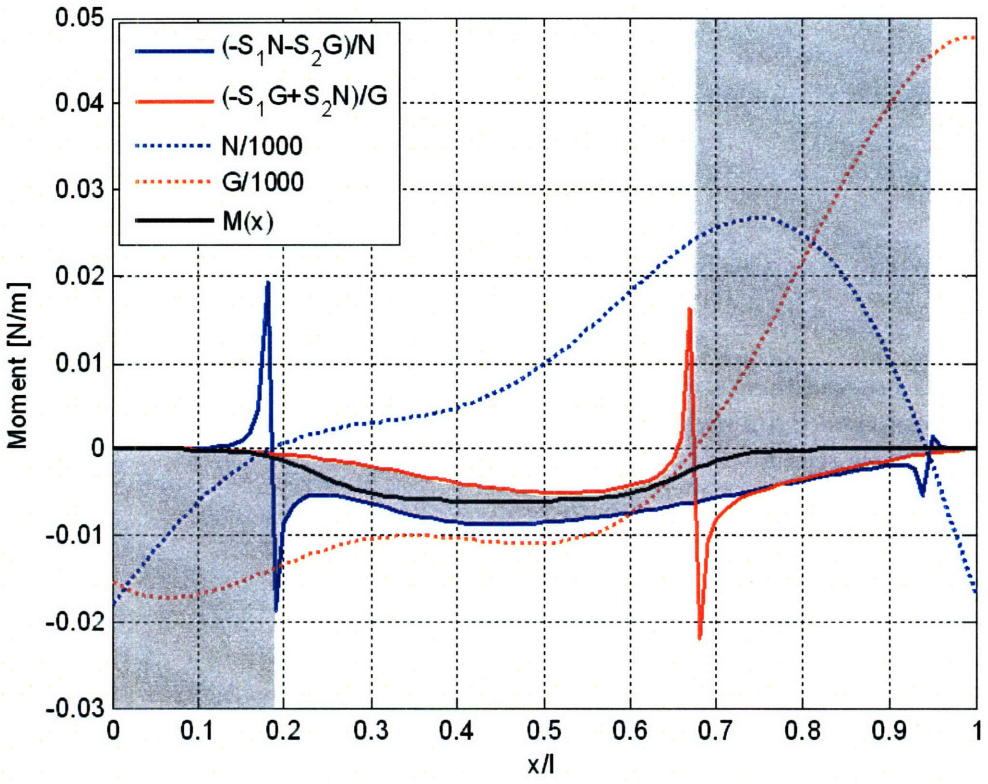

Figure 4-9: Graphical representation of inequality system defining the conditions for real positive values for $E(x)$ and $\mu(x)$. Gray region defines acceptable solutions. Scaled values for N and G are included to visualize the inequality sign changes.

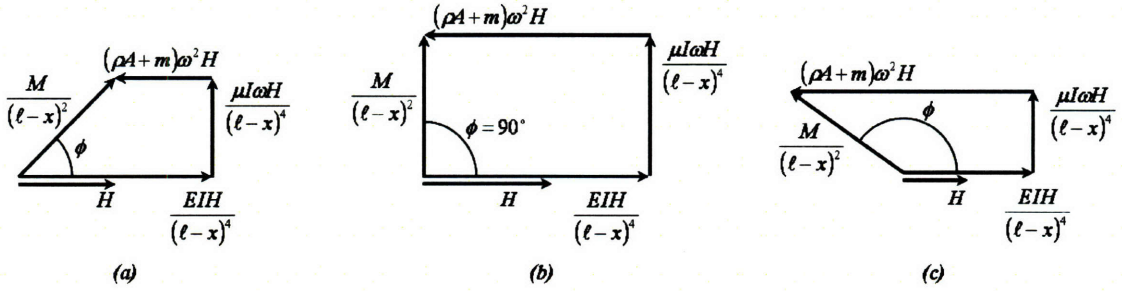

Figure 4-10: Vector relationship in forced vibration of fish-like elongated body. (a) Small phase lag. (b) Resonance, 90° phase. (c) Increasing phase lag.

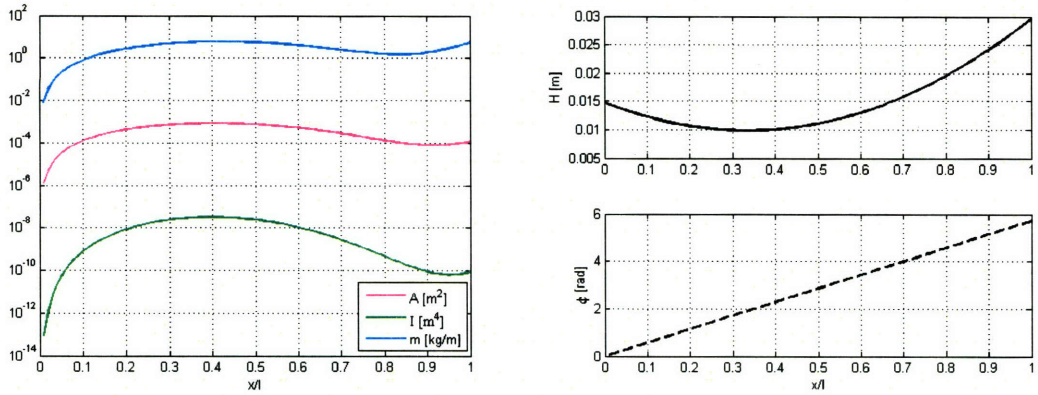

Figure 4-11: Cross-sectional area A, second moment of inertia I, and added mass m for caranguiform type swimmer of Figure 4-6 (left). Amplitude H and phase ϕ from required kinematics (right).

parameters. For $x \in [0, 0.1\ell[$, as the phase ϕ increases the elasticity force should increase to balance the increasing inertia force (both forces are proportional to H). Since the change in second moment of inertia I is greater than both the change in cross-sectional area A and added mass m, the modulus E should decrease to damp the larger increase in I and match the increase in inertia. Alternatively, the viscous force should match the local input force. Therefore, μ should also decrease to damp the larger increase in I. For $x \in [0.1\ell, 0.3\ell[$, the relation between the elastic force and inertia force remains the same, hence E should continue to decrease. However, the actuation moment M starts to decrease faster and the increase of I slows down, which causes the viscosity μ to increase in order to keep the balance between the viscous force and the input force. For $x \in [0.3\ell, a[$, the increase in I is of the same order as the changes in A and m. Therefore, to balance the higher increase in inertia force E should increase. Alternatively, the decrease in M diminishes which requires a smaller μ to keep viscous force and input force in balance. For $x \in [a, 0.9\ell[$, the decrease in I is greater than the decrease in both A and m, hence a bigger E is needed. While M is constant, H increases, therefore a smaller μ is needed. Finally, for $x \in [0.9\ell, \ell]$, A, I, and m increase again which causes both E and μ to decrease.

x	$[0, 0.1\ell[$	$[0.1\ell, 0.3\ell[$	$[0.3\ell, 0.4\ell[$	$[0.4\ell, a[$	$[a, 0.9\ell[$	$[0.9\ell, \ell]$
A'	+	+	+	-	-	+
I'	+	+	+	-	-	+
m'	+	+	+	-	-	+
H'	-	-	-	+	+	+
ϕ'	+	+	+	+	+	+
M'	-	-	-	+	+	+
E'	-	-	+	+	+	-
μ'	-	+	-	-	+	-

Table 4.4: Variations of A, I, m, H, ϕ, and M from examples in Figures 4-9 and 4-11 and corresponding variations of E and μ ($i' \equiv \frac{\partial i}{\partial x}$).

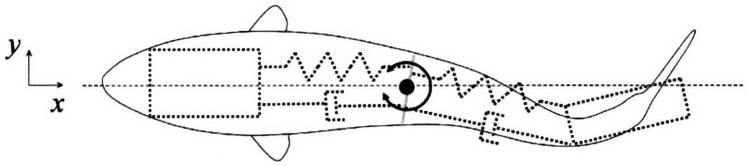

Figure 4-12: Lumped parameter model.

4.3.3 Approach 3: Lumped Parameters

Finally, the advantages of achieving continuous material distributions are clear since bulk material properties generate swimming kinematics errors and result in diminished swimming performance. However, the required material distributions might not be physically realizable, either because the required materials do not exist or simply because an structure with those particular distributions might not be easily manufactured. An intermediate solution would be to partition the body into regions with different bulk material properties. If the same actuation location is used, then the bulk material properties of each region correspond to average values of the corresponding local distributed solutions found using the previous approach. An advantage of this approach would be to increase the performance over bulk designs (approach 1) while still being physically realizable. The dynamics of each section can then be modeled using lumped parameters. A simple example of this approach can be illustrated by splitting the body in two regions. As seen in the previous chapter, for the case of caranguiform an thunniform swimmers, a mass-spring-damper model can be used to

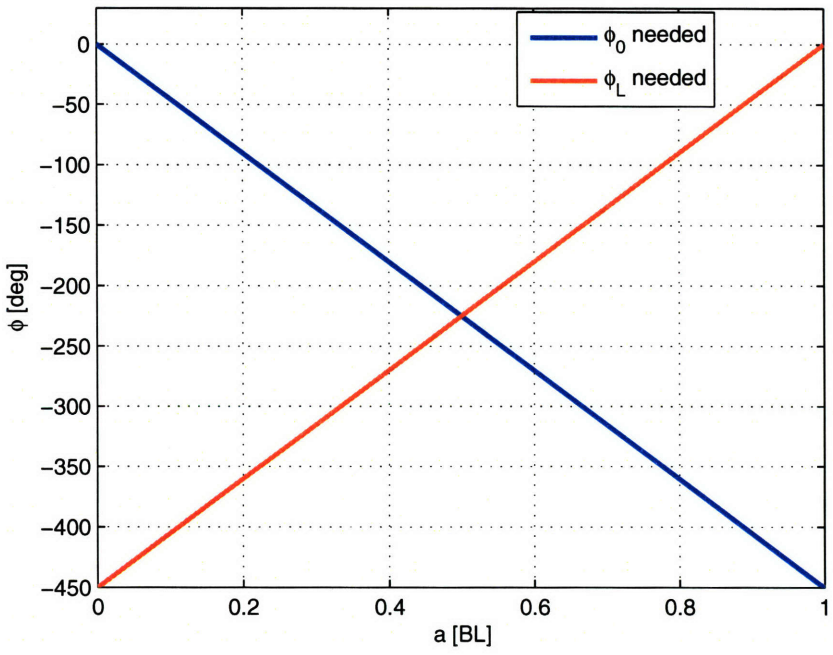

Figure 4-13: Required head and tail phases.

estimate the motions of the tail with respect to the motions of the body. The same approach can then be taken to estimate the motions of the head. Figure 4-12 shows a lumped parameter model for a compliant body with two discrete regions that are coupled by actuation. Since the phase between head an tail must have a constant value, $\phi(\ell) = \kappa\ell$, an approach is to first select a tail material that achieves the appropriate lateral deflections. This can be accomplished using the second order model approximation for amplitude H given by Equation (3.18). If actuation moment M, geometry of the tail, and the desired amplitude H are known, the designer can chose a known material with given E and μ to solve for the required actuation location a. Alternatively, if the actuation location a must be fixed due to geometry constraints, then several solutions for the required material are possible and would only differ on their resultant phase. To help in the selection process, when designing a body with two sections, a diagram such as the one in Figure 4-13 can be used. Figure 4-13 shows the required phase versus actuation location a for both head and tail ends when the required phase is known. For this example, $\phi(\ell) = \frac{2\pi}{0.8} = 450°$. For a given

set of material properties the phase between the tail oscillations and the actuation is given by the red line. If the actuation location is chosen as $a = 0.6\ell$, the tail lags the actuation by $\sim 180°$, then the required phase between the head oscillations and actuation is given by the point on the blue line at $a = 0.6\ell$ where the head lags the actuation by $\sim 270°$. Therefore the total phase difference between head and tail results in $\phi = -180° - 270° = -450°$ which was the original target. The required material properties for the head section can then be found from Equations (3.18) and (3.19) using the desired actuation location and the resulting required head phase. The same can be done if the phase of the head section is known a priori, in that case, the required tail phase is found and the corresponding material properties can again be found using Equations (3.18) and (3.19).

4.4 Summary

This chapter presented three design methodologies that can be used to solve for the design parameters $(E, \mu, \rho, A, I, m, \ell, M, \Omega, a)$ needed to achieve a particular target swimming kinematics and the resulting desired propulsion performance. In order to identify appropriate target kinematics h_{req}, scalings for the swimming kinematics model parameters (a_1, a_2, a_3,and κ) were identified from experimental data. The first design approach assumed a swimming device with constant beam-like geometry and solved for the bulk material properties E and μ required to approach the desired swimming kinematics h_f. This was achieved by fitting the required kinematics data with a simplified parametric model of the lateral body vibrations and solving for the design parameters that would minimize the fitting error. A more accurate approach consists of plugging the required swimming kinematics h_{req} into the dynamic model of body lateral deformations and solving for material distributions $E(x)$ and $\mu(x)$. Actuation bounds that guaranty real physical solutions can also be found. Finally, using the results of the more accurate approach, the prototype's body can be modeled using lumped parameters and required bulk material properties of individual body sections can be found.

Chapter 5

Prototype Designs and Fabrication

This chapter presents the designs of compliant biomimetic swimmers that result from the methodologies described in the previous chapter. The main design features for thunniform and caranguiform type swimmers are described along with the techniques used for their fabrication. This new class of biomimetic mechanisms is simpler and more robust than present biomimetic mechanisms. A list of part suppliers can be found in Appendix D.

5.1 Prototype Designs

This section describes the designs of caranguiform and thunniform swimmers. Figure 5-1 displays top and side views of the morphology typical of caranguiform and thunniform swimmers, the geometries were adapted from real fish specimens documented in fish morphology literature [42, 43]. The morphological differences among these two types of swimmers are not extreme. The differences occur mostly on the geometries of the tail and caudal fins. In aerodynamics and fluid dynamics an important feature for the study of the forces generated by wings and fins is their aspect ratio. The aspect ratio of a fin is defined as the span (length) squared divided by fin area. A high aspect ratio fin has a long and narrow geometry whereas a low aspect ratio fin displays a short and stubby geometry. Thunniform swimmers have high aspect ratio caudal fins and while the profile of the body ($2R$) tapers towards the caudal fin,

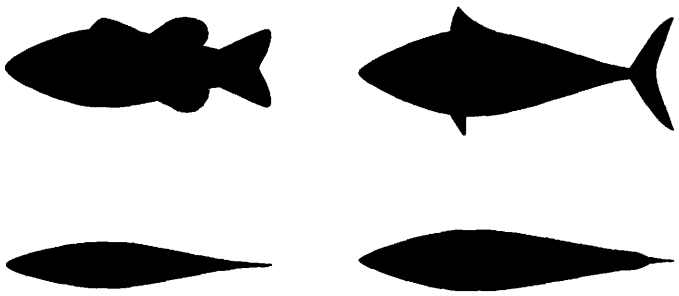

Figure 5-1: Fish geometries: (a) Caranguiform swimmers side and top views, (b) Thunniform swimmers side and top views. The geometries are based on illustrations and photographs from biological samples [42, 43].

the thickness ($2r$) is kept pronounced. In addition, the body mass and volume are concentrated towards the anterior parts of the body and the nose is streamlined. In contrast, caranguiform swimmers do not have high aspect ratio caudal fins and both their profile and thickness taper towards the caudal end. However, while their profile tapers towards the caudal fin it remains considerably thick in comparison to the thunniform's profile. The prototypes presented in this section share three common features:

- An actuation mechanism that implements a concentrated moment distribution $M(x)$.

- A compliant body that implements the geometry constraints (A_{fish}, I_{fish}, m_{fish}, ℓ_{fish}, ρ_{fluid}, ω) and approximations of the material distributions ($E(x), \mu(x)$) identified through the design methodologies of the previous section.

- Hardware and electronics that control actuation.

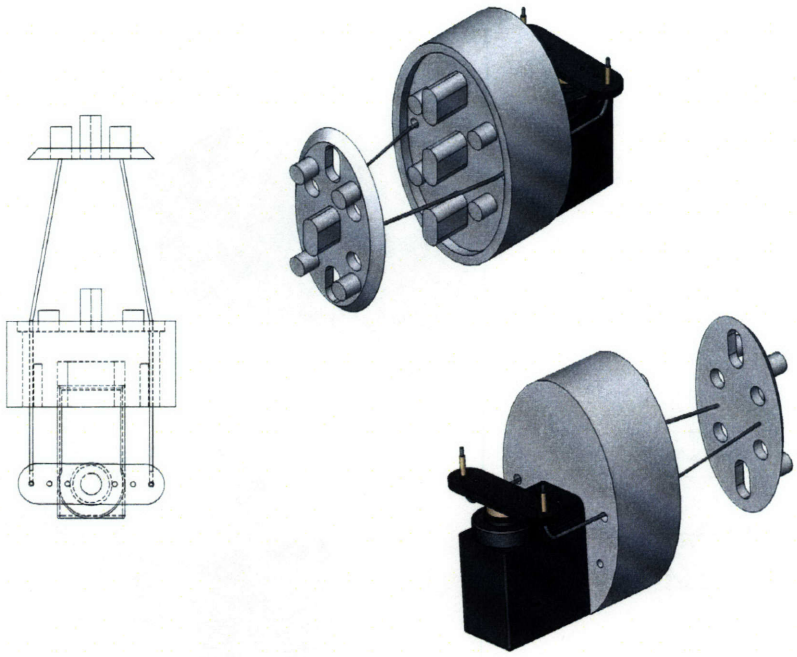

Figure 5-2: Cable torque transmission.

5.1.1 Actuation Mechanism

The required actuation can be implemented using rotational or linear actuators. For the design examples presented in this chapter, RC (radio control) servo motors are used. Figures 5-2 and 5-3 display different views of two transmission designs used in the prototypes. A transmission consists of a servo, a servo support, a rigid plate, and a mechanisms to transmit the servo forces to the rigid plate. A chosen transmission mechanism is then embedded inside the fish-like compliant body. During actuation, the transmission rigid plate applies the forces from the servo to the compliant body. Figure 5-2 shows a transmission mechanism that uses two cables attached to a servo motor to transmit torque to the rigid plate. Figure 5-3 shows an alternative mechanism that uses a flexure linkage connected to the rigid plate to transmit the required torque to a section inside the body. In this configuration the servo arm acts as the coupler link and the rigid plate is the ground link. The cable mechanism is simpler and more easily scalable. However, during a cycle the cable mechanism only transmits

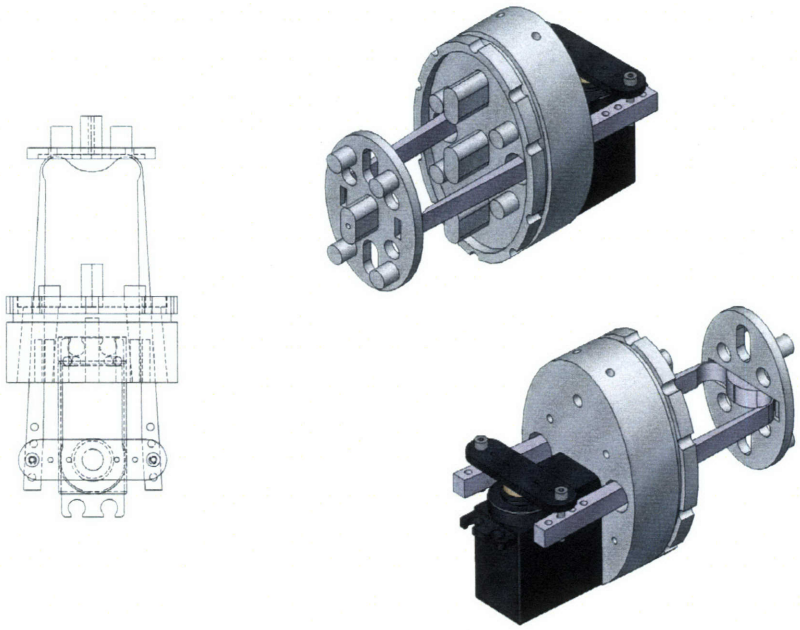

Figure 5-3: Flexure 4-bar torque transmission.

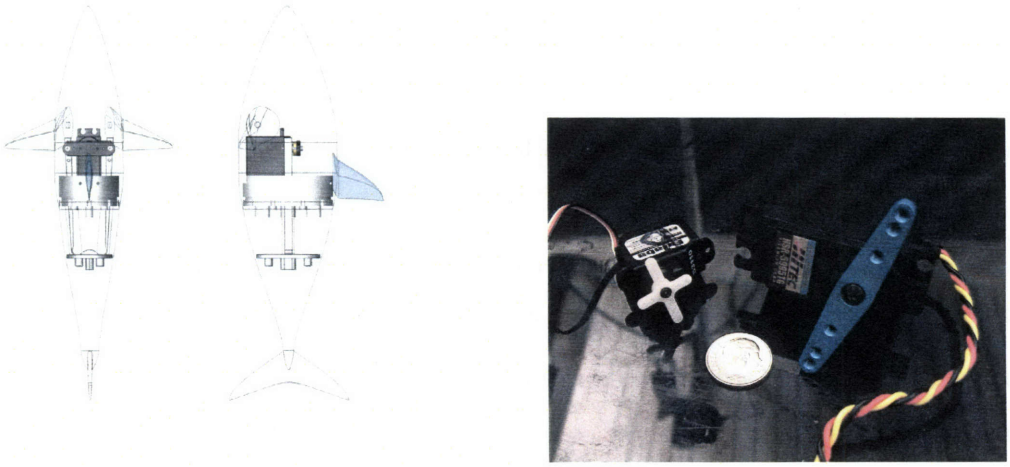

Figure 5-4: Location of embedded transmission and RC servos used for actuation.

servo forces through one cable at a time. In contrast, the flexure mechanism transmits servo forces through both links during the entire actuation cycle. However, the flexure mechanism requires cavities around the links so that the body material does not oppose their motions through friction. As a result, the implementation of this mechanisms is more challenging. The particular geometries of the rigid plates are an additional important feature of the transmission designs. The geometries on the rigid plates and servo supports present complex geometries to increase their surface area and maximize adhesion to the flexible body material. Figure 5-4 shows the location of an embedded transmission and the typical RC servos used. Once a transmission is embedded, the space in between the rigid plate and the servo motor is filled by body material as shown in Figure 5-4.

5.1.2 Compliant Bodies

The prototypes presented in this chapter mimic caranguiform and thunniform swimmers and their geometries are adapted from biological studies. Figures 5-5 and 5-6 display views of basic caranguiform and thunniform swimmer designs respectively. These simple designs are powered and controlled through an umbilical cord (not shown). Their main purpose is for testing forward propulsion capabilities, and their maneuverability is limited to biasing the tail beat amplitude. Umbilical cords are needed in prototypes for power consumption and locomotion efficiency measurement. Improved maneuverability can be achieved through the addition of individually controlled side fins. Figures 5-7 and 5-8 show two thunniform swimmer designs that use individually controlled (pitch control) fins. Figure 5-7 displays a design mimicking a tuna which is still powered and controlled through and umbilical cord (not shown). Figure 5-8 displays a shark inspired design with onboard power supply and control hardware.

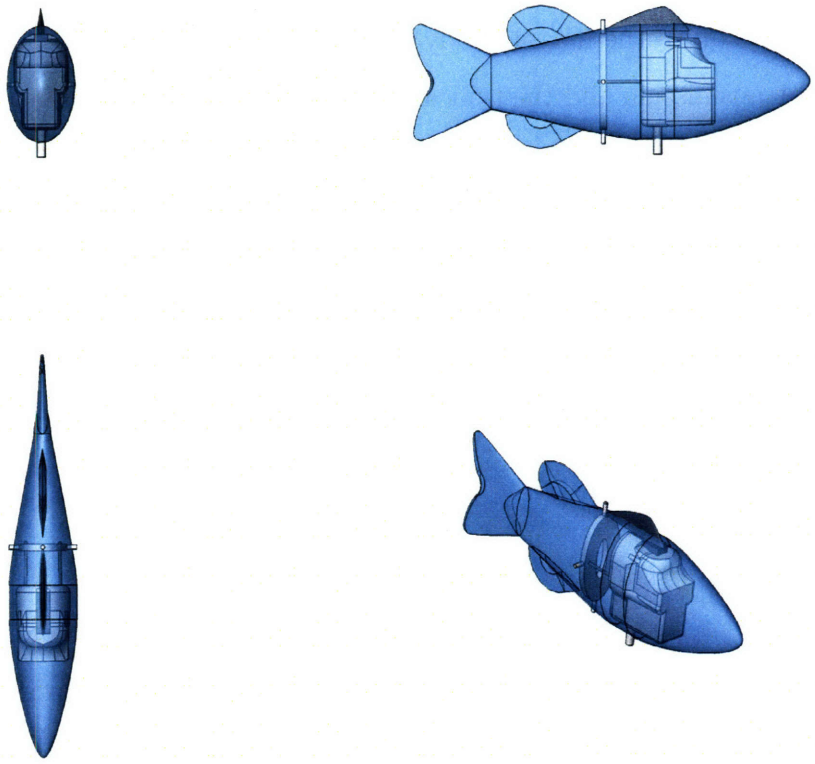

Figure 5-5: Basic caranguiform swimmer design: compliant body with embedded cable actuation transmission. Power and control signal are carried by umbilical cord (not shown).

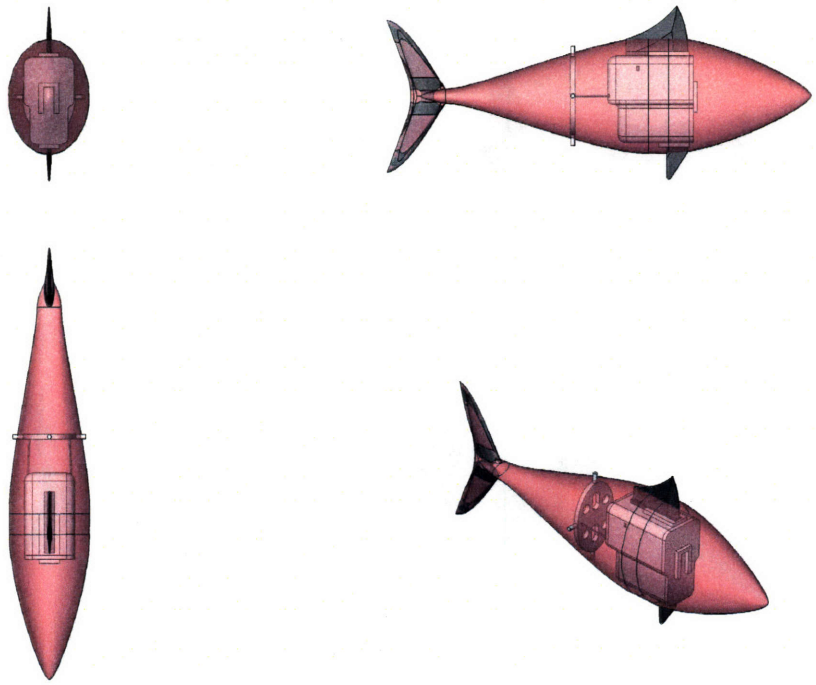

Figure 5-6: Basic thunniform swimmer design: compliant body with embedded cable actuation transmission. Power and control signal are carried by umbilical cord (not shown).

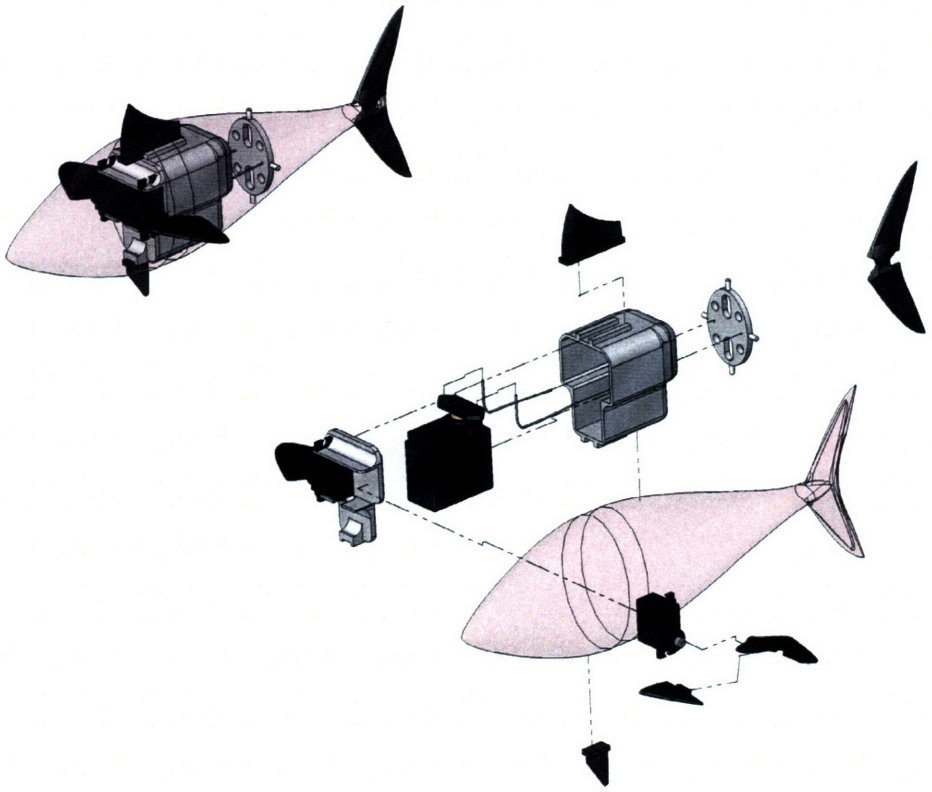

Figure 5-7: Tuna inspired swimmer with individually controlled side fins. Power and control signal are carried by umbilical cord (not shown).

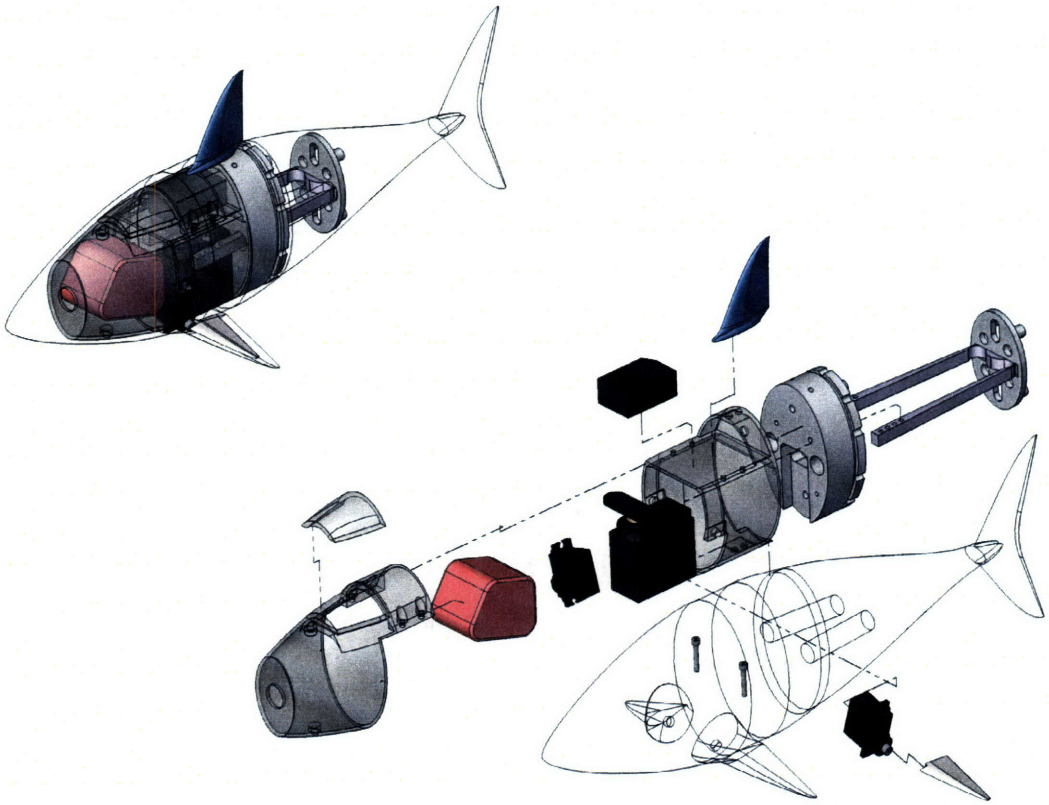

Figure 5-8: Shark inspired swimmer with individually controlled side fins. Power (batteries) and control hardware (microcontroller) are embedded inside the body.

5.1.3 Control Hardware

Prototypes can be operated by conventional radio control or through a microcontroller. Figure 5-9 displays the traditional components for radio control: a receiver (left), an RC servo (right), and a transmitter (left). RC servo motors are traditionally used in position control applications. In order to apply the sinusoidal varying input forces that result in desired tail beat frequencies, the RC servos are driven dynamically. For this purpose, a traditional transmitter can be modified by changing a servo channel input from the traditional potentiometer to a function generator or timing circuit providing a sinusoidal or triangular wave. Figure 5-9 (right) shows a standard transmitter with the channel modification and an additional input connector for a function generator.

Alternatively, prototypes can also be controlled through a microcontroller. Figure 5-10 shows the microcontroller chip (left), wireless components (center), and the board assembly (right) used to control some of the example designs presented in this chapter. A DSP56F803 MPU, 16 bit processor $Plugapod^{TM}$ chip from NewMicros, Inc. was chosen. The chip ($0.04m \times 0.035m \times 0.015m$) main features include the capability of 40 MIPS at 80 MHz, on chip flash EEProm and RAM, 24 general purpose digital I/O lines, 4 wire SPI interface, 6 general purpose timers, 6 PWM outputs, 3 led control lines, 1 RS-232 shutdwon line, two 4-channel 12 bit ADCs, and onboard 5.0V and 3.3V linear regulators. Four programming languages, $IsoMax^{TM}$, Forth, Small C, and Static C, are compatible with the microcontroller operating software. In addition $ZigBee^{TM}$ RF modules from $XBee^{TM}$ are used to establish a wireless connection between a microcontroller an a host computer. A transmitter-receiver module is stacked on top of the microcontroller chip, as shown in Figure 5-10 (right), and a transmitter-receiver dongle is connected to the USB port of the host computer (not shown) establishing a wireless communication channel with an indoor range of 100 m and outdoor line-of-sight range of 1.6 km.

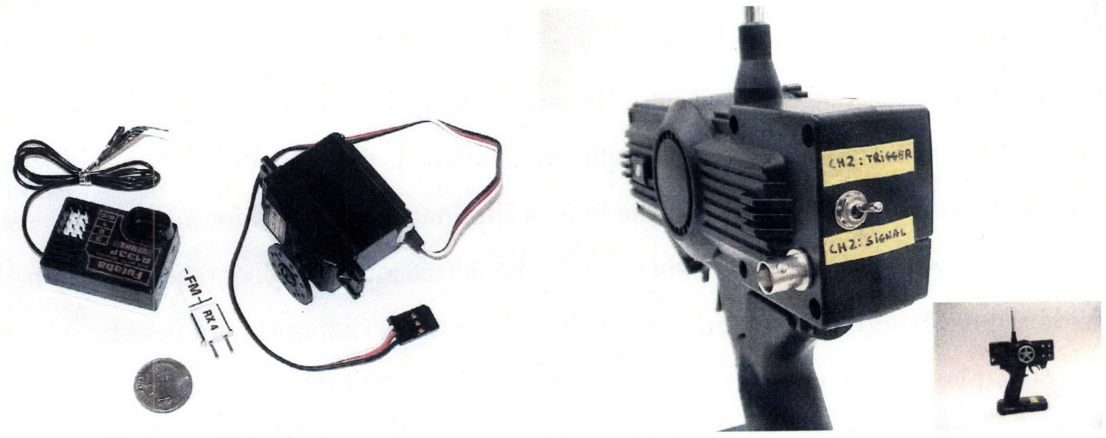

Figure 5-9: Traditional radio control components: receiver (left), servo (center), and transmitter (right). A standard transmitter can be modified to drive RC servos dynamically, by connecting a function generator or timing circuit to the channel inputs instead of the traditional potentiometers.

Figure 5-10: *Plugapod*^{TM} microcontroller chip (left), *ZigBee*^{TM} wireless components (center), and board assembly (right) used to control prototypes.

5.2 Fabrication Techniques

The actuation mechanisms described in the previous section along with control and power hardware are encapsulated inside a prototype's body. A two part mold with the negative shape of a selected body geometry is first machined out of wax. Wax is used for two main reasons: it can be quickly machined, and it does not adhere to the elastomer compounds used to cast the bodies eliminating the need for an extra release coat when casting. Figure 5-11 shows how the actuation components are positioned inside a mold before casting. Internal parts such as servo supports, fin inserts, or any other complex components are rapid-prototyped using 3D printers in order to increase the compactness of the parts. Once the internal parts are positioned inside a mold, the mold is closed and an elastomer compound is poured in through mold openings. Elastomer compounds such as silicone an urethane gels are used because of their viscoelastic material properties as well as their chemical and temperature resistance. The procedure used to characterize the physical properties of the materials used in the prototypes is described in Chapter 6, and experimental data for some examples is also presented. After the elastomer compound cures, the body of the device protects the internal parts form the environment. Figure 5-12 shows the fabrication steps of a tuna inspired prototype and Figure 5-13 displays different views of the finished device. The grooves observed along the body surface are due to mold finish. The required material distributions $E(x)$ and $\mu(x)$ found through the computed rigidity design methodology outlined in Chapter 4 can not be achieved using casting techniques. Instead, these results are used to identify body sections that can be casted using bulk material properties and approximate the required material distributions. Appropriate bulk material properties for each section are found through the lumped parameter design methodology. Figure 5-14 shows the fabrication steps of a shark inspired prototype. Images of several completed caranguiform and thunniform prototypes used for testing are shown in Figure 5-15. Table 5.1 summarizes the features of some of the caranguiform and thunniform prototypes built.

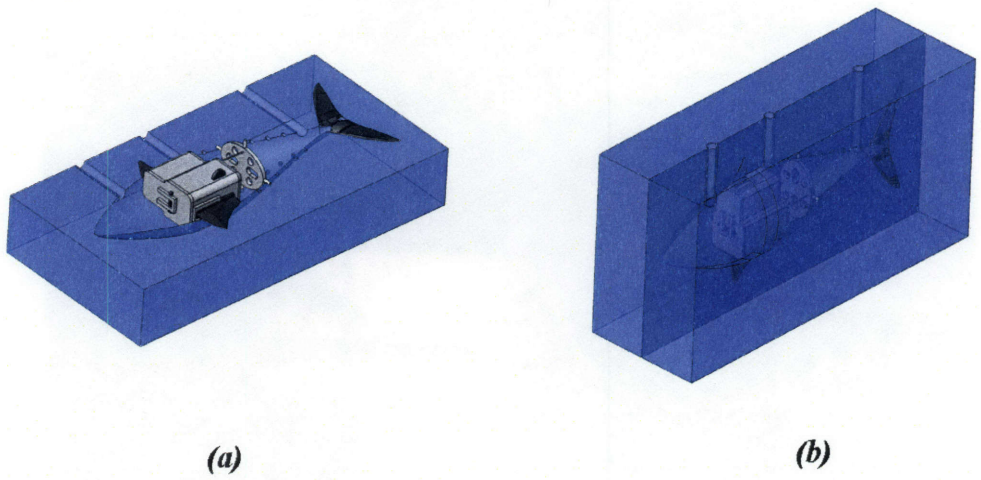

Figure 5-11: Casting procedure: (a) Actuation mechanisms and other required hardware are positioned inside a two part wax mold. (b) Mold is closed and elastomer compounds used to cast the compliant fish-like body can be poured through mold openings.

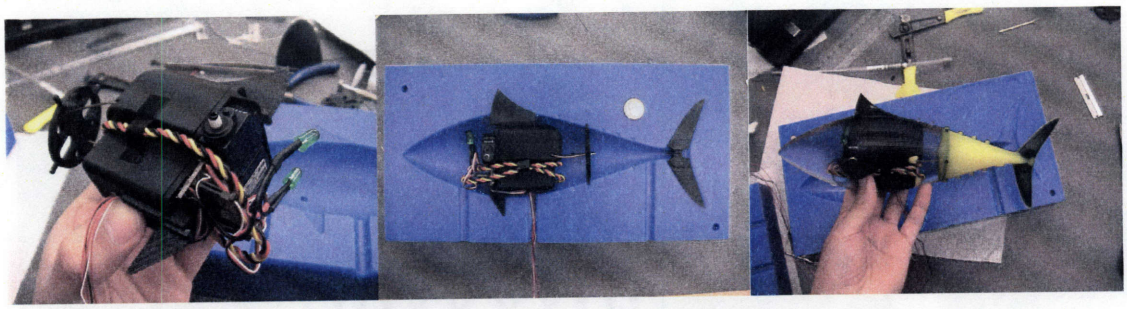

Figure 5-12: Tuna fabrication example: Actuation mechanism with cable transmission and individually controlled side fins is assembled using rapid prototyped parts (left). Hardware components are positioned inside mold (center). Finished prototype is taken out of mold after elastomer compounds are cured (right).

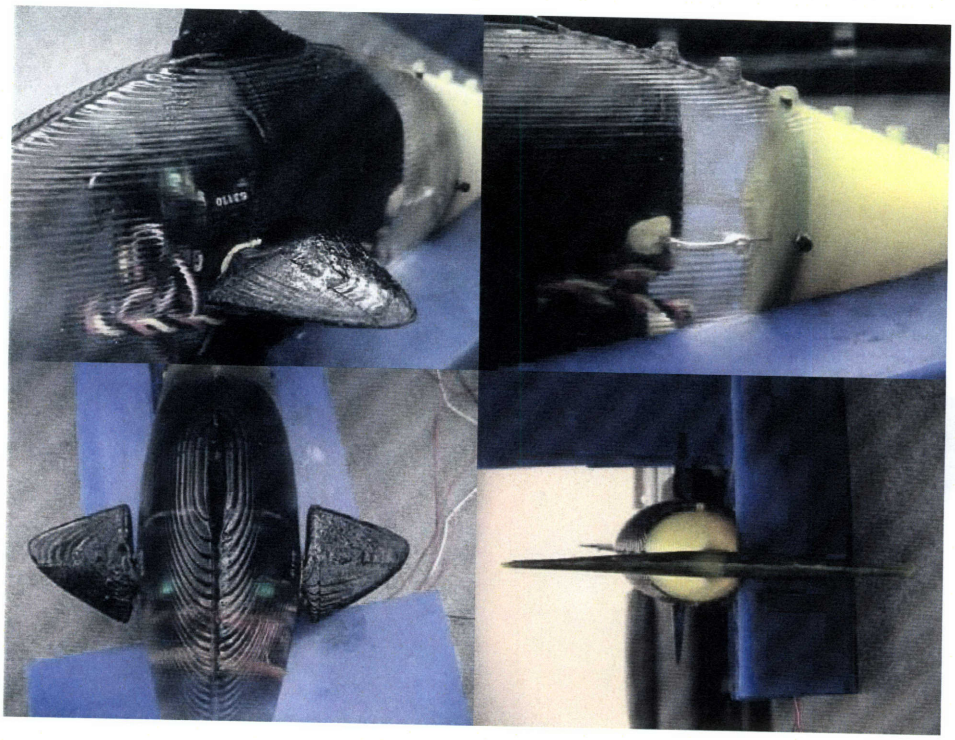

Figure 5-13: Tuna inspired prototype views of side fins, embedded cable transmission, and caudal fin. Body surface grooves are due to mold finish.

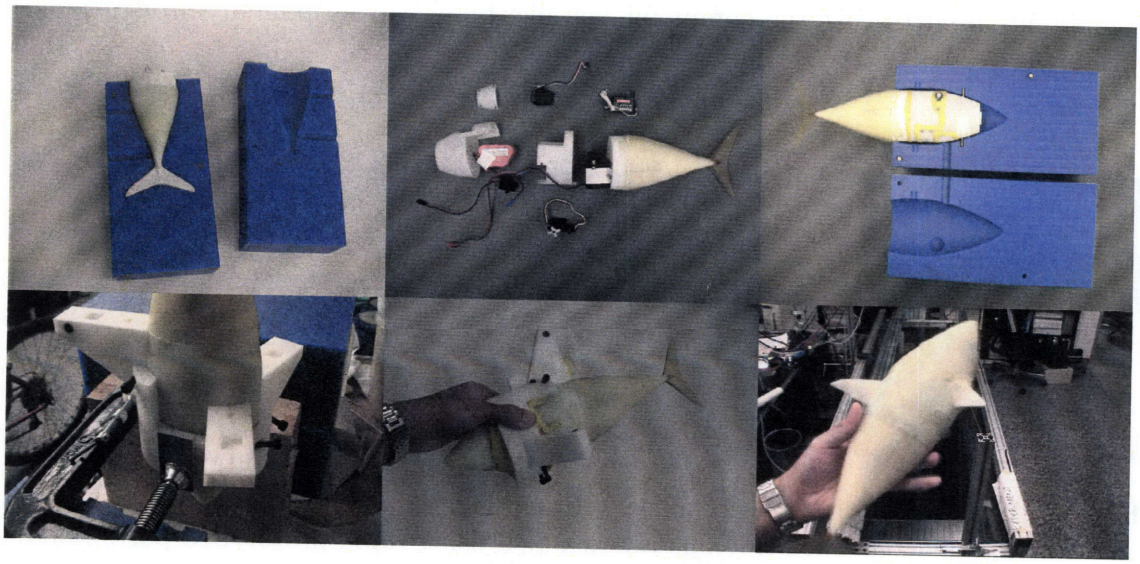

Figure 5-14: Shark fabrication example.

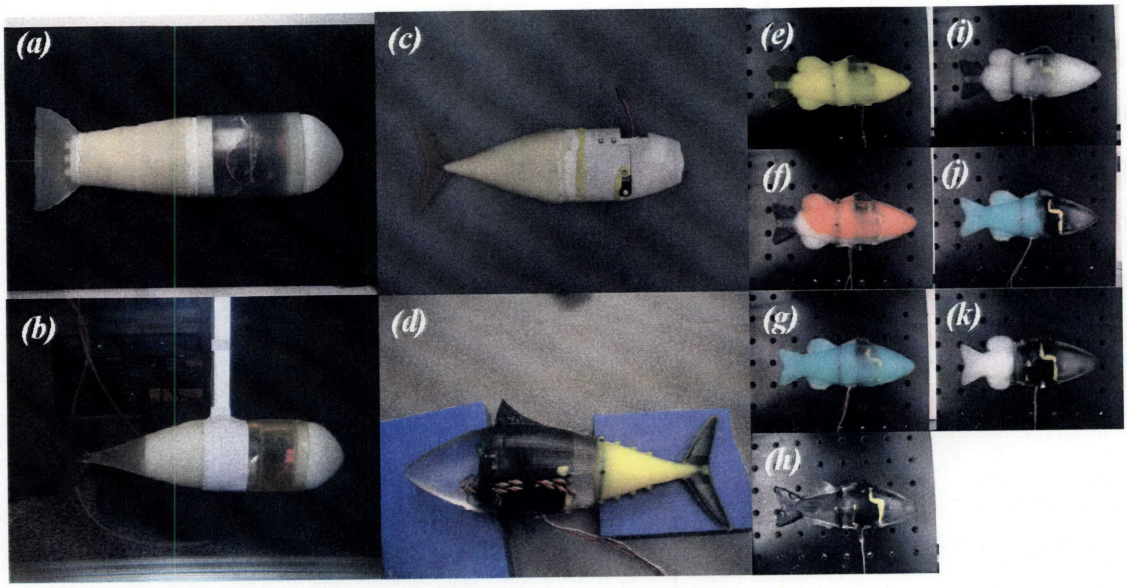

Figure 5-15: Prototypes: (a) Big bass, (b) Tuna, (c) Shark 3, (d) Hybrid tuna, (e) Yellow bass, (f) Orange bass, (g) Green bass, (h) Clear bass, (i) White bass, (j) Hybrid bass 1, (k) Hybrid bass 2.

Prototype	$E[N/m^2]$	$\mu[Ns/m^2]$	$\rho[kg/m^3]$	$\ell[m]$	$a[m]$	$M[Nm]$
Big Bass	48624	25.8	~1000	0.3	0.18	1.4
Tuna	48624	25.8	~1000	0.3	0.18	1.4
Shark 3	48624	25.8	~1000	0.32	0.21	1.4
Hybrid Tuna	37367, $x \in [0, 0.6\ell[$ 95650, $x \in [0.6\ell, \ell]$	52.3, $x \in [0, 0.6\ell[$ 90, $x \in [0.6\ell, \ell]$	~996	0.26	0.16	1.4
Yellow Bass	95650	90	~1000	0.148	0.074	0.1
Orange Bass	64820	68	~1000	0.148	0.074	0.1
Green Bass	56610	82	~1000	0.148	0.074	0.1
Clear Bass	37367	52.3	~970	0.148	0.074	0.1
White Bass	97835	92.3	~998	0.148	0.08	0.1
Hybrid Bass 1	37367, $x \in [0, 0.6\ell[$ 56610, $x \in [0.6\ell, \ell]$	52.3, $x \in [0, 0.6\ell[$ 82, $x \in [0.6\ell, \ell]$	~1000	0.148	0.074	0.1
Hybrid Bass 2	37367, $x \in [0, 0.6\ell[$ 97835, $x \in [0.6\ell, \ell]$	52.3, $x \in [0, 0.6\ell[$ 92.3, $x \in [0.6\ell, \ell]$	~1000	0.148	0.08	0.1

Table 5.1: Prototype material, geometric, and actuation parameter values.

5.3 Summary

This chapter presented prototype designs and techniques used to fabricate caranguiform and thunniform devices with compliant bodies. The different actuation mechanisms, geometrical characteristics, and control hardware used were listed and their features detailed. The required material distributions $E(x)$ and $\mu(x)$ were approximated by compliant bodies with multiple sections having individual bulk material properties.

Chapter 6

Performance Characterization

This chapter presents the experimental setups and procedures used to characterize the performance of compliant biomimetic swimmers designed according to the guidelines developed in Chapter 4. The results for thunniform and caranguiform swimmers are discussed and used to validate the performance models developed in Chapter 3.

6.1 Objectives

The objectives of the performance characterization are to verify the validity of the performance models, identify the limits of performance, and test the sensitivity of swimming performance to design parameter variations. To this end, the models developed in Chapter 3 are compared to experimental results. The experimental setups for each measurement are presented along with a detailed description of the procedures for testing. First, the material properties of the elastomer compounds used in the prototypes are characterized. Next, the measurements of swimming kinematics are presented and analyzed. In addition, swimming performance measurements are presented and their agreement with analytic models discussed. Finally, the limits of swimming performance and sensitivity to parameter variations are discussed in the context of the experimental results for both thunniform and caranguiform swimmers.

6.2 Material Properties

In the analysis of Chapter 3, a very simple model was assumed for the visco-elasticity displayed by the materials used in the prototype bodies. Mainly, the total resistive force was assumed to be analogous to the force exhibited by a capacitance (spring) and a resistance (dashpot) connected in parallel and resulting in a stress of the form,

$$\sigma = E\epsilon + \mu\frac{\partial\epsilon}{\partial t} \tag{6.1}$$

The validity of this model can be tested by performing a dynamic analysis on material samples. Elastomer compounds were chosen as the primary materials for the prototype's bodies due to their chemical and temperature resistance.

A dynamic mechanical analyzer (DMA) was used to perform the dynamic tests. The DMA subjected elastomer samples to constant amplitude strain loadings at different frequencies while controlling the environment's temperature. The results of this type of tests are shown in Figure 6-1 for 4 types of elastomers, IE10 (polyurethane), TD100-11 (polyurethane gel), Q300 (silicone gel), and EcoFlex 0010 (silicone rubber) at different strains values. All the elastomers used were two-part (resin and hardener) room temperature cure compounds. For the silicone rubber, EcoFlex 0010, several pigments were tested to gauge changes in material properties due to pigment addition. In addition, a silicone gel, Q300, was tested with two different mixing ratios. The experimental data in Figure 6-1 shows the measured stress σ (top graph) for a given strain magnitude ϵ (bottom graph) versus strain rate $\frac{\partial\epsilon}{\partial t}$ in Hz. For a given strain magnitude ϵ, the measured stress σ increases with increments in the applied strain rate $\frac{\partial\epsilon}{\partial t}$. Furthermore, increasing the stress magnitude ϵ results in an overall increase of stress σ. Both observations agree with the simple model in Equation (6.1). At the limit where the strain rate is very slow ($\frac{\partial\epsilon}{\partial t} \to 0$), its effect on the resulting stress can be ignored and the modulus of elasticity E can be estimated as $E \approx \frac{\sigma}{\epsilon}$. In addition, since the measured stress-strain relation can be approximated by the linear model in Equation (6.1), the viscosity μ is the slope of the resulting line and its value can then be identified from a linear fit of the measured data. Figure 6-2 shows a linear

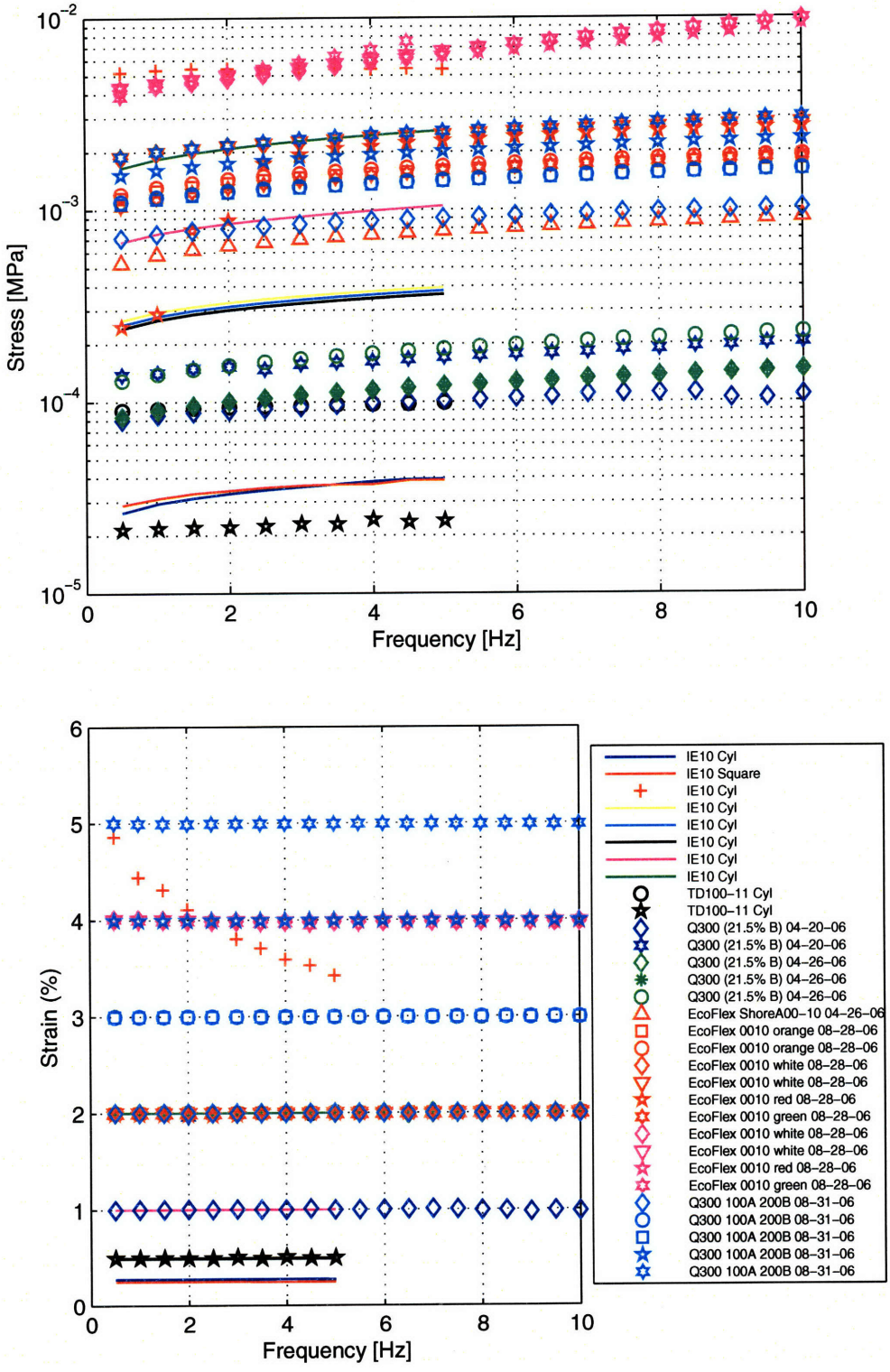

Figure 6-1: Dynamical mechanical analyzer experimental results.

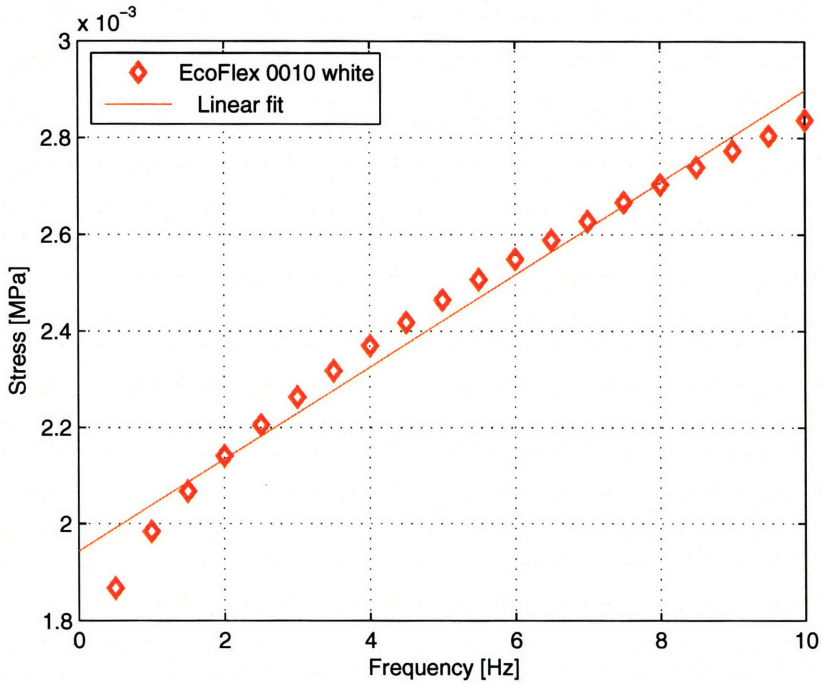

Figure 6-2: Linear fit of experimental data for EcoFlex 0010 sample without pigmentation.

fit superimposed on experimental stress data for and Ecoflex 0010 sample without pigmentation.

The strain magnitude ϵ chosen for the experiments is crucial in order to characterize values for the modulus E and viscosity μ that are relevant to the prototype dynamics. For a swimming prototype, the strain magnitudes vary at different locations through its body. Therefore, choosing the appropriate strain for the stress estimation is extremely important. The local radius of curvature ζ in an elongated body undergoing bending, with small amplitude lateral deflection, can be approximated by the local second derivative of the lateral motions,

$$\frac{1}{\zeta} \approx \frac{\partial^2 h}{\partial x^2}$$

Material	Type	ϵ	$E[N/m^2]$	$\mu[Ns/m^2]$
IE10	Polyurethane	0.005	48624	25.8
TD100-11	Polyurethane gel	0.005	4221	0.6
Q300 (1A-1.215B)	Silicone gel	0.02	4373.6	6.4
Q300 (1A-2B)	Silicone gel	0.03	37366.6	52.3
EcoFlex 0010 (no pigment)	Silicone rubber	0.02	97835	92.3
EcoFlex 0010 (orange pigment)	Silicone rubber	0.02	64820	68
EcoFlex 0010 (red pigment)	Silicone rubber	0.02	38417	232
EcoFlex 0010 (green pigment)	Silicone rubber	0.02	56610	82
EcoFlex 0010 (yellow pigment)	Silicone rubber	0.02	95650	90

Table 6.1: Measured material Properties.

Using the same coordinates as in the analysis of Chapter 3, the local strain is then,

$$\epsilon \approx -y\frac{\partial^2 h}{\partial x^2}$$

which can be approximated as,

$$\epsilon \sim r^*\frac{H^*}{(\ell^*)^2}$$

where r^* is the local minor radius (y-direction) of the body cross-section, H^* is the amplitude of the local lateral motion, and ℓ^* is the section length. Using this expression, estimates of the maximum stresses that can arise inside the body of a prototype can be found. For the tested prototypes and the kinematics under study,

$$\epsilon \in [0.005, 0.03]$$

Measured material properties for the polyurethane and silicone compounds tested are listed in Table 6.1 as well as the strain magnitudes used in the experiments.

6.3 Prototype Kinematics

6.3.1 Experimental Setup

Figures 6-3, 6-4, and 6-5 show the experimental setup and the different configurations used to characterize a prototype's swimming kinematics. The setup consists of a $2.5m \times 0.6m \times 0.6m$ acrylic tank surrounded by an aluminum frame. The frame allows for an easy implementation of additional sensors and support hardware. Available support hardware includes a power supply for the prototypes and sensors used and a DSpace data acquisition and real time control interphase. The frame can support a digital camera as shown in Figure 6-4. The digital camera used in the experiments is a Sony DCR-TRV30 NTSC MiniDV digital camera with a 30 frames per second shutter speed and a 1.5 mega pixel image resolution. High frame rates or high resolution are not required for the prototype's motion speeds and sizes used in the experiments. Figure 6-5 shows an alternative configuration in which a linear slide carrying a low friction carriage is mounted across the top of the tank. The carriage is equipped with a linear encoder and low friction is achieved with the use of vacuum preloaded air bearings. These setups allow for both free swimming experiments and constrained motion experiments. During free swimming experiments a prototype swims freely along the length of the tank and its motions are recorded using the digital camera. For constrained motion experiments, the fish is attached to the low friction carriage which constrains the prototype's trajectory to a straight line. As the prototype swims it pushes the carriage and its swimming displacements and velocities are then measured using the carriage linear encoder. Both types of measurements can then be used to verify the validity of each other. Figure 6-6 displays a side view of the linear slide and carriage assembly. Details on the air bearings configuration, the carriage design, and the encoder location can be seen. A prototype is connected to the carriage through a flexure mechanism that includes a tension compression load cell positioned to measure the forces acting along the axis of the prototype. Figure 6-7 displays different views of the low friction carriage design. A total of four vacuum preloaded air bearings are used, to avoid over-constraints each air bearing is mounted using a flexure connection.

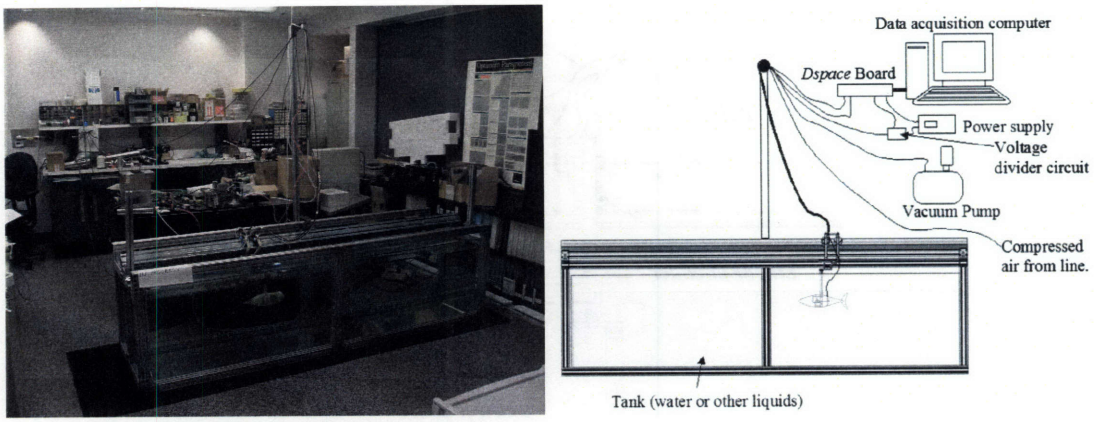

Figure 6-3: Acrylic tank and supporting hardware.

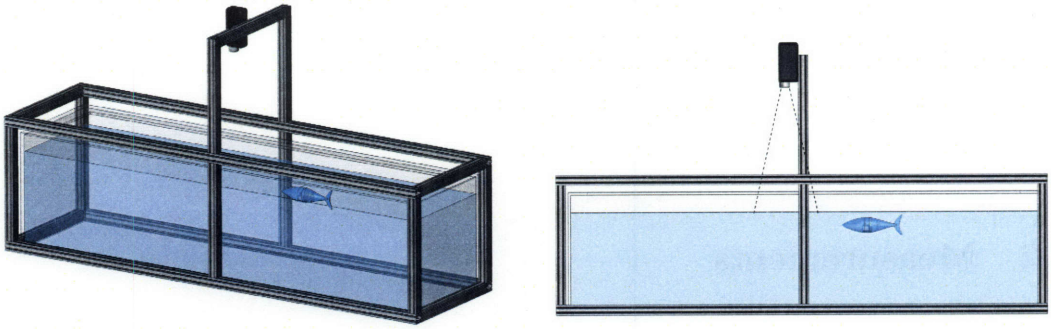

Figure 6-4: Tank with camera setup.

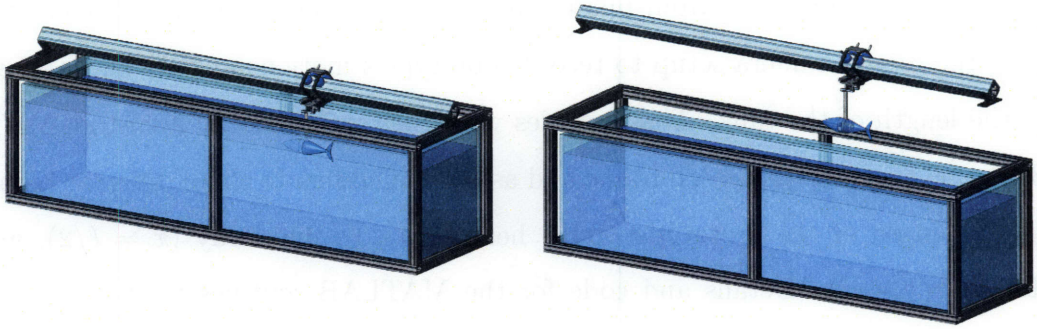

Figure 6-5: Tank with linear slide and low friction carriage setup.

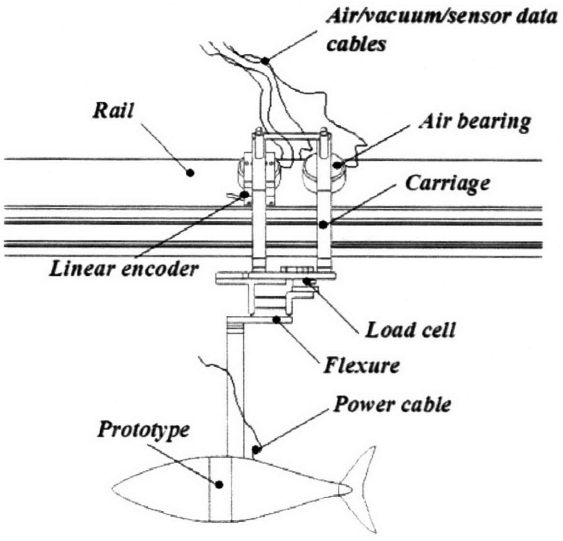

Figure 6-6: Linear slide and carriage assembly features.

6.3.2 Measurements

The analysis in Chapter 3 indicates that estimates of a prototype's swimming kinematics in terms of the amplitude of oscillation at the caudal end $h(\ell)$ and the wave number κ are required in order to estimate its swimming performance. Therefore, measurements of amplitudes h (which we refer to as simply H) and phase ϕ between the caudal end and the nose of a prototype were carried through. The body wave number κ can be computed from phase data as $\kappa = \frac{\phi}{\ell}$. The experiments consisted of using the digital camera setup to record prototype's motions as they swam freely along the length of the tank. These movies were then processed by a custom MATLAB routine that analyzed each frame and assigned markers to three different points along the length of the prototype body: head ($x = 0$), mid-body ($x = \ell/2$), and caudal end ($x = \ell$). Details and code for the MATLAB routines used to analyze experimental results can be found in Appendix C. Figure 6-8 shows both a movie frame (left image) of a prototype swimming and a superposition of multiple MATLAB processed frames (right image) where the contours of the prototype and its power ca-

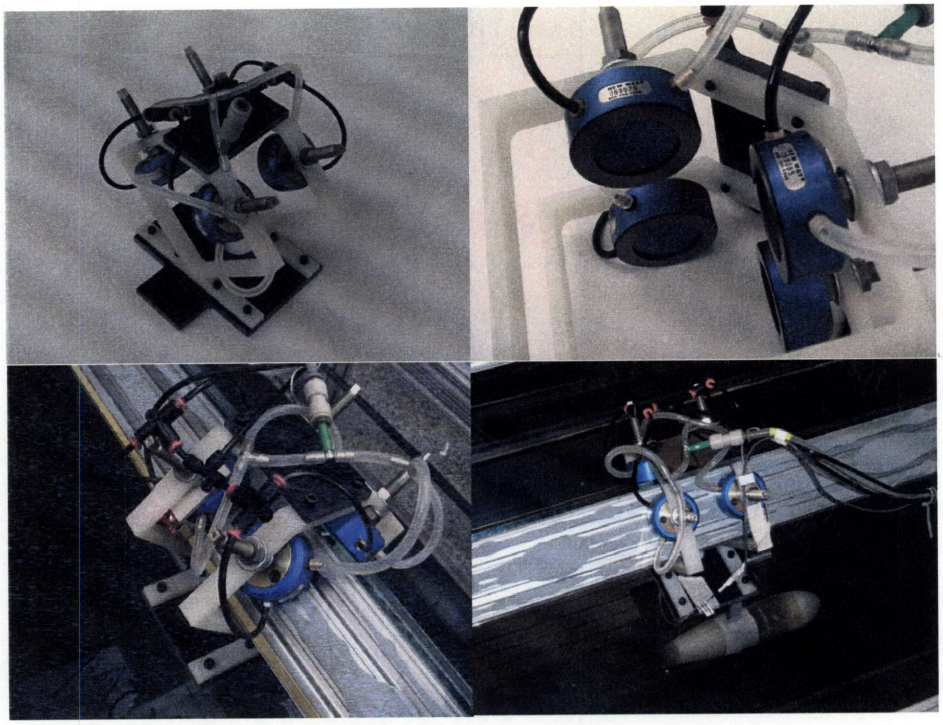

Figure 6-7: Low-friction carriage details.

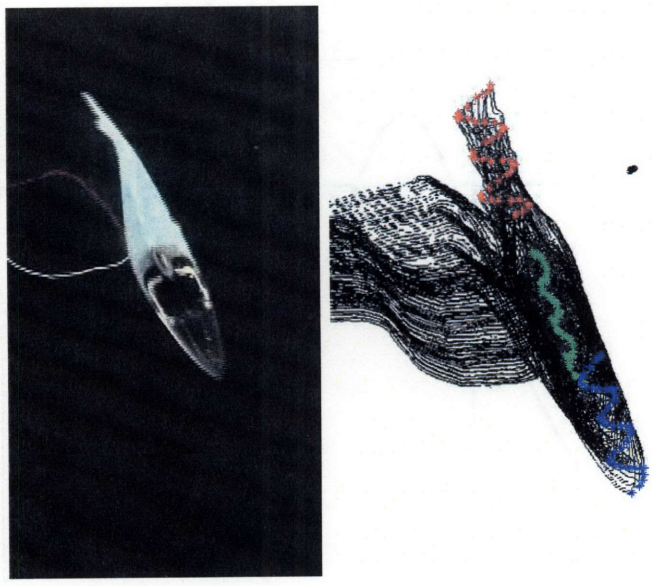

Figure 6-8: Free swimming Hybrid bass movie frame (left image). Superposition of MATLAB processed frames: prototype contours appear in black, body markers for head, mid body, and caudal end appear in blue, green, and red respectively (right image).

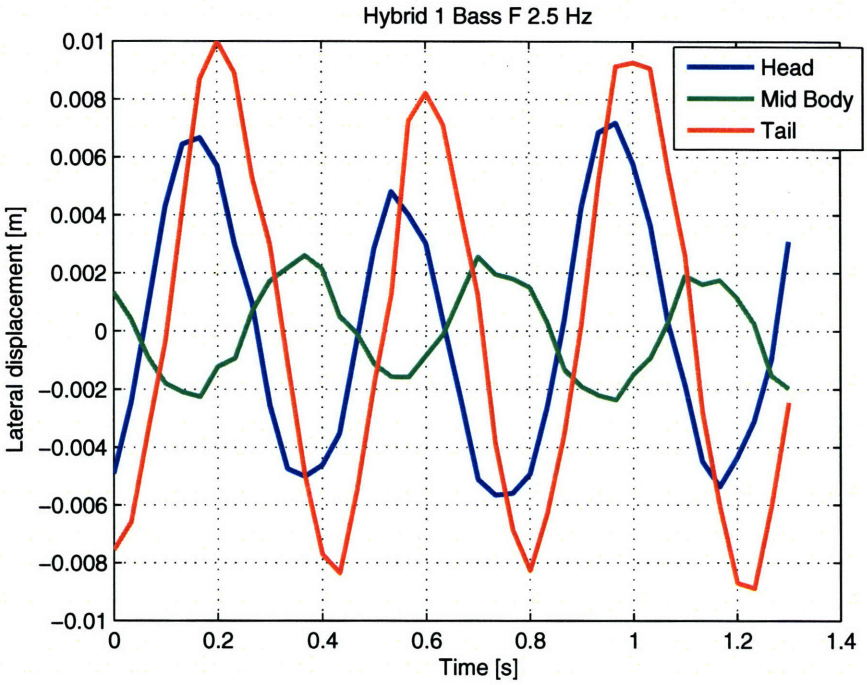

Figure 6-9: Hybrid bass kinematics: Time history of amplitude variations for head (blue), mid body (green), and caudal end (red).

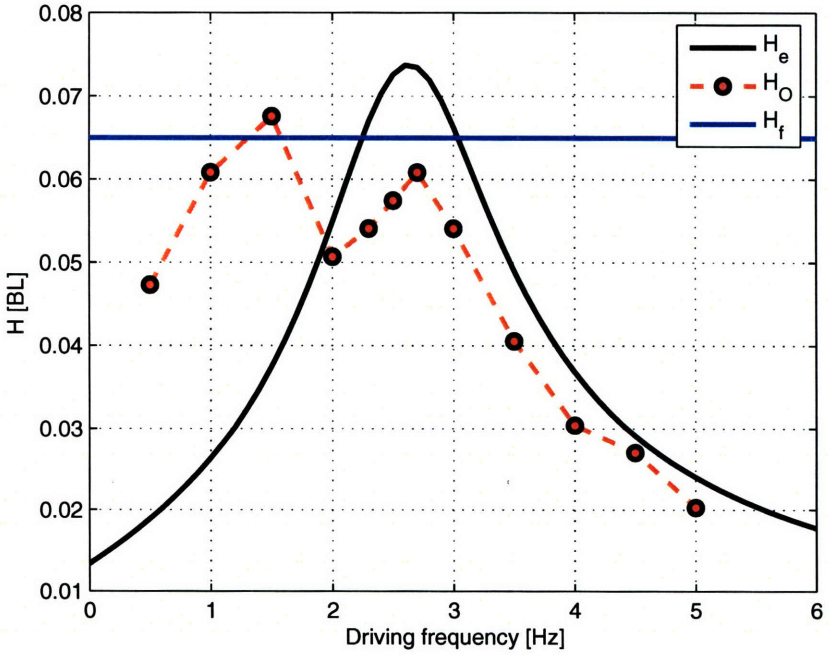

Figure 6-10: Lateral body oscillation amplitudes at caudal end.

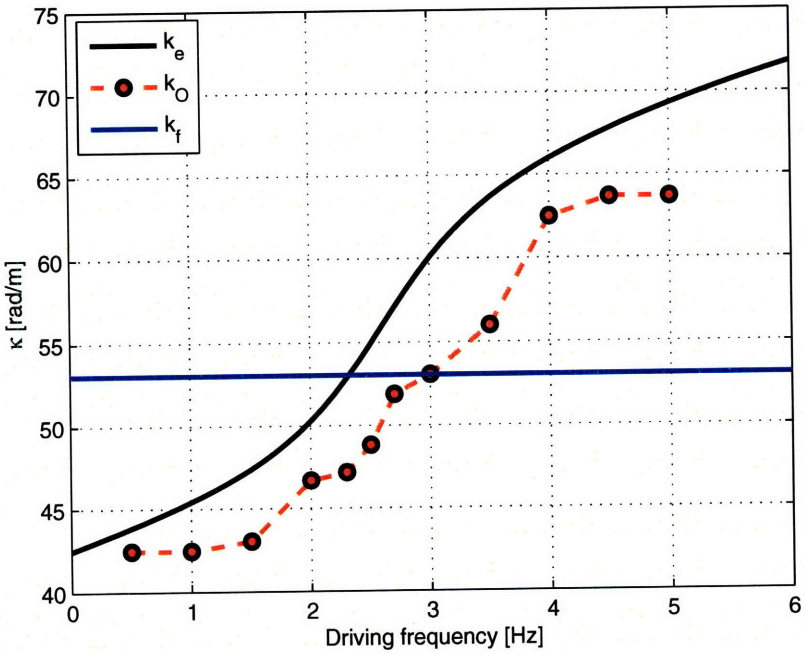

Figure 6-11: Body wave number.

ble appear in black and the body markers for head, mid body, and caudal end appear in blue, green, and red respectively. The superposition of processed frames allows the visualization of body kinematics as the prototype swims forward. The custom MATLAB routine uses the cumulative information on the frames to determine an average direction of motion and calculate the oscillations of each marker with respect to this average direction. The results for a caranguiform prototype, Hybrid Bass 1, swimming with a tail beat frequency of $2.5Hz$ are shown in Figure 6-9. The results in Figure 6-9 can be used to calculate average amplitudes of oscillation as well as the phase difference between the head, mid body and caudal end. The oscillation amplitude of a prototype is computed by averaging the amplitude values over at least 4 tail beat cycles. The phase between the caudal end and the nose of a prototype is found by measuring the time delay Δt between the head oscillations and Tail oscillations,

$$\phi_o = \frac{\Delta t 2\pi}{\tau}$$

where τ is the period of oscillations. The wave number data is then computed from the phase data,

$$\kappa_o = \frac{\phi_o}{\ell}$$

These results can then be compared with the theoretical predictions developed in Chapter 3. Figures 6-10 and 6-11 display the results for amplitudes H_o and wave numbers κ_o (dashed red lines) computed from data similar to the example in Figure 6-9 acquired for swimming frequencies ranging between $0.5Hz$ and $5Hz$. The range of frequencies tested was constrained by the bandwidth of the RC servomotors used in the prototypes. Model predictions for the kinematic parameters H_e, from Equation (3.18), and κ_e, from Equation (3.19),(solid black lines) and the values displayed by real fish H_f and κ_f (solid blue lines), which represent the target kinematics, are also superimposed for comparison. The amplitude data H_o in Figure 6-10 displays a first peak at $1.5Hz$ and a second peak at $2.7Hz$. The occurrence of two peaks is normal in experiments involving small prototypes (Yellow bass, Orange bass, Green bass, Clear bass, White bass, Hybrid bass 1, and Hybrid bass 1). When larger prototypes (Big bass, Tuna, Shark 3, Hybrid tuna) are tested only one peak is observed. A peak in the amplitude data H_o is expected and corresponds to the resonant frequency also displayed by the theoretical prediction H_e. The first peak, present in small prototype's data only, is due to an extra resonant mode introduced by the prototype's power cable. This extra resonant mode is negligible for bigger prototypes because of their larger inertia. The prototypes are designed such that the target kinematics are achieved at the resonant frequency of the tail since at this particular frequency the required input force is minimized. For the prototype whose measurements are shown in Figure 6-10 the design frequency was $2.7Hz$. The data in Figure 6-10 confirms a good qualitative agreement of the model estimations H_e and the measured data H_o. The amplitude estimation error e_H, defined as the error between the measured and estimated amplitudes, at the design frequency is in the order of 20%,

$$e_H = abs(H_e(2.7) - H_o(2.7)) \approx 0.013[l]$$

In addition, the amplitude error $e_H^\star$, defined as the error between the measured and target amplitudes, at the design frequency is in the order of 10%,

$$e_H^\star = abs(H_f(2.7) - H_o(2.7)) \approx 0.0075[l]$$

Figure 6-11 displays the wave number data κ_o. It can be observed that the measured values increase with driving frequency. Again, the experimental behavior κ_o is qualitatively described my the model prediction κ_e. The estimation error in wave number e_κ, defined as the error between the measured and estimated wave number values at the design frequency $f = 2.7hz$ is in the order of 10%,

$$e_\kappa = abs(\kappa_e(2.7) - \kappa_o(2.7)) \approx 6[rad/l]$$

The wave number estimate consistently overestimates the actual wave number measurements. The wave number error $e_\kappa^\star$, defined as the error between the measured and target wave numbers, at the design frequency is in the order of 4%,

$$e_\kappa^\star = abs(\kappa_f(2.7) - \kappa_o(2.7)) \approx 2[rad/l]$$

6.4 Prototype Swimming Performance

6.4.1 Experimental Setup

In order to characterize the prototype's swimming performance, the tank setup is used once more. As discussed in the previous section, a prototypes's swimming velocity can be measured in two different ways. Prototypes can be attached to the low-friction carriage and their swimming velocity is monitored using the carriage linear encoder. Alternatively, prototypes can swim freely inside the tank while their motions are recorder by the digital camera. A second custom MATLAB script was used to determine the body displacement in the average direction of motion for each movie frame, and the camera shutter sampling gives the time reference to calculate average

velocities.

The low-friction carriage setup can also be used to estimate the thrust developed by a prototype. The vacuum pre-loading force on the bearings can be adjusted such that it prevents forward motion. Once the carriage is clamped, the forces achieved by the motions of a prototype's body are transmitted through the flexure support to the load cell and recorded. Alternatively, for smaller prototypes a second fixture was designed in which a similar principle is used to measure static thrust. Figure 6-12 displays the two fixtures side by side. The smaller fixture does not use the linear slide, instead it can be attached to an anchoring structure as shown in Figure 6-13. The thrust values measured with these fixtures are lower bounds of the real swimming thrust since during free swimming the external hydrodynamics change and the thrust is augmented by the vorticity forces shed by the undulating body [25].

To measure a prototype's total propulsive efficiency it is convenient to have an external power supply attached to the prototype via wires. Great care was taken when choosing the appropriate cable lengths and gauges to avoid any significant interference with prototype motions. A simple voltage divider circuit can be used to measure the current i and voltage v drawn by a prototype as it swims. The total propulsive efficiency is measured by combining these measurements with the measurements of swimming velocity and thrust estimates, $\eta = \frac{UT}{vi}$.

Finally, in order to characterize subsystem efficiencies an experimental setup to measure servomotor efficiencies was designed and built. Figure 6-14 displays different views of the setup. The setup consists of an especial prototype tail where the flexure type servo transmission used has a miniature tension compression load cell embedded into one of its links. Figure 6-14 shows a side view of the system (left image), a close up of the transmission link where the load cell is mounted (middle image), and a frontal view that shows both the servo and the load cell (right image). As the tail is actuated by the servo, the force applied to the body can be measured, and using the known servo arm length the moment M applied by the servo can be computed. Simultaneously, the voltage v and current i consumed by the servo can be measured and the local angular velocity $\dot{h}'(a)$ is given by the servo angular velocity which is

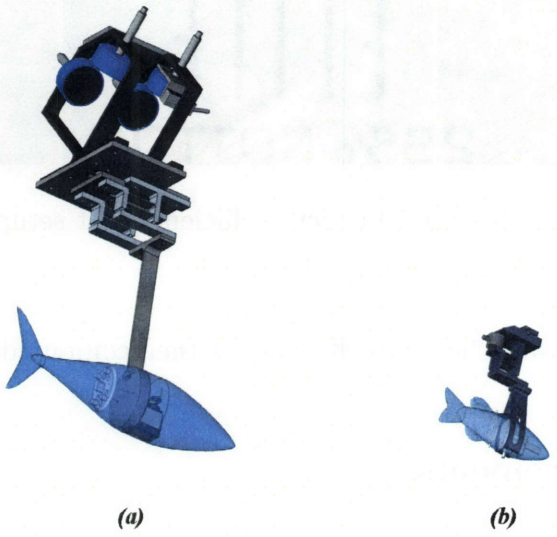

Figure 6-12: Thrust measurement hardware: (a) Low-friction carriage. (b) Fixture for small prototypes.

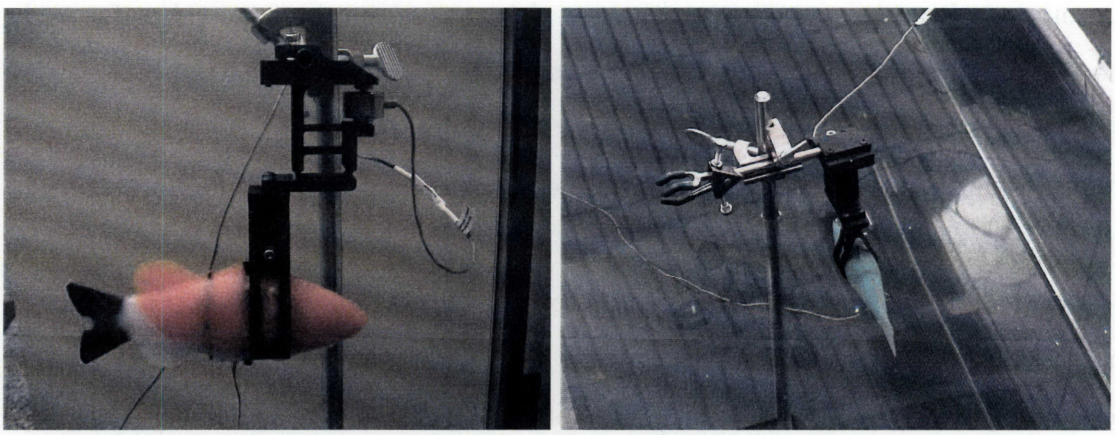

Figure 6-13: Static thrust fixture: Side view showing flexure connection to prototype and tension compression load cell (left image), top view showing anchoring structure and fixture submerged inside tank (right image).

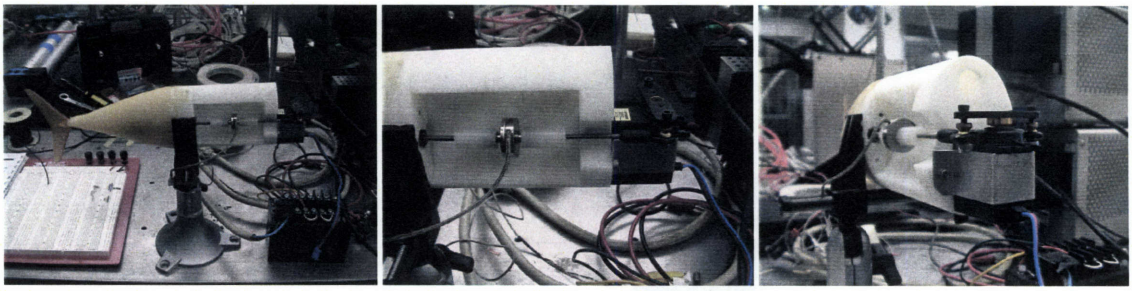

Figure 6-14: Servo efficiency test setup.

controlled and known. The servo efficiency is then computed as $\eta_1 = \frac{M\dot{h}'(a)}{vi}$.

6.4.2 Measurements

The swimming performance is defined by the propulsive thrust T, the swimming velocity U, and the total propulsive efficiency η. Figure 6-15 displays raw experimental measurements of the voltage (blue traces) and current (red traces) consumed, and the corresponding static thrust (green traces) produced by a prototype for various swimming frequencies ranging between $1Hz$ and $5Hz$. Again, the range of frequencies tested was constrained by the bandwidth of the RC servomotors used in the prototypes. In order to compress the raw data, average values are taken for each measurement. Figure 6-16 shows the resultant average values for voltage (blue), current (red), and static thrust (green) versus swimming frequency. As the swimming frequency increases from $0.5Hz$ to $5Hz$ the average current consumed increases almost 4 times from $\sim 0.1A$ to $\sim 0.4A$. The average voltage decreases slightly from $\sim 5.1V$ to $\sim 5.05V$ due to loading of the power supply. The resulting static thrust increases from $\sim 0.015N$ at low frequencies to a maximum value of $\sim 0.025N$ at the design frequency of $2.7Hz$ and then drops off to $\sim 0.01N$ as the swimming frequency reaches $5Hz$. The thrust data exhibits a local minimum at $2.3Hz$ right before the design frequency. This irregularity is due to the experimental setup. At frequencies near $\sim 2.3Hz$ a natural mode of vibration of the water mass inside the tank is excited. Changing the water volume inside the tank can shift the location of the irregularity but for allowable volumes this water mode stays within the range of tested frequencies.

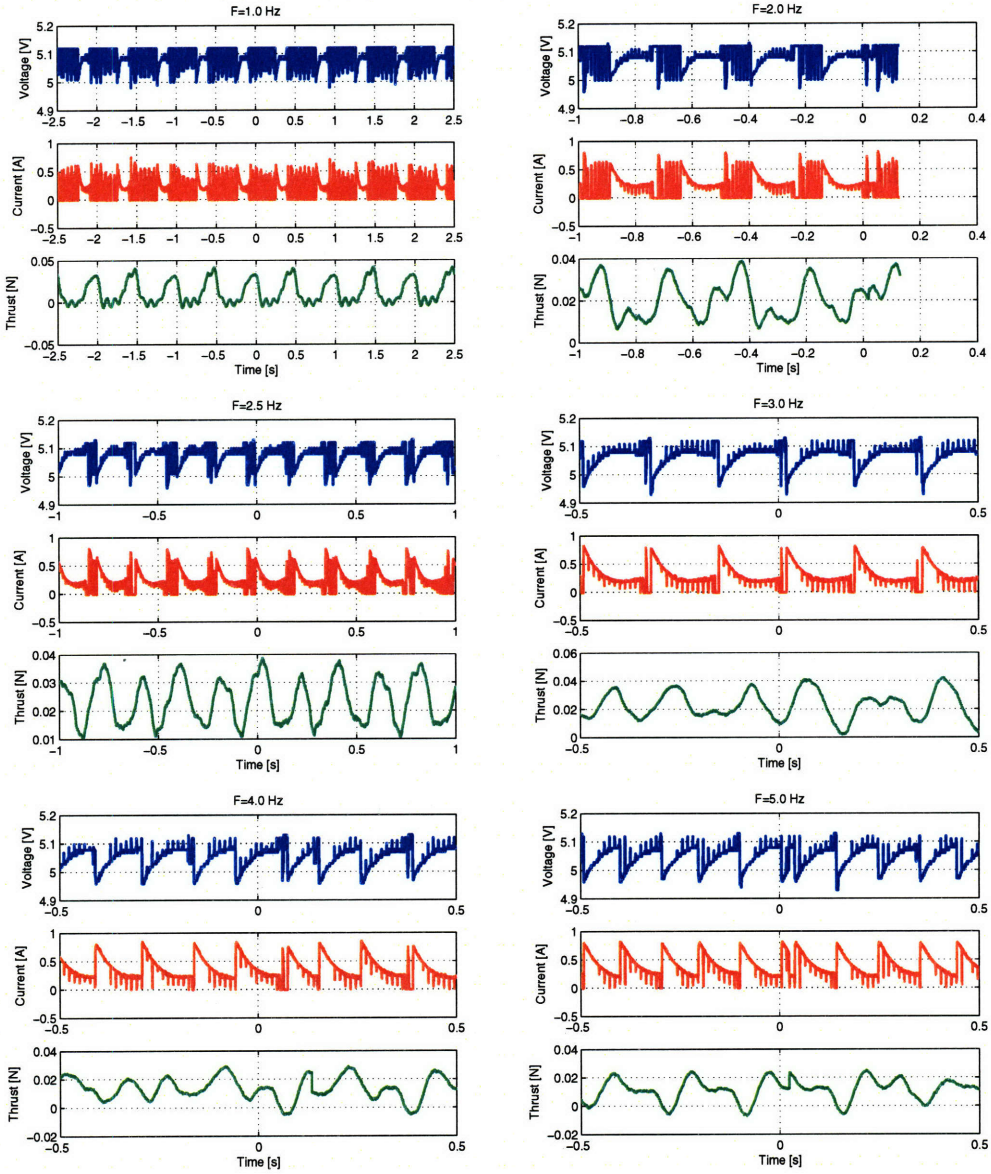

Figure 6-15: Raw experimental measurements of voltage (blue traces), current (red traces), and static thrust (green traces) for a prototype swimming at frequencies between $1Hz$ and $5Hz$.

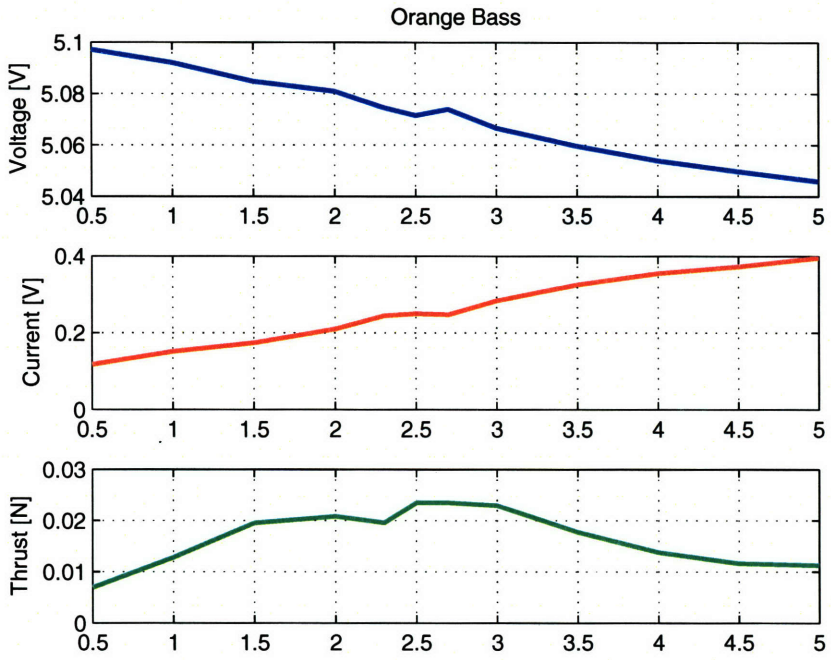

Figure 6-16: Average voltage, current and static thrust values versus swimming frequency.

The increased water motion affects the static thrusts readings negatively by damping the force which the prototype applies to the load cell. Figure 6-17 displays the average thrust measurements T_o for a caranguiform swimmer, Hybrid bass 1, where thrust estimates T_e, computed from Equation (3.21), are also superimposed for comparison. The maximum measured static thrust at the design frequency of $f = 2.7Hz$ is also predicted by the thrust estimate T_e. In addition, the thrust estimate T_e captures qualitatively the static thrust T_o behavior but consistently underestimates its values. The estimation error at the design frequency is,

$$e_T = abs(T_e(2.7) - T_o(2.7)) \approx 0.01[N]$$

Figure 6-18 shows average static thrust data for other caranguiform and thunniform prototypes. All prototypes display similar performance, exhibiting a peak at their corresponding design frequencies. The maximum static thrust measured is in the

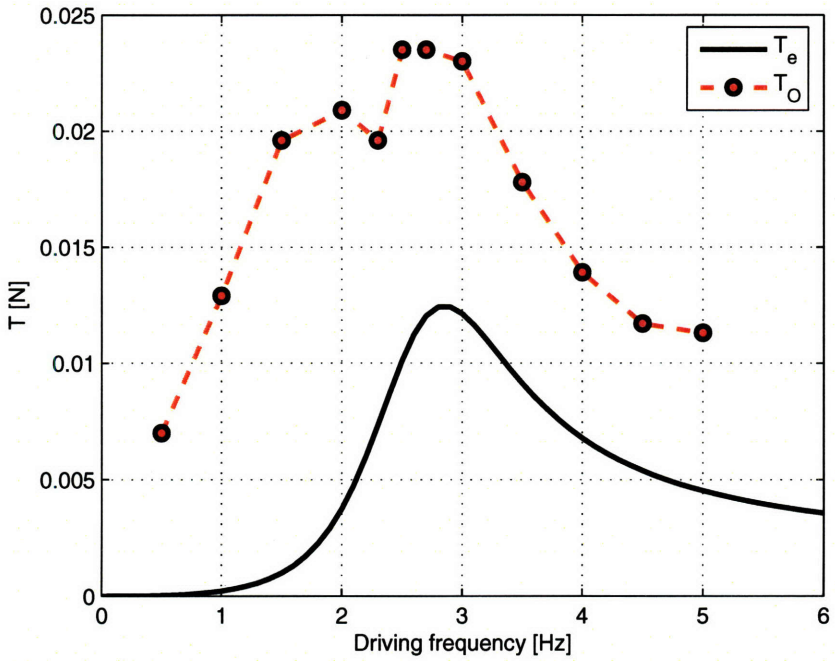

Figure 6-17: Static thrust measurements and thrust estimates versus swimming frequencies.

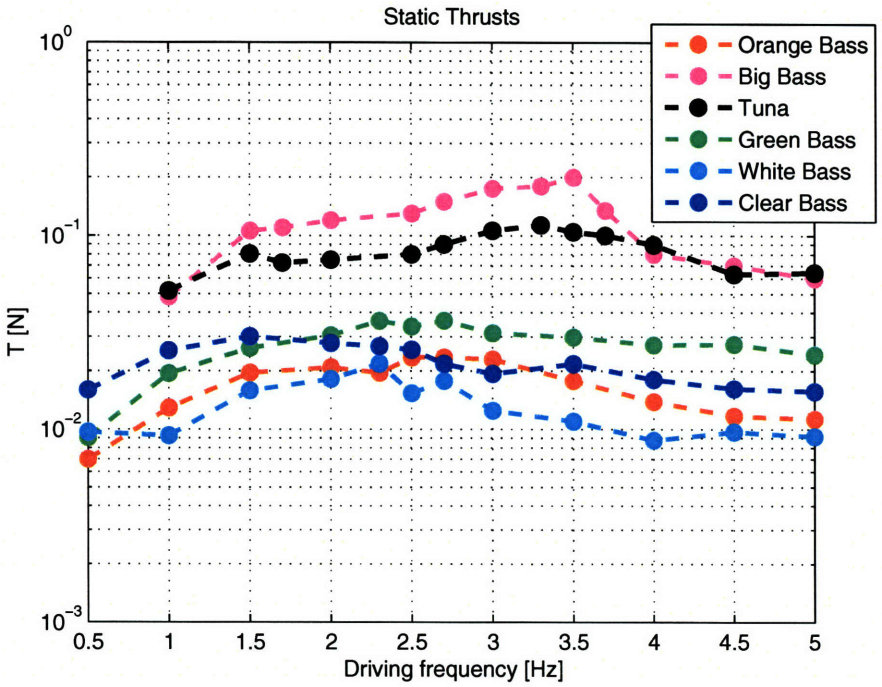

Figure 6-18: Thrust measurements for caranguiform and thunniform prototypes.

order of $0.2N$ and corresponds to a caranguiform swimmer prototype, Big bass, with body length $\ell = 0.3m$ and occurs close to its correspondent design frequency of $3.5Hz$.

Figure 6-19 displays average velocity measurements U_o for a caranguiform swimmer, Hybrid bass 1, computed with the custom MATLAB code described in the previous section. The average velocity estimates U_e, computed from Equation (3.22), and the target fish swimming velocity U_f [6] are superimposed for comparison. The maximum measured velocity occurs at the design frequency $f = 2.7Hz$. The velocity estimates U_e are in good agreement with the experimental results U_o. The estimation error at the design frequency is,

$$e_U = abs(U_e(2.7) - U_o(2.7)) \approx 0.015[l/s]$$

Figure 6-20 displays average velocity data for other caranguiform and thunniform prototypes. Again, all prototypes display similar behavior with a performance peak at the design frequency. The maximum swimming velocity measured is in the order

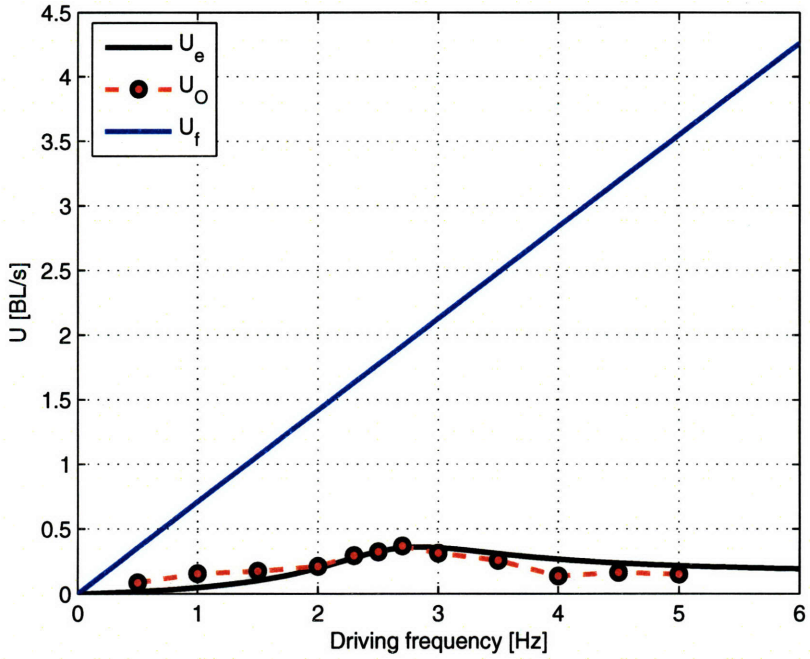

Figure 6-19: Swimming velocity measurements, swimming velocity estimates, and target swimming performance versus swimming frequencies.

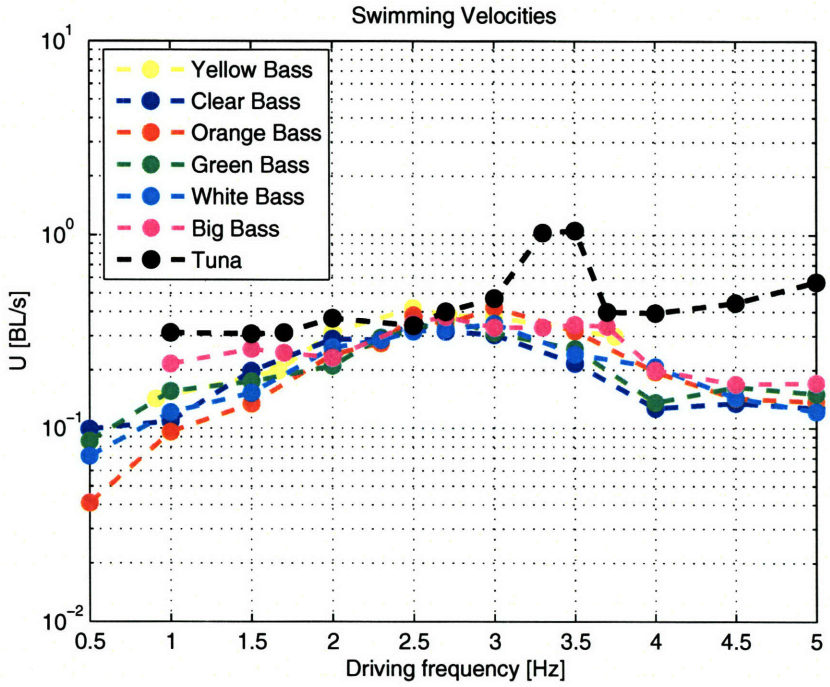

Figure 6-20: Swimming velocity measurements for caranguiform and thunniform prototypes.

of $1\ell/s$ and corresponds to a thunniform swimmer prototype, Tuna, with body length $\ell = 0.3m$ and occurs close to its correspondent design frequency of $3.5Hz$.

Figure 6-21 displays total propulsive efficiency measurements η_o for a caranguiform swimmer, Hybrid bass 1, along with propulsion efficiency estimates η_e computed from Equation (3.26). The maximum measured efficiency occurs at the design frequency $f = 2.7Hz$. The efficiency estimates capture qualitatively the trends perceived in the experimental results. The error at the design frequency is,

$$e_\eta = abs(\eta_e(2.7) - \eta_o(2.7)) \approx 10^{-3}$$

The total propulsive efficiencies are very low, $\eta \sim 0.0012$ (0.12%). The low efficiency is primarily due to the actuation used in the prototypes. Radio controlled servomotors are not designed to be operated with continuous direction changes, the armature inductance heats up quickly and power is lost through heat. Furthermore, the gear

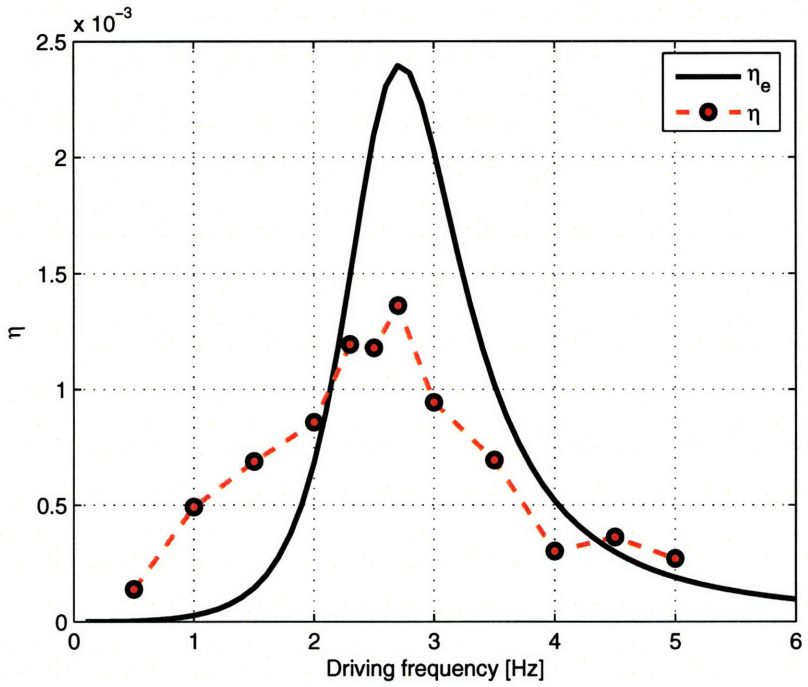

Figure 6-21: Total propulsive efficiency measurements and propulsive efficiency estimates versus swimming frequencies.

boxes and transmissions in RC servomotors use plastic gears and components with little lubrication which also contributes to power losses through friction.

In order to gauge the performance of the different system components described in Chapter 3, the servo performance if first characterized. Figure 6-22 portrays the typical measured efficiency η_1 of the prototype's servomotors versus swimming frequency. As predicted, the efficiency of this type of transducer is very low when used for alternating motions. The servo efficiency has a peak of 0.55% at $2Hz$ and an average value of 0.35% for the tested frequencies. Next, the efficiency of subsystems 2 and 3 can be identified from the total efficiency η and the servo efficiency η_1,

$$\eta_2 \times \eta_3 = \frac{\eta}{\eta_1}$$

Figure 6-23 displays the calculated values for $\eta_2 \times \eta_3$. The results show a maximum of

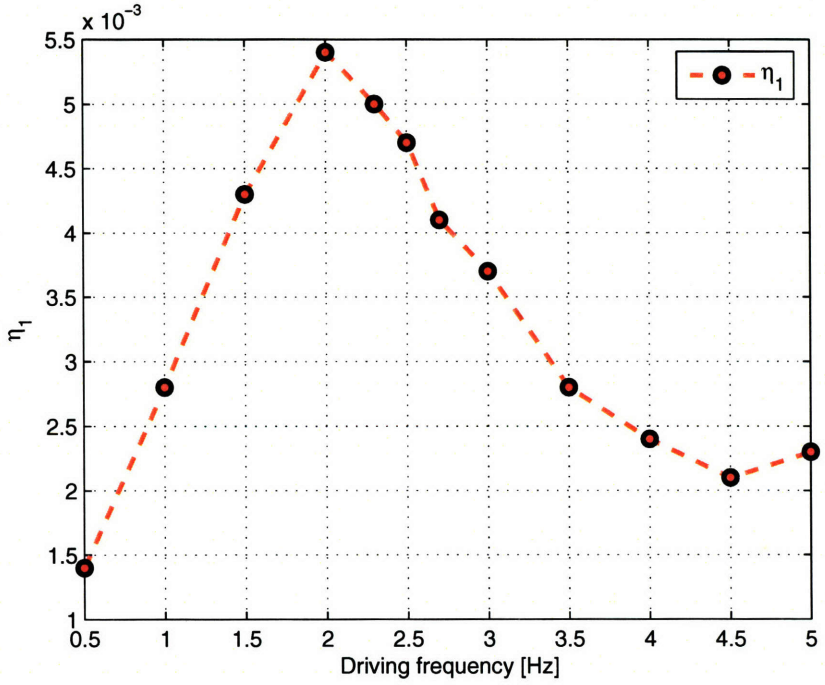

Figure 6-22: Subsystem 1: servomotor efficiency versus swimming frequencies.

$\sim 34\%$ at the design frequency $(2.7Hz)$. Furthermore, the hydrodynamic efficiency (subsystem 3) can be estimated using the model derived in Chapter 3 (Equation (3.25)) evaluated with the kinematic variables H and κ measured in the previous section. The results are shown in Figure 6-24, a local maximum of $\sim 58\%$ occurs at the design frequency $(2.7Hz)$. The average hydrodynamic efficiency is $\sim 0.55(55\%)$. Finally, the body efficiency (subsystem 2) can be identified using the previous results,

$$\eta_2 = \frac{\eta}{\eta_1 \times \eta_3}$$

Figure 6-25 displays the estimate values for the body efficiency η_2. A maximum body efficiency of 57% occurs at $2.7Hz$ and the average body efficiency is $\sim 0.37(37\%)$. These last results are very encouraging since the hydrodynamic efficiency η_3 is an indicator of how well the prototype design mimics real fish swimming motions. Furthermore, body efficiency η_2 is an indicator that can be used by designers for comparison with alternative fish-like mechanical implementations.

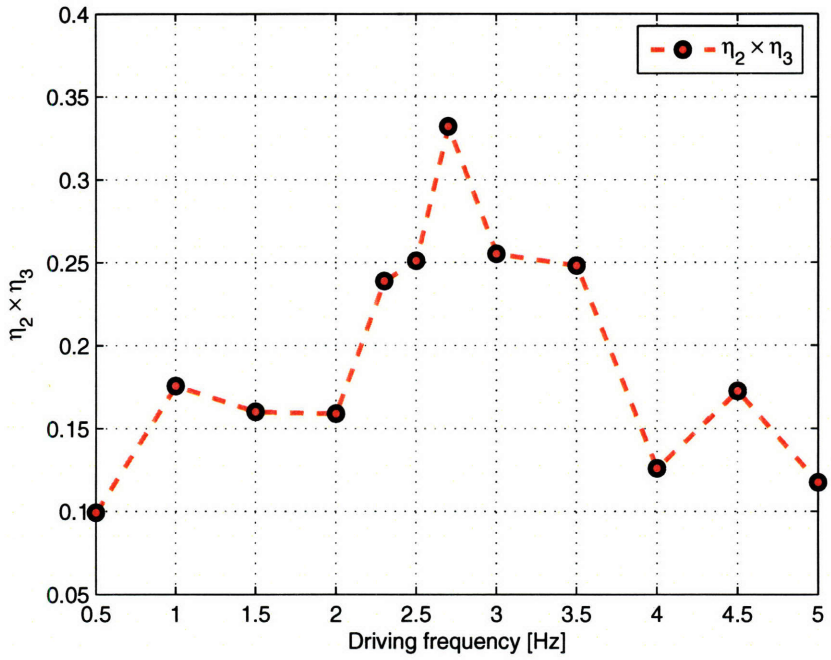

Figure 6-23: Subsystems 2 and 3: Combined body and hydrodynamics efficiency versus swimming frequencies.

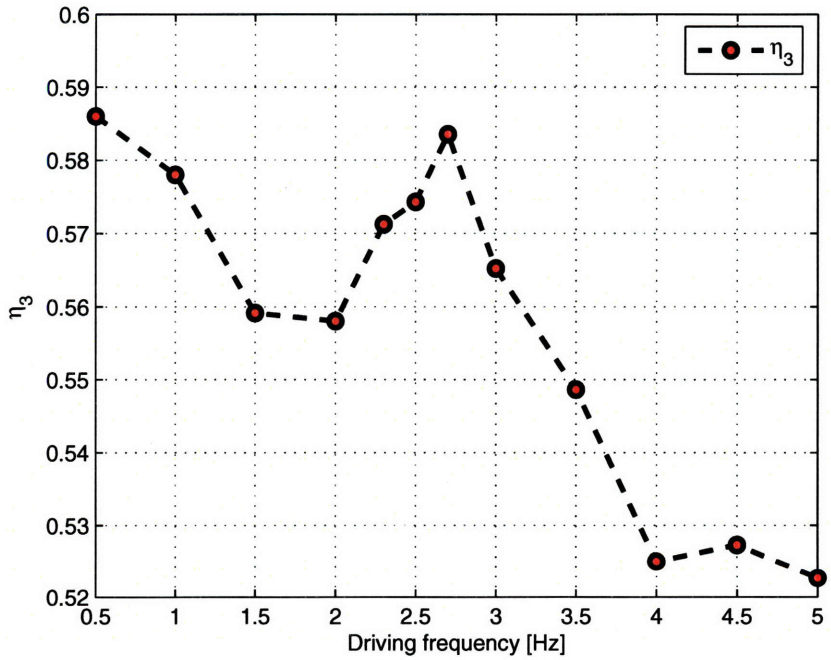

Figure 6-24: Subsystem 3: Hydrodynamic efficiency versus swimming frequencies.

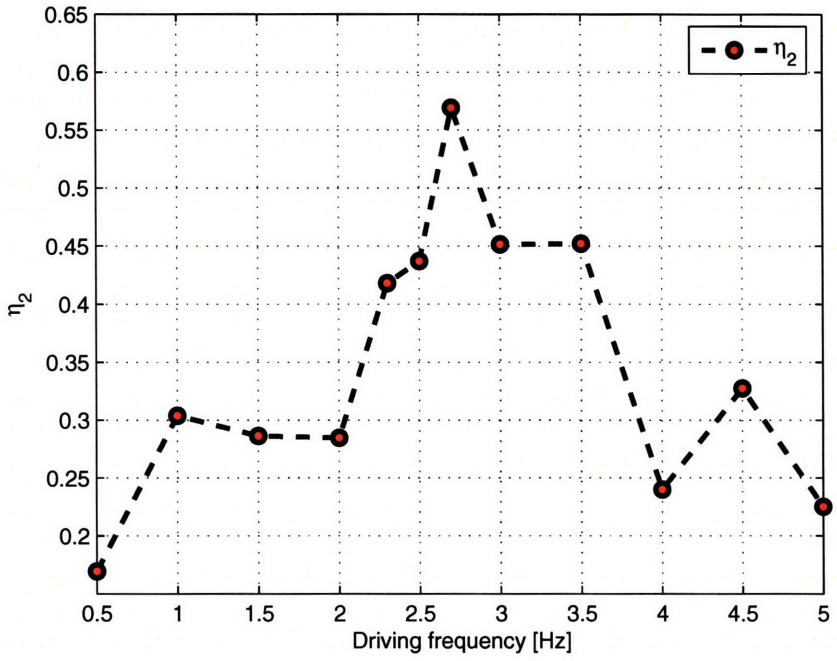

Figure 6-25: Subsystem 2: Body efficiency versus swimming frequencies.

6.4.3 Performance Sensitivity

Swimming performance is a function of design parameter values as the models in Chapter 3 suggest and experimental results in the previous section confirm. Due to the fact that in real hardware implementations, design parameter objectives can not always be met (e.g. unavailable materials, actuators, etc) or can change (e.g. material degradation, failure, etc) it is useful to study and predict the resulting changes in performance. The sensitivity of swimming performance to changes in design variables can be simplified, as suggested in Chapter 3, by using intermediate variables. In this case the intermediate variables are the swimming kinematics variables: amplitude H and phase ϕ. Swimming performance depends on both H and ϕ, and these are in turn functions of the design parameters. Therefore, studying how changes in design parameters influence the swimming kinematics can give some intuition as to how these in turn will change swimming performance. The analysis in Chapter 3 estimates H and ϕ as the amplitude and phase of an equivalent mass-spring-damper system. Both

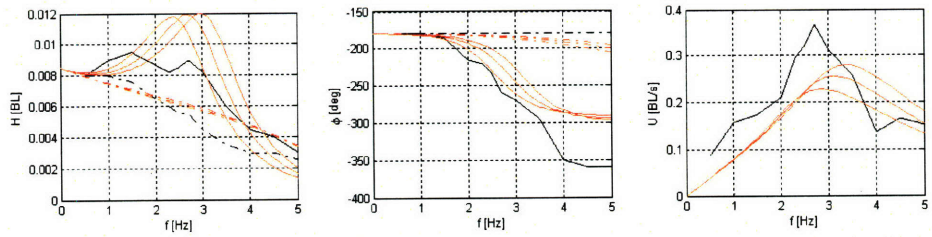

Figure 6-26: Swimming performance sensitivity to changes in modulus E.

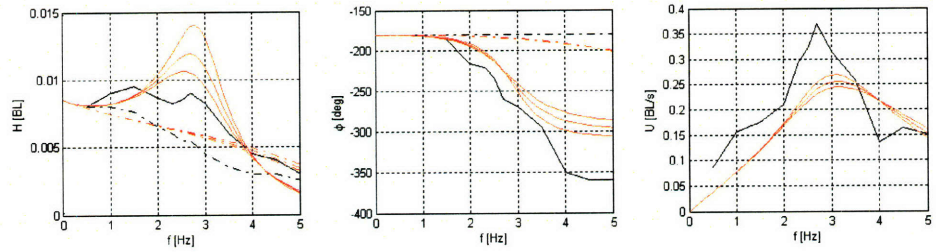

Figure 6-27: Swimming performance sensitivity to changes in viscosity μ.

amplitude and phase behaviors follow this second order system behavior. Figure 6-26 shows amplitude and phase experimental data for a prototype's tail (solid black lines) and head (dashed black lines). The model estimations and their variations due to an increase in modulus value are superimposed in red. Increasing E results in a shift of the resonant peak (increasing stiffness) and a shift in phase. As a result, the peak in swimming velocity increases and shifts accordingly. Figure 6-27 shows once more amplitude and phase experimental data for a prototype's tail (solid black lines) and head (dashed black lines). The model estimations and their variations due to an increase in viscosity value are superimposed in red. Increasing μ results in a decrease of the resonant peak amplitude (adding damping) and accentuates the phase transition. As a result, the peak in swimming velocity decreases.

The importance of these results resides in the fact that the complexity of estimating biomimetic fish-like swimming performance can be simplified to a second order system analysis for which a great majority of engineers have substantial intuition.

Lastly, it should also be noted that prototypes where tested in tap water for pe-

riods spanning several months and in some cases longer than a year without showing material of performance deterioration. For each experiment, prototypes would remain submerged for periods ranging from a couple of hours up to a day. This fact contributes to prove the initial hypothesis regarding the mechanical robustness of continuous compliant bodies.

6.5 Summary

This chapter described the experimental setups used to characterize the performance of prototypes built using the design guidelines in Chapter 4. The experimental data for swimming kinematics and swimming performance was presented and compared to both estimates based on the models developed in Chapter 3 and target performance. Measurements showed good agreement with performance models. The prototype kinematics approached the target fish performance, showing small errors. However, prototype performance is still a fraction of real fish propulsion performance.

Chapter 7

Conclusions and Recommendations

The need for devices capable of locomotion in liquid environments is present in humanitarian, industrial and defence applications. Due to the nature of the mission environments, the required devices must overcome several challenges. The principal challenges are related to hardware performance in terms of propulsion efficiency, mechanical robustness, maneuverability, adaptability, stealth and autonomy. Current traditional approaches that use propeller driven devices have limited success in addressing the principal challenges. As a result biomimetic devices have emerged as a promising alternative that can provide additional features and the promise of improved performance. However, after a review of the field, presented in Chapter 2, the major inherent problems found in current biomimetic devices for underwater locomotion were: (i) mechanical complexity due to the use of discrete and rigid components, and (ii) lack of a structured design approach that would provide guidelines for scaling design parameters according to performance objectives or size constraints. In contrast, the proposed approach presented through the thesis produces prototypes that are mechanically simple, easily scalable, and represent a new type of biomimetic devices based on the principle of exploiting natural dynamics of compliant bodies.

The models that describe the dominant dynamics of the proposed biomimetic compliant swimmers were derived in Chapter 3. The governing equation of lateral body motions $h(x)$ was derived in terms of design parameters: $E, \mu, \rho, A, I, m, \ell, M, \Omega$, and a. Expressions for the lateral body motions $h(x)$ were subsequently found by solving

a special case of the governing equation of motion (i.e. constant coefficients). In addition, swimming kinematics characteristic parameters such as amplitude H and wave number κ were estimated from and order of magnitude analysis of the general equation of lateral body motion. In this manner swimming kinematics parameters were related to design parameters. The corresponding swimming performance in terms of propulsive thrust T, swimming velocity U, and total propulsive efficiency η was in turn related to swimming kinematics parameters using an elongated body theory analysis that incorporated a drag model based on lateral deflection amplitude of the anterior and posterior body ends. Therefore, swimming performance was related to design parameters $E, \mu, \rho, A, I, m, \ell, M, \Omega$, and a through the swimming kinematics parameters H and κ.

Three design methodologies to identify the required design parameters for a given target performance were described in Chapter 4. Based on the analysis carried in Chapter 3, a first step was to simplify calculations by undertaking a change of variables that placed the swimming kinematics as an equivalent performance target instead of the actual propulsion performance. The first approach analyzed the problem of achieving the required performance target $h_{req}(x)$ as a data set fitting problem. The required swimming kinematics $h_{req}(x)$ were seen as a data set that could be fitted with a parametric model defined by the analytical representation of the lateral motions $h(x)$ of a biomimetic device. Model parameters such as bulk material properties E, μ were identified by minimizing the fitting error. A more accurate approach used both the dynamic equation governing the body lateral motions and the required kinematics $h_{req}(x)$ to solve for the appropriate material distributions $E(x)$, $\mu(x)$ and actuation properties $M(x)$ that would satisfy the equations. Finally, based on the theoretical results of the second approach, a lumped parameter approximation was described. In the simplest case, both the posterior and anterior body sections could be modeled as mass-spring-damper systems. This approximation allowed to solve for local bulk material properties E_i, μ_i once actuation properties were defined.

Chapter 5 outlined the manner in which the results obtained by the design methodologies were used to design biomimetic devices that incorporated thunniform and

caranguiform swimming techniques. Details of the designs for these two types of swimmers and the fabrication techniques used for prototyping were presented. Details on the actuators, the actuator transmissions that allow the implementation of concentrated moments, and the control hardware were also presented.

The experimental set ups and techniques used to characterize a prototype's swimming performance were described in Chapter 6. A tank with supporting hardware that included a digital camera setup, a low friction linear slide, and data acquisition equipment, was designed and built for the experiments. Two MATLAB routines were developed to analyze movie frames and calculate average velocities, trajectories, and amplitudes of oscillation of particular points through the body length of a prototype. The procedure to characterize the physical properties of the elastomer materials used in the prototypes was detailed. Experimental measurements of modulus of elasticity E and viscosity μ for silicone and polyurethane gels were also presented. The kinematic models developed in Chapter 3 displayed good agreement with the amplitudes and wave numbers values measured on prototypes. The corresponding swimming performance also displayed good agreement with the models based on elongated body theory. Finally, the limits of swimming performance and the sensitivity to changes in design parameter values were both related to the second order model used to approximate the kinematic variables. Resonant peaks in amplitudes of oscillation were observed at frequencies corresponding to the resonant frequencies of the equivalent second order systems and corresponded to peak in swimming performance. The system's damping increased with an increase in material viscosity and, as expected, corresponded to a decrease in swimming performance. Similarly, the system's resonant frequency shifted with changes in material modulus and resulted in a shift of the swimming performance peak.

7.1 Thesis Contributions

The work on this thesis confirmed the feasibility of achieving fish-like swimming performance with under-actuated compliant bodies. Contributions in three major areas

related to the field of biomimetic devices were accomplished.

First, new analysis tools related to the study of swimming kinematics were developed. Real fish swimming kinematics, which are the target that all fish-like mechanical devices strive to achieve, have been traditionally modeled by functions combining a backward traveling wave with an amplitude envelope. These values can be found experimentally for a particular fish. However, no general scalable expressions existed regarding the features of the amplitude envelope. This thesis provided scalable expressions to define both caranguiform and thunniform swimming amplitude envelopes based on experimental results cited. In addition, swimming performance based on elongated body theory yields good qualitative predictions. However, body kinematics values are required when computing swimming performance. This thesis presented two approaches to estimate body kinematics based on approximate solutions to the equation of body lateral motion: A closed form solution to the constant coefficient case and a solution based on order of magnitude approximation. These analysis tools are useful to the field of biomimetic fish-like mechanism design in general regardless of the mechanical approach used.

In addition, synthesis tools for designing fish-like swimmers using compliant bodies were proposed and tested. The need for complex mechanisms in order to achieve fish swimming kinematics was eliminated and three design methodologies were proposed. The principles behind the design methodologies are very flexible and allow their use with different target kinematics such as maneuvering or other steady or unsteady motions. Furthermore, these ideas can be applied to other biomimetic devices that use undulatory and oscillatory motions, such as anguilliform swimmers, bathoid swimmers, legged and walking robots, brachiating robots (locomotion with arms), etc. Therefore, their usability is not limited and can contribute to improve the design approaches in the robotics field.

Finally, novel designs for thunniform and caranguiform type swimmers that in-

corporate compliant robust biomimetic bodies were detailed. Simple and robust prototypes that can be used in several liquid environments missions where tested and fabrications techniques where successfully put in practice.

7.2 Recommendations for Future Work

The work presented in this thesis enables the study and implementation of alternative steady or unsteady swimming kinematics such as turning, accelerating, etc. Furthermore, different swimming devices such as anguilliform and bathoid swimmers can be designed using the ideas presented in this thesis since the dynamic behavior of these alternative swimming techniques is suitable to similar mechanical implementation as the one presented in this thesis. More generally, the approaches presented here can be implemented in biomimetic locomotion systems that use any king of oscillatory or undulatory movements such as walking, running, etc.

Alternatively, there still a need to study the implementation and compatibility of different sensors typically required for missions in liquid environments. New approaches for inertial navigation, sonar, optical, and chemical detection or clever use of current technologies is required to add the necessary tools to tackle a particular mission.

Finally, the control problems for navigation and task implementation need to be studied. In particular, the mechanical simplicity and dominant dynamics should be exploited when developing new control laws.

Appendix A

Elongated body theory

A.1 Derivations

A.1.1 Assumptions

$$\left|\frac{\partial h}{\partial x}\right| \ll 1, \quad \left|\frac{\partial h}{\partial t}\right| \ll U \tag{A.1}$$

$$\frac{d}{dt} \simeq \frac{\partial}{\partial t} + U\frac{\partial}{\partial x} \equiv D \tag{A.2}$$

A.1.2 Performance

The y-component of the velocity of a cross section seen by the moving water slice is the approximate material derivative of the displacement $h(x,t)$:

$$w(x,t) = \frac{\partial h}{\partial t} + U\frac{\partial h}{\partial x} = Dh \tag{A.3}$$

Let $m(x)$ be the apparent mass of the cross section at x.

$$m(x) \simeq \frac{1}{4}\beta\pi s(x)^2\rho_f \tag{A.4}$$

The lateral force exerted by the body on the water slice is the material derivative of mw.

$$L_y = D(m(x)w(x,t)) = \left(\frac{\partial}{\partial t} + U\frac{\partial}{\partial x}\right)\left[m(x)\left(\frac{\partial h}{\partial t} + U\frac{\partial h}{\partial x}\right)\right] \tag{A.5}$$

The rate of working of the lateral motions is

$$P(t) = \int_0^\ell L_y \frac{\partial h}{\partial t} dx = \int_0^\ell D(mw)\frac{\partial h}{\partial t} dx \tag{A.6}$$

$$\Rightarrow P(t) = \int_0^\ell \left(\frac{\partial}{\partial t} + U\frac{\partial}{\partial x}\right)\left[m(x)\left(\frac{\partial h}{\partial t} + U\frac{\partial h}{\partial x}\right)\right]\frac{\partial h}{\partial t} dx$$

$$\Rightarrow P(t) = \int_0^\ell \left(\frac{\partial}{\partial t} + U\frac{\partial}{\partial x}\right)\left(m(x)w(x,t)\frac{\partial h}{\partial t}\right) dx - \int_0^\ell m(x)w(x,t)\frac{\partial w}{\partial t} dx$$

$$\Rightarrow P(t) = \int_0^\ell m\frac{\partial}{\partial t}\left(w\frac{\partial h}{\partial t}\right) + U\frac{\partial}{\partial x}\left(mw\frac{\partial h}{\partial t}\right) dx - \int_0^\ell m(x)w(x,t)\frac{\partial w}{\partial t} dx$$

$$\Rightarrow P(t) = \int_0^\ell \left(m\frac{\partial}{\partial t}\left(w\frac{\partial h}{\partial t}\right) - mw\frac{\partial w}{\partial t}\right) dx + U\left[mw\frac{\partial h}{\partial t}\right]_{x=\ell} - U\left[mw\frac{\partial h}{\partial t}\right]_{x=0}$$

$$\Rightarrow P(t) = \int_0^\ell \left(m\frac{\partial}{\partial t}\left(w\frac{\partial h}{\partial t}\right) - m\frac{\partial}{\partial t}\left(\frac{1}{2}w^2\right)\right) dx + U\left[mw\frac{\partial h}{\partial t}\right]_{x=\ell}$$

$$P(t) = \frac{\partial}{\partial t}\int_0^\ell \left(mw\frac{\partial h}{\partial t} - \frac{1}{2}mw^2\right) dx + U\left[mw\frac{\partial h}{\partial t}\right]_{x=\ell} \tag{A.7}$$

or alternatively,

$$P(t) = \frac{\partial}{\partial t}\int_0^\ell \left(\frac{1}{2}mw^2 - Umw\frac{\partial h}{\partial x}\right) dx + U\left[mw\frac{\partial h}{\partial t}\right]_{x=\ell} \tag{A.8}$$

If we use another frame of reference where the water far from the fish is at rest:

$$P(t) = UT + U\left[\frac{1}{2}mw^2\right]_{x=\ell} + \frac{\partial}{\partial t}\int_0^l \left(\frac{1}{2}mw^2\right) \tag{A.9}$$

where the first term is the work done by the fish in moving at velocity U in the direction of the thrust T. The second term represents the rate at which kinetic energy of water movements per unit length of fish is shed into the wake at the trailing edge (wasted energy). The third term represents the rate of change of the total kinetic

energy ahead of the trailing edge. Combining Equations (A.8) and (A.9):

$$\frac{\partial}{\partial t}\int_0^{\ell}\left(\frac{1}{2}mw^2 - Umw\frac{\partial h}{\partial x}\right)dx + U\left[mw\frac{\partial h}{\partial t}\right]_{x=\ell} = UT + U\left[\frac{1}{2}mw^2\right]_{x=l} + \frac{\partial}{\partial t}\int_0^{l}\left(\frac{1}{2}mw^2\right)$$

$$\Rightarrow \frac{\partial}{\partial t}\int_0^{\ell}\left(-Umw\frac{\partial h}{\partial x}\right)dx + U\left[mw\frac{\partial h}{\partial t}\right]_{x=\ell} = UT + U\left[\frac{1}{2}mw^2\right]_{x=l}$$

$$T = \left[mw\left(\frac{\partial h}{\partial t} - \frac{1}{2}w\right)\right]_{x=\ell} - \frac{\partial}{\partial t}\int_0^{\ell}\left(mw\frac{\partial h}{\partial x}\right)dx \tag{A.10}$$

Then the average thrust is simply

$$\langle T\rangle = \left\langle\left[mw\left(\frac{\partial h}{\partial t} - \frac{1}{2}w\right)\right]_{x=\ell}\right\rangle \tag{A.11}$$

The efficiency is given by,

$$\eta = \frac{U\langle T\rangle}{\langle P\rangle}$$

From Equation (A.8),

$$\langle P\rangle = \left\langle U\left[mw\frac{\partial h}{\partial t}\right]_{x=\ell}\right\rangle \tag{A.12}$$

thus,

$$\eta = \frac{U\left\langle\left[mw\left(\frac{\partial h}{\partial t} - \frac{1}{2}w\right)\right]_{x=\ell}\right\rangle}{\left\langle U\left[mw\frac{\partial h}{\partial t}\right]_{x=\ell}\right\rangle} = \frac{\left\langle\left[\frac{\partial h}{\partial t}w - \frac{1}{2}w^2\right]_{x=\ell}\right\rangle}{\left\langle\left[w\frac{\partial h}{\partial t}\right]_{x=\ell}\right\rangle} \tag{A.13}$$

The kinematics can be modeled by,

$$h(x,t) = (a_1 + a_2x + a_3x^2)sin(wt - kx) = H(x)sin(wt - kx) \tag{A.14}$$

hence,

$$\frac{\partial h}{\partial t} = \dot{h} = Hwcos(wt - kx)$$

$$\frac{\partial h}{\partial x} = h' = -Hkcos(wt - kx) + H'sin(wt - kx) \tag{A.15}$$

Using Equations (A.3), (A.11) and (A.15),

$$\langle T\rangle = m(\ell)\left\langle\left[w\frac{\partial h}{\partial t}\right]_{x=\ell}\right\rangle - m(l)\left\langle\left[\frac{1}{2}w^2\right]_{x=\ell}\right\rangle$$

$$\Rightarrow \langle T \rangle = m(\ell) \left\langle \left[\dot{h}^2 + U\dot{h}h' \right]_{x=\ell} \right\rangle - m(l) \left\langle \left[\frac{1}{2}(\dot{h}^2 + 2U\dot{h}h' + U^2h'^2) \right]_{x=\ell} \right\rangle$$

$$\Rightarrow \langle T \rangle = m(\ell) \left\langle \left[\frac{1}{2} \left(\dot{h}^2 - U^2h'^2 \right) \right]_{x=\ell} \right\rangle$$

$$\Rightarrow \langle T \rangle = \frac{m(\ell)}{2} \left(\frac{w}{2\pi} \int_0^{\frac{2\pi}{w}} H(\ell)^2 w^2 cos^2(wt - k\ell) dt \right)$$
$$- \frac{m(\ell)}{2} \left(\frac{w}{2\pi} \int_0^{\frac{2\pi}{w}} U^2(-H(\ell)kcos(wt - k\ell) + H'(\ell)sin(wt - k\ell))^2 dt \right) \quad \text{(A.16)}$$

$$\Rightarrow \langle T \rangle = \frac{m(\ell)}{2} \left(\frac{w}{2\pi} \pi w H(\ell)^2 \right) - \frac{m(\ell)}{2} \left(\frac{w}{2\pi} \frac{\pi U^2(k^2 H(\ell)^2 + H'(\ell)^2)}{w} \right)$$

$$\Rightarrow \langle T \rangle = \frac{m(\ell)}{4} \left(w^2 H(\ell)^2 - U^2 k^2 H(\ell)^2 - U^2 H'(\ell)^2 \right)$$

In addition, $V = f\lambda = w/k$ thus $k = w/V$,

$$\Rightarrow \langle T \rangle = \frac{m(\ell)}{4} \left(w^2 H(\ell)^2 - U^2 \frac{w^2}{V^2} H(\ell)^2 - U^2 H'(\ell)^2 \right)$$

$$\langle T \rangle = \frac{m(\ell)}{4} \left(w^2 H(\ell)^2 \left(1 - \frac{U^2}{V^2} \right) - U^2 H'(\ell)^2 \right) \quad \text{(A.17)}$$

To calculate swimming velocities we note,

$$T - D = m_{fish}\dot{U}$$

But at steady state,

$$T = D = \frac{1}{2}\rho_f C_d A U^2 \quad \text{(A.18)}$$

Combining Equations (A.17) and (A.18),

$$\frac{m(\ell)}{4} \left(w^2 H(\ell)^2 \left(1 - \frac{U^2}{V^2} \right) - U^2 H'(\ell)^2 \right) = \frac{1}{2}\rho_f C_d A U^2$$

$$\Rightarrow U^2 \left(\frac{1}{2}\rho_f C_d A + \frac{m(\ell)}{4} \left(\frac{w^2 H(\ell)^2}{V^2} + H'(\ell)^2 \right) \right) = \frac{m(\ell)}{4} w^2 H(\ell)^2$$

$$U = \sqrt{\frac{\frac{m(\ell)}{4} w^2 H(\ell)^2}{\left(\frac{1}{2}\rho_f C_d A + \frac{m(\ell)}{4}\left(\frac{w^2 H(\ell)^2}{V^2} + H'(\ell)^2\right)\right)}} \tag{A.19}$$

Appendix B

Beam theory

B.1 Viscoelastic Timoshenko beam theory (VTBT)

Balance of forces in the y-direction:

$$S - \left(S + \frac{\partial S}{\partial x}dx\right) - L_y dx - D dx = \rho A dx \frac{\partial^2 h}{\partial t^2}$$

$$\Rightarrow -\frac{\partial S}{\partial x} - L_y = \rho A \frac{\partial^2 h}{\partial t^2} \tag{B.1}$$

$$M_b - \left(M_b + \frac{\partial M_b}{\partial x}dx\right) + \frac{1}{2}S dx + \frac{1}{2}\left(S + \frac{\partial S}{\partial x}dx\right)dx = J\frac{\partial^2 \psi}{\partial t^2}$$

$$\Rightarrow -\frac{\partial M_b}{\partial x}dx + S dx = J\frac{\partial^2 \psi}{\partial t^2} \tag{B.2}$$

where,

$$J = \rho I dx \tag{B.3}$$

$$\frac{\partial h}{\partial x} = \psi + \gamma_0 \tag{B.4}$$

$$S = AG\kappa_s\left(\frac{\partial h}{\partial x} - \psi\right) \tag{B.5}$$

$$M_b = -M + M_e + M_v = -M + EI\frac{\partial \psi}{\partial x} + \mu I \frac{\partial}{\partial t}\frac{\partial \psi}{\partial x} \tag{B.6}$$

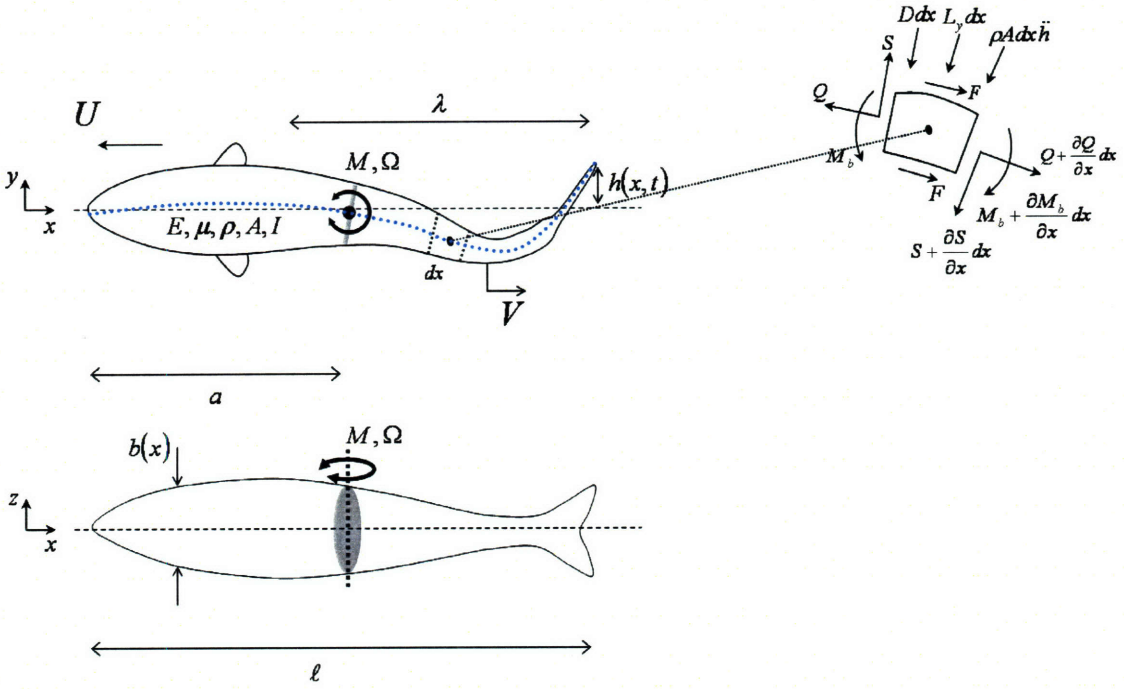

Figure B-1: Fish-like compliant body model parameters.

Substituting Equations (B.5) and (B.6) into Equations (B.1) and (B.2) we find:

$$-AG\kappa_s\left(\frac{\partial^2 h}{\partial x^2}-\frac{\partial \psi}{\partial x}\right)-L_y=\rho A\frac{\partial^2 h}{\partial t^2} \tag{B.7}$$

$$-\frac{\partial}{\partial x}\left(-M+EI\frac{\partial \psi}{\partial x}+\mu I\frac{\partial}{\partial t}\frac{\partial \psi}{\partial x}\right)+AG\kappa_s\left(\frac{\partial h}{\partial x}-\psi\right)=\rho I\frac{\partial^2 \psi}{\partial t^2} \tag{B.8}$$

Differentiating Equation (B.8) with respect to x we get:

$$-\frac{\partial^2}{\partial x^2}\left(-M+EI\frac{\partial \psi}{\partial x}+\mu I\frac{\partial}{\partial t}\frac{\partial \psi}{\partial x}\right)+AG\kappa_s\left(\frac{\partial^2 h}{\partial x^2}-\frac{\partial \psi}{\partial x}\right)=\rho I\frac{\partial^3 \psi}{\partial x \partial t^2} \tag{B.9}$$

From Equation (B.7):

$$\frac{\partial \psi}{\partial x}=\frac{L_y+\rho A\frac{\partial^2 h}{\partial t^2}}{AG\kappa_s}+\frac{\partial^2 h}{\partial x^2} \tag{B.10}$$

Hence, replacing Equation (B.10) into Equation (B.9), we get:

$$-\frac{\partial^2}{\partial x^2}\left(-M+EI\left(\frac{L_y+\rho A\frac{\partial^2 h}{\partial t^2}}{AG\kappa_s}+\frac{\partial^2 h}{\partial x^2}\right)+\mu I\frac{\partial}{\partial t}\left(\frac{L_y+\rho A\frac{\partial^2 h}{\partial t^2}}{AG\kappa_s}+\frac{\partial^2 h}{\partial x^2}\right)\right)$$
$$+AG\kappa_s\left(\frac{\partial^2 h}{\partial x^2}-\left(\frac{L_y+\rho A\frac{\partial^2 h}{\partial t^2}}{AG\kappa_s}+\frac{\partial^2 h}{\partial x^2}\right)\right)=\rho I\frac{\partial^2}{\partial t^2}\left(\frac{L_y+\rho A\frac{\partial^2 h}{\partial t^2}}{AG\kappa_s}+\frac{\partial^2 h}{\partial x^2}\right) \quad \text{(B.11)}$$

$$\frac{\partial^2 M}{\partial x^2}-\frac{\partial^2}{\partial x^2}\left(\frac{EIL_y}{AG\kappa_s}\right)-\frac{\partial^2}{\partial x^2}\left(\frac{EI\rho}{G\kappa_s}\frac{\partial^2 h}{\partial t^2}\right)-\frac{\partial^2}{\partial x^2}\left(EI\frac{\partial^2 h}{\partial x^2}\right)$$
$$-\frac{\partial^2}{\partial x^2}\left(\mu I\frac{\partial}{\partial t}\left(\frac{L_y}{AG\kappa_s}\right)\right)-\frac{\partial^2}{\partial x^2}\left(\mu I\frac{\partial}{\partial t}\left(\frac{\rho}{G\kappa_s}\frac{\partial^2 h}{\partial t^2}\right)\right)-\frac{\partial^2}{\partial x^2}\left(\mu I\frac{\partial^3 h}{\partial t\partial x^2}\right)$$
$$-L_y-\rho A\frac{\partial^2 h}{\partial t^2}=\rho I\frac{\partial^2}{\partial t^2}\left(\frac{L_y}{AG\kappa_s}\right)+\rho I\frac{\partial^2}{\partial t^2}\left(\frac{\rho}{G\kappa_s}\frac{\partial^2 h}{\partial t^2}\right)+\rho I\frac{\partial^4 h}{\partial t^2\partial x^2} \quad \text{(B.12)}$$

B.2 Green function solutions

Assume a solution of the form $w = H(x)e^{i\Omega t}$ where $h = Re\{w\}$, substituting into Equation (3.15) and using a generalized input force $f(x)$:

$$EIH''''e^{i\Omega t}+i\mu I\Omega H''''e^{i\Omega t}-(m(x)+\rho A)\Omega^2 He^{i\Omega t}=f(x)e^{i\Omega t} \quad \text{(B.13)}$$

Dividing by $e^{i\Omega t}$ yields:

$$H''''-\kappa^4 H=\frac{f(x)}{(EI+i\mu I\Omega)} \quad \text{(B.14)}$$

where

$$\kappa^4=\frac{(m(x)+\rho A)\Omega^2}{(EI+i\mu I\Omega)} \quad \text{(B.15)}$$

The solution of Equation (B.14) is given by:

$$H(x)=\int_0^\ell f(\xi)G(x,\xi)d\xi \quad \text{(B.16)}$$

The Green function $G(x,\xi)$ of the beam is its response to a unit concentrated force acting at an arbitrary position ξ. In order to find the Green function we must solve:

$$H'''' - \kappa^4 H = \frac{\delta'(x-\xi)}{(EI + i\mu I\Omega)} \tag{B.17}$$

The solution of Equation (B.17) will be the green function $H = G$ which we can use later in Equation (B.16) to find H for the general problem. Taking the Laplace transform of Equation (B.17) we find:

$$\hat{H}(s) = \frac{1}{(s^4 - \kappa^4)}\left[\frac{e^{-s\xi}}{(EI + i\mu I\Omega)} + s^3 H(0) + s^2 H'(0) + sH''(0) + H'''(0)\right] \tag{B.18}$$

The inverse Laplace transform of Equation (B.18) is:

$$H(x,\xi) = \frac{\phi_4(x-\xi)u(x-\xi)}{\kappa^3(EI + i\mu I\Omega)} + H(0)\phi_1(x) + \frac{H'(0)}{\kappa}\phi_2(x) + \frac{H''(0)}{\kappa^2}\phi_3(x) + \frac{H'''(0)}{\kappa^3}\phi_4(x) \tag{B.19}$$

where $u(x)$ is the unit step function and,

$$\begin{aligned} \phi_1(x) &= \frac{1}{2}(cosh(\kappa x) + cos(\kappa x)), \qquad \phi_2(x) = \frac{1}{2}(sinh(\kappa x) + sin(\kappa x)) \\ \phi_3(x) &= \frac{1}{2}(cosh(\kappa x) - cos(\kappa x)), \qquad \phi_4(x) = \frac{1}{2}(sinh(\kappa x) - sin(\kappa x)) \end{aligned} \tag{B.20}$$

Hence Equation (B.19) is the Green function sought. In order to find the response for a particular problem we will sue the following relations:

$$\begin{aligned} \phi_1' &= \kappa\phi_4 \quad \phi_1'' = \kappa^2\phi_3 \quad \phi_1''' = \kappa^3\phi_2 \\ \phi_2' &= \kappa\phi_1 \quad \phi_2'' = \kappa^2\phi_4 \quad \phi_2''' = \kappa^3\phi_3 \\ \phi_3' &= \kappa\phi_2 \quad \phi_3'' = \kappa^2\phi_1 \quad \phi_3''' = \kappa^3\phi_4 \\ \phi_4' &= \kappa\phi_3 \quad \phi_4'' = \kappa^2\phi_2 \quad \phi_4''' = \kappa^3\phi_1 \end{aligned} \tag{B.21}$$

and for $x \geq \xi$

$$H'(x,\xi) = \frac{\phi_3(x-\xi)}{\kappa^2(EI+i\mu I\Omega)} + \kappa H(0)\phi_4(x) + H'(0)\phi_1(x) + \frac{H''(0)}{\kappa}\phi_2(x) + \frac{H'''(0)}{\kappa^2}\phi_3(x) \tag{B.22}$$

$$H''(x,\xi) = \frac{\phi_2(x-\xi)}{\kappa(EI+i\mu I\Omega)} + \kappa^2 H(0)\phi_3(x) + \kappa H'(0)\phi_4(x) + H''(0)\phi_1(x) + \frac{H'''(0)}{\kappa}\phi_2(x) \tag{B.23}$$

$$H'''(x,\xi) = \frac{\phi_1(x-\xi)}{(EI+i\mu I\Omega)} + \kappa^3 H(0)\phi_2(x) + \kappa^2 H'(0)\phi_3(x) + \kappa H''(0)\phi_4(x) + H'''(0)\phi_1(x) \tag{B.24}$$

To find the beam response we need to solve for $H(0)$, $H'(0)$, $H''(0)$, $H'''(0)$, substitute the values in Equation (B.19) and then solve Equation (B.16) for the appropriate input force. The first step requires the definition of the boundary conditions. We can explore 4 types of boundary conditions that could model our setups.

(a) Assume front end of fish does not move, BCs: Fixed-Free (anguilliform).

(b) Assume front part of body has more mass, BCs: Free-Free, with concentrated mass m_b in the frontal part of the body (anguilliform).

(c) Assume front end of fish does not move, BCs: Fixed-End force due to caudal fin (caranguiform/tuniform).

(d) Assume front part of body has more mass, BCs: Free-End force due to caudal fin, with concentrated mass m_b in the frontal part of the body (caranguiform/tuniform).

Fixed-Free:

$$\begin{aligned} [h]_{x=0} &= 0 \qquad \left[\frac{\partial h}{\partial x}\right]_{x=0} = 0 \\ \left[EI\frac{\partial^2 h}{\partial x^2}\right]_{x=\ell} &= 0 \qquad \left[EI\frac{\partial^3 h}{\partial x 3}\right]_{x=\ell} = 0 \end{aligned} \tag{B.25}$$

From BCs we know that $H(0) = H'(0) = H''(\ell) = H'''(0) = 0$. From Equations (B.23) and (B.24) evaluated at ℓ we find:

$$H''(\ell,\xi) = \frac{\phi_2(\ell-\xi)}{\kappa(EI+i\mu I\Omega)} + H''(0)\phi_1(\ell) + \frac{H'''(0)}{\kappa}\phi_2(\ell) = 0 \tag{B.26}$$

$$H'''(\ell,\xi) = \frac{\phi_1(\ell-\xi)}{(EI+i\mu I\Omega)} + \kappa H''(0)\phi_4(\ell) + H'''(0)\phi_1(\ell) = 0 \tag{B.27}$$

Which are two equations with two unknowns, of the form:

$$\begin{bmatrix} a & b \\ c & d \end{bmatrix} \begin{matrix} H''(0) \\ H'''(0) \end{matrix} = \begin{bmatrix} e \\ f \end{bmatrix}$$

Hence,

$$H''(0) = \frac{fb-ed}{cb-ad} = \frac{-\frac{\phi_1(\ell-\xi)}{(EI+i\mu I\Omega)}\frac{\phi_2(\ell)}{\kappa} + \frac{\phi_2(\ell-\xi)}{\kappa(EI+i\mu I\Omega)}\phi_1(\ell)}{\kappa\phi_4(\ell)\frac{\phi_2(\ell)}{\kappa} - \phi_1^2(\ell)}$$

$$H'''(0) = \frac{ec-fa}{cb-ad} = \frac{-\frac{\phi_2(\ell-\xi)}{\kappa(EI+i\mu I\Omega)}\kappa\phi_4(\ell) + \frac{\phi_1(\ell-\xi)}{(EI+i\mu I\Omega)}\phi_1(\ell)}{\kappa\phi_4(\ell)\frac{\phi_2(\ell)}{\kappa} - \phi_1^2(\ell)}$$

thus,

$$H''(0) = \frac{1}{\kappa(EI+i\mu I\Omega)}\frac{\phi_2(\ell-\xi)\phi_1(\ell) - \phi_1(\ell-\xi)\phi_2(\ell)}{\phi_4(\ell)\phi_2(\ell) - \phi_1^2(\ell)} \tag{B.28}$$

$$H'''(0) = \frac{1}{(EI+i\mu I\Omega)}\frac{\phi_1(\ell-\xi)\phi_1(\ell) - \phi_2(\ell-\xi)\phi_4(\ell)}{\phi_4(\ell)\phi_2(\ell) - \phi_1^2(\ell)} \tag{B.29}$$

and from Equation (B.19)

$$G(x,\xi) = \frac{1}{\kappa^3(EI+i\mu I\Omega)}\left[\phi_4(x-\xi)u(x-\xi) + C_1\phi_3(x) + C_2\phi_4(x)\right] \tag{B.30}$$

where

$$C_1 = \frac{\phi_2(\ell-\xi)\phi_1(\ell) - \phi_1(\ell-\xi)\phi_2(\ell)}{\phi_4(\ell)\phi_2(\ell) - \phi_1^2(\ell)}$$

$$C_2 = \frac{\phi_1(\ell-\xi)\phi_1(\ell) - \phi_2(\ell-\xi)\phi_4(\ell)}{\phi_4(\ell)\phi_2(\ell) - \phi_1^2(\ell)}$$

From Equation (B.16),

$$H(x) = \int_0^\ell f(\xi)G(x,\xi)d\xi = \int_0^\ell \delta'(\xi-a)M_0G(x,\xi)d\xi$$

Making use of the relation:

$$\int_a^c \delta^{(n)}(\xi-b)f(\xi)d\xi = (-1)^n f^{(n)}(b) \quad a \le b \le c \tag{B.31}$$

$$\Rightarrow H(x) = \int_0^\ell \delta'(\xi - a) M_0 G(x,\xi) d\xi = -M_0 \frac{\partial G}{\partial \xi}(a)$$

Hence,

$$H(x) = \frac{-M_0}{\kappa^3(EI + i\mu I\Omega)} \left[\frac{\partial \phi_4(x-\xi)}{\partial \xi} u(x-\xi) + \phi_4(x-\xi) \frac{\partial u(x-\xi)}{\partial \xi} + \frac{\partial C_1}{\partial \xi}\phi_3(x) + \frac{\partial C_2}{\partial \xi}\phi_4(x) \right]$$

Note that:

$$\frac{\partial \phi_i(z)}{\partial \xi} = \phi_i' \frac{\partial(z)}{\partial \xi}$$

So using relations in Equation (B.31) we find:

$$\frac{\partial G}{\partial \xi} = \frac{1}{\kappa^3(EI + i\mu I\Omega)} \left[\kappa\phi_3(x-\xi)(-1)u(x-\xi) + \phi_4(x-\xi)\delta(x-\xi)(-1) + Q_1\phi_3(x) + Q_2\phi_4(x) \right] \tag{B.32}$$

where,

$$Q_1 = \frac{\kappa\phi_1(\ell-\xi)(-1)\phi_1(\ell) - \kappa\phi_4(\ell-\xi)(-1)\phi_2(\ell)}{\phi_4(\ell)\phi_2(\ell) - \phi_1^2(\ell)} = -\frac{\kappa(\phi_1(\ell-\xi)\phi_1(\ell) - \phi_4(\ell-\xi)\phi_2(\ell))}{\phi_4(\ell)\phi_2(\ell) - \phi_1^2(\ell)}$$

$$Q_2 = \frac{\kappa\phi_4(\ell-\xi)(-1)\phi_1(\ell) - \kappa\phi_1(\ell-\xi)(-1)\phi_4(\ell)}{\phi_4(\ell)\phi_2(\ell) - \phi_1^2(\ell)} = -\frac{\kappa(\phi_4(\ell-\xi)\phi_1(\ell) - \phi_1(\ell-\xi)\phi_4(\ell))}{\phi_4(\ell)\phi_2(\ell) - \phi_1^2(\ell)}$$

Thus,

$$w(x,t) = \frac{M_0 e^{i\Omega t}}{\kappa^3(EI + i\mu I\Omega)} \left[\kappa\phi_3(x-a)u(x-a) + \phi_4(x-a)\delta(x-a) - Q_1(a)\phi_3(x) - Q_2(a)\phi_4(x) \right] \tag{B.33}$$

where $h(x,t) = Re\{w(x,t)\}$.

Free-Free with concentrated mass:

$$\left[EI\frac{\partial^2 h}{\partial x^2}\right]_{x=0} = 0 \qquad \left[EI\frac{\partial^3 h}{\partial x^3}\right]_{x=0} = 0$$
$$\left[EI\frac{\partial^2 h}{\partial x^2}\right]_{x=\ell} = 0 \qquad \left[EI\frac{\partial^3 h}{\partial x3}\right]_{x=\ell} = 0 \tag{B.34}$$

From BCs we know that $H''(0) = H'''(0) = H''(\ell) = H'''(\ell) = 0$. From Equations (B.23) and (B.24) evaluated at ℓ we find:

$$H''(\ell,\xi) = \frac{\phi_2(\ell-\xi)}{\kappa(EI+i\mu I\Omega)} + \kappa^2 H(0)\phi_3(\ell) + \kappa H'(0)\phi_4(\ell) = 0 \tag{B.35}$$

$$H'''(\ell,\xi) = \frac{\phi_1(\ell-\xi)}{(EI+i\mu I\Omega)} + \kappa^3 H(0)\phi_2(\ell) + \kappa^2 H'(0)\phi_3(\ell) = 0 \tag{B.36}$$

The problem is again of similar form:

$$\begin{bmatrix} a & b \\ c & d \end{bmatrix} \begin{matrix} H(0) \\ H'(0) \end{matrix} = \begin{bmatrix} e \\ f \end{bmatrix}$$

Hence,

$$H(0) = \frac{fb-ed}{cb-ad} = \frac{-\frac{\phi_1(\ell-\xi)}{(EI+i\mu I\Omega)}\kappa\phi_4(\ell) + \frac{\phi_2(\ell-\xi)}{\kappa(EI+i\mu I\Omega)}\kappa^2\phi_3(\ell)}{\kappa^3\phi_2(\ell)\kappa\phi_4(\ell) - (\kappa^2\phi_3(\ell))^2}$$

$$H'(0) = \frac{ec-fa}{cb-ad} = \frac{-\frac{\phi_2(\ell-\xi)}{\kappa(EI+i\mu I\Omega)}\kappa^3\phi_2(\ell) + \frac{\phi_1(\ell-\xi)}{(EI+i\mu I\Omega)}\kappa^2\phi_3(\ell)}{\kappa^3\phi_2(\ell)\kappa\phi_4(\ell) - (\kappa^2\phi_3(\ell))^2}$$

thus,

$$H(0) = \frac{1}{\kappa^3(EI+i\mu I\Omega)} \frac{-\phi_1(\ell-\xi)\phi_4(\ell) + \phi_2(\ell-\xi)\phi_3(\ell)}{\phi_2(\ell)\phi_4(\ell) - \phi_3(\ell)^2} \tag{B.37}$$

$$H'(0) = \frac{1}{\kappa^2(EI+i\mu I\Omega)} \frac{-\phi_2(\ell-\xi)\phi_2(\ell) + \phi_1(\ell-\xi)\phi_3(\ell)}{\phi_2(\ell)\phi_4(\ell) - \phi_3(\ell)^2} \tag{B.38}$$

and from Equation. (B.19)

$$G(x,\xi) = \frac{1}{\kappa^3(EI+i\mu I\Omega)} \left[\phi_4(x-\xi)u(x-\xi) + C_3\phi_1(x) + C_4\phi_2(x)\right] \tag{B.39}$$

where

$$C_3 = \frac{-\phi_1(\ell-\xi)\phi_4(\ell) + \phi_2(\ell-\xi)\phi_3(\ell)}{\phi_2(\ell)\phi_4(\ell) - \phi_3(\ell)^2}$$

$$C_4 = \frac{-\phi_2(\ell-\xi)\phi_2(\ell) + \phi_1(\ell-\xi)\phi_3(\ell)}{\phi_2(\ell)\phi_4(\ell) - \phi_3(\ell)^2}$$

For this case:

$$H(x) = \int_0^\ell f(\xi)G(x,\xi)d\xi = \int_0^\ell (\delta'(\xi - a)M_0 + \delta(\xi - b)m_b\Omega^2)G(x,\xi)d\xi$$

hence,

$$H(x) = -M_0\frac{\partial G}{\partial \xi}(a) + m_b G(b)$$

Again, using relations in Equation (B.31) we find:

$$\frac{\partial G}{\partial \xi} = \frac{1}{\kappa^3(EI + i\mu I\Omega)}\left[\kappa\phi_3(x-\xi)(-1)u(x-\xi) + \phi_4(x-\xi)\delta(x-\xi)(-1) + Q_3\phi_1(x) + Q_4\phi_2(x)\right] \tag{B.40}$$

where,

$$Q_3 = \frac{-\kappa\phi_4(\ell-\xi)(-1)\phi_4(\ell) + \kappa\phi_1(\ell-\xi)(-1)\phi_3(\ell)}{\phi_2(\ell)\phi_4(\ell) - \phi_3(\ell)^2} = -\frac{\kappa(-\phi_4(\ell-\xi)\phi_4(\ell) + \phi_1(\ell-\xi)\phi_3(\ell))}{\phi_2(\ell)\phi_4(\ell) - \phi_3(\ell)^2}$$

$$Q_4 = \frac{-\kappa\phi_1(\ell-\xi)(-1)\phi_2(\ell) + \kappa\phi_4(\ell-\xi)(-1)\phi_3(\ell)}{\phi_2(\ell)\phi_4(\ell) - \phi_3(\ell)^2} = -\frac{\kappa(-\phi_1(\ell-\xi)\phi_2(\ell) + \phi_4(\ell-\xi)\phi_3(\ell))}{\phi_2(\ell)\phi_4(\ell) - \phi_3(\ell)^2}$$

Thus,

$$\begin{aligned} w(x,t) = {} & \frac{M_0 e^{i\Omega t}}{\kappa^3(EI + i\mu I\Omega)}\left[\kappa\phi_3(x-a)u(x-a) + \phi_4(x-a)\delta(x-a) - Q_3(a)\phi_1(x) - Q_4(a)\phi_2(x)\right] \\ & + \frac{m_b\Omega^2 e^{i\Omega t}}{\kappa^3(EI + i\mu I\Omega)}\left[\phi_4(x-b)u(x-b) + C_3(b)\phi_1(x) + C_4(b)\phi_2(x)\right] \end{aligned} \tag{B.41}$$

where $h(x,t) = Re\{w(x,t)\}$.

Fixed-End force due to caudal fin:

$$\begin{aligned} [h]_{x=0} &= 0 & \left[\frac{\partial h}{\partial x}\right]_{x=0} &= 0 \\ \left[EI\frac{\partial^2 h}{\partial x^2}\right]_{x=\ell} &= -\frac{m_c\frac{c}{2}\Omega^2}{(EI + i\mu I\Omega)}H(\ell) & \left[EI\frac{\partial^3 h}{\partial x 3}\right]_{x=\ell} &= \frac{m_c\Omega^2}{(EI + i\mu I\Omega)}H(\ell) \end{aligned} \tag{B.42}$$

From Equations (B.21),(B.23), and (B.24) evaluated at ℓ we find:

$$H''(\ell,\xi) = \frac{\phi_2(\ell-\xi)}{\kappa(EI + i\mu I\Omega)} + H''(0)\phi_1(\ell) + \frac{H'''(0)}{\kappa}\phi_2(\ell) = -\frac{m_c\frac{c}{2}\Omega^2}{(EI + i\mu I\Omega)}H(\ell) \tag{B.43}$$

$$H'''(\ell,\xi) = \frac{\phi_1(\ell-\xi)}{(EI+i\mu I\Omega)} + \kappa H''(0)\phi_4(\ell) + H'''(0)\phi_1(\ell) = \frac{m_c\Omega^2}{(EI+i\mu I\Omega)}H(\ell) \quad \text{(B.44)}$$

Which are two equations with two unknowns, of the form:

$$\begin{bmatrix} a & b \\ c & d \end{bmatrix} \begin{matrix} H''(0) \\ H'''(0) \end{matrix} = \begin{bmatrix} e \\ f \end{bmatrix}$$

Hence,

$$H''(0) = \frac{fb-ed}{cb-ad} = \frac{-\frac{\phi_1(\ell-\xi)}{(EI+i\mu I\Omega)}\frac{\phi_2(\ell)}{\kappa} + \frac{\phi_2(\ell-\xi)}{\kappa(EI+i\mu I\Omega)}\phi_1(\ell)}{\kappa\phi_4(\ell)\frac{\phi_2(\ell)}{\kappa} - \phi_1^2(\ell)}$$

$$H'''(0) = \frac{ec-fa}{cb-ad} = \frac{-\frac{\phi_2(\ell-\xi)}{\kappa(EI+i\mu I\Omega)}\kappa\phi_4(\ell) + \frac{\phi_1(\ell-\xi)}{(EI+i\mu I\Omega)}\phi_1(\ell)}{\kappa\phi_4(\ell)\frac{\phi_2(\ell)}{\kappa} - \phi_1^2(\ell)}$$

thus,

$$H''(0) = \frac{1}{\kappa(EI+i\mu I\Omega)}\frac{\phi_2(\ell-\xi)\phi_1(\ell) - \phi_1(\ell-\xi)\phi_2(\ell)}{\phi_4(\ell)\phi_2(\ell) - \phi_1^2(\ell)} \quad \text{(B.45)}$$

$$H'''(0) = \frac{1}{(EI+i\mu I\Omega)}\frac{\phi_1(\ell-\xi)\phi_1(\ell) - \phi_2(\ell-\xi)\phi_4(\ell)}{\phi_4(\ell)\phi_2(\ell) - \phi_1^2(\ell)} \quad \text{(B.46)}$$

Appendix C

Matlab code

```
% Program to determine trajectory kinematics of a prototype by
% analyzing progressive frames
% writen by Pablo Valdivia and Ani Mazumdar
% august 28 2006

clear; digCheck = 0; numFrames = 30; tempDig = 0; trajMap =
zeros(1,1); boolTraj = 0; F_width = -1; scaleFactor = 1;
F_width_known = 0.0254; %WIDTH OF FISH IN METERS
% timeArray =0:(4/30):116/30; % F=0.5 Hz
% timeArray =0:(2/30):58/30; % F=1.0 Hz
% timeArray=0:(1/30):29/30; % F=1.5 Hz
% timeArray=0:(1/30):29/30; % F=2 Hz
% timeArray=0:(1/30):20/30; % F=2.3 Hz
% timeArray=0:(1/30):23/30; % F=2.5 Hz
% timeArray=0:(1/30):25/30; % F=2.7 Hz
% timeArray=0:(1/30):29/30; % F=3.0 Hz
% timeArray=0:(1/30):29/30; % F=3.5 Hz
% timeArray=0:(1/30):29/30; % F=4.0 Hz
% timeArray=0:(1/30):29/30; % F=4.5 Hz
timeArray=0:(1/30):29/30; % F=5.0 Hz
```

```
boolVel = 1; if(size(timeArray,2) > numFrames || size(timeArray,2)
<numFrames)
    disp('TIME ARRAY IS INVALID, VELOCITY WILL NOT BE CALCULATED');
    boolVel = 0;
end
```

```
file1 = 'TB_K_F50_00.gif'; counter =1; for(count = 1:numFrames)

        tempDig = count / 10;
        tempMod = mod(count, 10) / 10;
        tempVal = tempDig - tempMod;
        file1(10) = char(tempVal+48);
        tempMod2 = mod(count,10);
        file1(11) = char(tempMod2 + 48);
        file1

        [test(:,:,1),map(:,:,1)]=imread(file1);
        I1=ind2rgb(test(:,:,1),map(:,:,1));


        J1=rgb2gray(I1);

        J1 = medfilt2(J1, [3 3]);
```

```
thresh=0.05;
BW1=edge(J1,'sobel',thresh);
if(count == 1)
    trajMap = zeros(size(J1,2),size(J1,1));
    imTemp = zeros(size(J1));
    imPre = BW1;
end

figure(1);
imshow(BW1);
boolSelect = 1;
while(boolSelect)
    disp('Create a Line Across the fattest point of the Fish, double click on
    [BWtemp, x_s, y_s] = roipoly(BW1);
    if(size(x_s,1) < 3 || size(x_s,1) > 3)
        disp('You did not select exactly 2 points, please try again');
        boolSelect = 1;
    else
        boolSelect = 0;
    end
end
x_1 = x_s(1);
x_2 = x_s(2);
y_1 = y_s(1);
y_2 = y_s(2);
boolSelect = 1

while(boolSelect)
    disp('Double Click on the Head');
    [BWtemp, x_s, y_s] = roipoly(BW1);
```

```
    if(size(x_s,1) < 2 || size(x_s,1) > 2)
        disp('You did not select exactly 1 point, please try again');
        boolSelect = 1;
    else
        boolSelect = 0;
    end
end
x_head = x_s(1);
y_head = y_s(1);
boolSelect = 1;

while(boolSelect)
    disp('Double Click on the Tail');
    [BWtemp, x_s, y_s] = roipoly(BW1);
    if(size(x_s,1) < 2 || size(x_s,1) > 2)
        disp('You did not select exactly 1 point, please try again');
        boolSelect = 1;
    else
        boolSelect = 0;
    end
end
x_tail = x_s(1);
y_tail = y_s(1);
%Calculate Pixel Width across Fish
if(count == 1)
    F_width = sqrt( (x_2- x_1)^2 + (y_2 - y_1)^2);
    scaleFactor = F_width / F_width_known; % PIXELS PER METER
end
%Calculate Midpoint of line segment
x_m = int16(abs(x_2+x_1)/2);
```

```
        y_m = int16(abs(y_2+y_1)/2);
        trajMap(x_m, y_m) = 1;
        positions(1,count) = x_m;
        positions(2,count) = y_m;

        positionsB1(1, counter) = x_tail;
        positionsB1(2, counter) = y_tail;
        positionsB1(1, counter+1) = x_m;
        positionsB1(2, counter+1) = y_m;
        positionsB2(1, counter) = x_m;
        positionsB2(2, counter) = y_m;
        positionsB2(1, counter+1) = x_head;
        positionsB2(2, counter+ 1) = y_head;

        headPos(1, count) = x_head;
        headPos(2, count) = y_head;
        tailPos(1, count) = x_tail;
        tailPos(2, count) = y_tail;

        boolTraj = 1;
        if(count >= 2)
            K=imlincomb(1,double(BW1),1,double(imPre));
            imPre = K;
        end
        counter= counter +2;

end if(boolTraj ==1)
    figure(2), imshow(~K), hold on
```

```
        plot(positions(1,:),positions(2,:),'LineWidth',2,'Color','green');

        % Plot beginnings and ends of lines
        %plot(xy(1,1),xy(1,2),'x','LineWidth',2,'Color','yellow');
        %plot(xy(2,1),xy(2,2),'x','LineWidth',2,'Color','red');

        % Determine the endpoints of the longest line segment

end totalDist = calcDist(positions(1,:), positions(2,:));


%NOW DO THE KINEMATICS
%First step, fit the trajectory data to a 3rd order polynomial
positionsM = double(positions); positionsH = double(headPos);
positionsT = double(tailPos);


p_M = polyfit(positionsM(2,:), positionsM(1,:), 1); %FIT x in terms of Y
p_H = polyfit(positionsH(2,:), positionsH(1,:), 1); p_T =
polyfit(positionsT(2,:), positionsT(1,:), 1);


a_M = p_M(1); b_M = p_M(2); a_H = p_H(1); b_H = p_H(2); a_T =
p_T(1); b_T = p_T(2);


%y_fit_Int = int16(y_fit);
%y_predict_head = a*headPos(1,:).^2 +b * headPos(1,:) + c;
%figure(5)
%hold on;
```

```
%imshow(K);
%plot(x_fit,y_fit_Int,'LineWidth',2,'Color','Red');
plot(positions(1,:), positions(2,:), '*', 'Color', 'g'); hold on;
%plot(x_fit, y_fit,'LineWidth', 4, 'Color', 'b');
plot(headPos(1,:), headPos(2,:), '*', 'Color', 'b');
plot(tailPos(1,:), tailPos(2,:), '*', 'Color', 'r');
%plot(headPos(1,:), y_predict_head, 'o', 'Color', 'b');
hold off;



%NOW WE HAVE THE TAIL AND HEAD

%CALCULATIONS FOR THE HEAD
mulNeg = 1; counter = 1; headDist = zeros(1,size(headPos,2)); for(i
= 1: size(headPos,2))

% Step 1 find x_t, y_t
    x_t = headPos(1,i);
    y_t = headPos(2,i);

% Step 2 find m_p
    m = 1/a_H;

    m_p = -1/m;

    a = 1/ a_H;

    b = - b_H / a_H;
```

```
%Step 3 solve for x_c
    polytemp = [a - m_p, b - y_t + m_p * x_t];
    x_c = roots(polytemp);

    %Step 3a Check Sign
    if(x_c > x_t)
        mulNeg = 1;
    else
        mulNeg = -1;
    end
%Step 4 Solve for y_c
    y_c = y_t + m_p*x_c - m_p * x_t;

    headDist(counter) = mulNeg*sqrt( (x_c - x_t)^2 + (y_c - y_t)^2 );
    counter = counter + 1;

end

%CALCULATIONS FOR THE TAIL

mulNeg = 1; counter = 1; tailDist = zeros(1,size(headPos,2)); for(i
= 1: size(headPos,2))

% Step 1 find x_t, y_t
    x_t = tailPos(1,i);
    y_t = tailPos(2,i);

% Step 2 find m_p
    m = 1/a_T;
```

```
    m_p = -1/m;

    a = 1/ a_T;

    b = - b_T / a_T;
%Step 3 solve for x_c
    polytemp = [a - m_p, b - y_t + m_p * x_t];
    x_c = roots(polytemp);

    %Step 3a Check Sign
    if(x_c > x_t)
        mulNeg = 1;
    else
        mulNeg = -1;
    end
%Step 4 Solve for y_c
    y_c = y_t + m_p*x_c - m_p * x_t;

    tailDist(counter) = mulNeg*sqrt( (x_c - x_t)^2 + (y_c - y_t)^2 );
    counter = counter + 1;

end


%CALCULATIONS FOR THE Middle
mulNeg = 1; counter = 1; medDist = zeros(1,size(positions,2));
medPos = double(positions); for(i = 1: size(medPos,2))

% Step 1 find x_t, y_t
    x_t = medPos(1,i);
```

```
    y_t = medPos(2,i);

% Step 2 find m_p
    m = 1/a_M;

    m_p = -1/m;

    a = 1/ a_M;

    b = - b_M / a_M;
%Step 3 solve for x_c
    polytemp = [a - m_p, b - y_t + m_p * x_t];
    x_c = roots(polytemp);

%Step 3a Check Sign
    if(x_c > x_t)
        mulNeg = 1;
    else
        mulNeg = -1;
    end

%Step 4 Solve for y_c


    y_c = y_t + m_p*x_c - m_p * x_t;

    medDist(counter) = mulNeg*sqrt( (x_c - x_t)^2 + (y_c - y_t)^2 );
    counter = counter + 1;

end
```

```
totalDist = totalDist/scaleFactor; headDist = headDist/scaleFactor;
tailDist = tailDist / scaleFactor; medDist = medDist / scaleFactor;

% disp('Total Distance Traveled in Meters');
% disp(totalDist);
% disp('Mean Head Deflection');
% headDef = mean(headDist);
% disp(headDef);
% disp('Mean Tail Deflection');
% tailDef = mean(tailDist);
% disp(tailDef);
% disp('Tail Deflections');
% disp(tailDist);
% disp('Head Deflections');
% disp(headDist);
% disp('Middle Deflections');
% disp(medDist);

figure(5)
% hold on;
% plot(timeArray, headDist, 'b');
% plot(timeArray, tailDist, 'r');
% plot(timeArray, medDist, 'g');
plot(timeArray,headDist,'b',timeArray,
tailDist,'r',timeArray,medDist,'g','LineWidth',2); grid;
title('Clear Bass F 5.0 Hz'); xlabel('Time [s]'); ylabel('Lateral
displacement [m]'); legend('Head','Tail','Mid Body');

% Program to determine the trajectory and velocity of a prototype by
```

```
% analyzing progressive frames
% writen by Pablo Valdivia and Ani Mazumdar
% august 28 2006

clear; digCheck = 0; numFrames = 3; tempDig = 0; trajMap =
zeros(1,1); boolTraj = 0; F_width = -1; scaleFactor = 1;
F_width_known = 0.0254; %WIDTH OF FISH IN METERS

% IMPORTANT STEP!!!!!!!!!!!!!!!!!!!!!!!!!!!!!!!!!!!!!!!!!!!!!!!
% ENTER TIME VALUES CORRESPONDING TO EACH FRAME (IN SECONDS)

% timeArray = [0 8.06 13.93]; % F=0.5 Hz
% timeArray = [0 4.73 7.3]; % F=1.0 Hz
% timeArray = [0 5.36 9.36]; % F=1.5 Hz
% timeArray = [0 4.76 10.46]; % F=2.0 Hz
% timeArray = [0 4.0 9.06]; % F=2.3 Hz
% timeArray = [0 4.16 8.0]; % F=2.5 Hz
% timeArray = [0 3.2 7.76]; % F=2.7 Hz
% timeArray = [0 5.6 11.1]; % F=3.0 Hz
% timeArray = [0 6.53 11.23]; % F=3.5 Hz
timeArray = [0 9.86 22.63]; % F=4.0 Hz
% timeArray = [0 2.76 7.06]; % F=4.5 Hz
% timeArray = [0 2.43 6.26]; % F=5.0 Hz

boolVel = 1; if(size(timeArray,2) > numFrames || size(timeArray,2)
<numFrames)
    disp('TIME ARRAY IS INVALID, VELOCITY WILL NOT BE CALCULATED');
    boolVel = 0;
end
```

```
file1 = 'TB_U_F40_00.gif'; for(count = 1:numFrames)


        tempDig = count / 10;
        tempMod = mod(count, 10) / 10;
        tempVal = tempDig - tempMod;
        file1(10) = char(tempVal+48);
        tempMod2 = mod(count,10);
        file1(11) = char(tempMod2 + 48);
        file1

        [test(:,:,1),map(:,:,1)]=imread(file1);
        I1=ind2rgb(test(:,:,1),map(:,:,1));


        J1=rgb2gray(I1);

        J1 = medfilt2(J1, [3 3]);


        thresh=0.07;
        BW1=edge(J1,'sobel',thresh);
        if(count == 1)
            trajMap = zeros(size(J1,2),size(J1,1));
            imTemp = zeros(size(J1));
            imPre = BW1;
        end

        figure(1);
```

```
imshow(BW1);
boolSelect = 1;

while(boolSelect)
        disp('Double Click on the Nose');
        [BWtemp, x_s, y_s] = roipoly(BW1);
        if(size(x_s,1) < 2 || size(x_s,1) > 2)
            disp('You did not select exactly 1 points, please try again');
            boolSelect = 1;
        else
            boolSelect = 0;
        end
    positions(1,count) = x_s(1);
    positions(2,count) = y_s(1);
end


 boolSelect = 1;
if(count == 2)
    while(boolSelect)
        disp('Create a Line Across the fattest point of the Fish, double cli
        [BWtemp, x_s, y_s] = roipoly(BW1);
        if(size(x_s,1) < 3 || size(x_s,1) > 3)
            disp('You did not select exactly 2 points, please try again');
            boolSelect = 1;
        else
            boolSelect = 0;
        end
    end
    x_1 = x_s(1);
```

```
            x_2 = x_s(2);
            y_1 = y_s(1);
            y_2 = y_s(2);
            %Calculate Midpoint of Line Segment
            x_m = int16(abs(x_2+x_1)/2);
            y_m = int16(abs(y_2+y_1)/2);
            trajMap(x_m, y_m) = 1;
        end

        %Calculate Pixel Width across Fish
        if(count == 2)
            F_width = sqrt( (x_2- x_1)^2 + (y_2 - y_1)^2);
            scaleFactor = F_width / F_width_known; % PIXELS PER METER
        end



        boolTraj = 1;
        if(count >= 2)
            K=imlincomb(1,double(BW1),1,double(imPre));
            imPre = K;
        end

end if(boolTraj ==1)
    figure(2), imshow(~K), hold on


        plot(positions(1,:),positions(2,:),'-.b','LineWidth',2);

        % Plot beginnings and ends of lines
        %plot(xy(1,1),xy(1,2),'x','LineWidth',2,'Color','yellow');
```

```
        %plot(xy(2,1),xy(2,2),'x','LineWidth',2,'Color','red');

        % Determine the endpoints of the longest line segment

end [avSpeed, totalDist] = calcSpeed(positions(1,:), positions(2,:),
timeArray);

disp('Total Distance Traveled in meters'); disp(totalDist /
scaleFactor); disp('Average Speed in Meters per second');
disp(avSpeed / scaleFactor);
```

Appendix D

Parts and Materials Suppliers

D.1 RC Components

- Tower Hobbies (www.towerhobbies.com): Transmitters, receivers, batteries, servos, servo horns, etc.
- Servo City (www.servocity.com): High torque servo, digital servos, miniature servos, etc.

D.2 Control Hardware

- Parallax, Inc. (www.parallax.com): Basic2 stamps, radio, inertial, proximity and temperature sensors.
- New Micros, Inc. (www.newmicros.com): PlugaPod chip, ZigBee transmitter-receiver modules, etc.
- Surveyor, Corp. (www.surveyor.com): Wireless camera.

D.3 Elastomer materials

- Innovative polymers, Inc. (www.innovative-polymers.com): IE10 and TD100-11 Polyurethane compounds.

- Quantum Silicones, LLC. (www.quantumsilicones.com): Q300 Silicone gels.
- Smooth-On (www.smooth-on.com): EcoFlex Silicone rubbers.

D.4 Sensors and Machine Elements

- NewWay Air Bearings (www.newwayairbearings.com): Vacuum preloaded air bearings.
- Renishaw (www.renishaw.com): Linear encoders.
- Omega Engineering, Inc. (www.omega.com): Tension compression miniature load cells and amplifiers.

Bibliography

[1] Autonomous Ocean Sampling Network project: http://www.mbari.org/aosn/

[2] Yuh, J., and West, M., 2001, "Underwater Robotics", Advanced Robotics, **15**(5), pp. 609-639.

[3] Bluefin Robotics, Autonomuous underwater vehicles, http://www.bluefinrobotics.com/

[4] Hydroid, Autonomuous underwater vehicles, http://www.hydroidinc.com/

[5] MIT Autonomuous underwater vehicle team: http://web.mit.edu/orca/www/

[6] Videler, J. J., 1993, *Fish Swimming*, Cahpman & Hall, London.

[7] Houssay, S. F., 1912, *Forme, Puissance et Stabilité des Poissons*, A. Hermann et fils, Paris.

[8] Breder, C. M., 1926, "The Locomotion of Fishes", Zoologica (N.Y.), **4**(5), pp. 159-297. Society for Industrial and Applied Mathematics, Philadelphia.

[9] Gray, J., 1933, "Studies of Animal Locomotion:I. The Movement of Fish with Special reference to the Eel", J. Exp. Biol., **10**(4), pp. 88-104.

[10] Barrett, D. S., Triantafyllou, M. S., Yue, D. K. P., Grosenbaugh, M. A., and Wolfgang, M. J., 1999, "Drag Reduction in Fish-like Locomotion", Journal of Fluid Mechanics, **392**, pp. 183-212.

[11] Shen, L., Zhang, X., Yue, D. K. P., and Triantafyllou, M. S., 2003, "Turbulent Flow Over a Flexible Wall Undergoing a Streamwise Travelling Wave Motion", Journal of Fluid Mechanics, **484**, pp. 197-221.

[12] Triantafyllou, M. S., and Triantafyllou, G. S., 1995, "An efficient Swimming Machine", Scientific American, **272**(3), p64.

[13] Triantafyllou, M. S., Triantafyllou, G. S., and Yue, D. K. P., 2000, "Hydrodynamics of Fishlike Swimming", Annual Review of Fluid Mechanics. **32**, pp. 33-53.

[14] Donley, J. M., and Dickson, K. A., 2000, "Swimming Kinematics of Juvenile Kawakawa Tuna (Euthynnus Affinis) and Chub Mackerel (Scomber Japonicus)", J. Exp. Biol., **203**, pp. 3103-3116.

[15] Donley, J. M., Sepulveda, C. A., Konstantinidis, P., Gemballa, S., and Shadwick, R. E., 2004, "Convergent Evolution in Mechanical Design of Lamnid Sharks and Tunas", Nature., **429**, pp. 61-65.

[16] Jayne, B. C., and Lauder, G. V., 1995, "Speed Effects on Midline Kinematics During Steady Undulatory Swimming of Largemouth Bass, Micropterus Salmoides", J. Exp. Biol., **198**, pp. 585-602.

[17] Liao, J. C., Beal, D. N., Lauder, G. V., and Triantafyllou, M. S.,2003, "Fish exploiting vortices decrease muscle activity", Science, **302**, 5650, pp. 1566-1569.

[18] Lighthill, M. J., 1960, "Note on the Swimming of Slender Fish", J. Fluid Mech., **9**, pp. 305-317.

[19] Lighthill, M. J., 1969, "Hydromechanics of Aquatic animal locomotion", A. Rev. Fluid Mech., **I**, pp. 413-446.

[20] Lighthill, M. J., 1970, "Aquatic Animal Propulsion of High Hydromechanical Efficiency", J. Fluid Mech., **44**, pp. 265-301.

[21] Lighthill, M. J., 1971, "Large-amplitude Elongated-body Theory of Fish Locomotion", Proc. R. Soc., **179B**, pp. 125-138.

[22] Lighthill, M. J., 1975, *Mathematical Biofluiddynamics*, Society for Industrial and Applied Mathematics, Philadelphia.

[23] Wu, T. Y., 1961, "Swimming of a Waving Plate", J. Fluid Mech., **10**, pp. 321-344.

[24] Wu, T. Y., 1970, "Hydromechanics of Swimming Propulsion. Part 1. Swimming of a Two-dimensional Flexible Plate at Varible Forward Speeds in an Inviscid Fluid", J. Fluid Mech., **46**, pp. 337-355.

[25] Newman, J. N., and Wu, T. Y., 1972, "A Generalized Slender-body Theory for Fish-like Forms", J. Fluid Mech., **57**, pp. 673-693.

[26] Newman, J. N., 1972, "The Force on a Slender Fish-like Body", J. Fluid Mech., **58**, pp. 689-702.

[27] Wu, T. Y., 2001, "Mathematical Biofluiddynamics and MEchanophysiology of Fish Locomotion", Math. Meth. Appl. Sci., **24**, pp. 1541-1564.

[28] Childress, S., 1981, *Mechanics of Swimming and Flying*, Cambridge University Press.

[29] Cheng, J. Y., Zhuang, L. X., and Tong, B. G., 1991, "Analysis of Swimming 3-Dimensional Waving Plates", J. Fluid. Mech., **232**, pp. 341-355.

[30] Cheng, J. Y., and Blickhan, R., 1994, "Note on the Calculation of Propeller Efficiency Using Elongated Body Theory", J. Exp. Biol., **192**, pp. 169-177.

[31] Cheng, J. Y., Pedley, T. J., and Altringham, J. D. 1998, "A Continuous Dynamic Beam Model for Swimming Fish", Phil. Trans. R. Soc. Lond., **353**, pp. 981-997.

[32] Anderson, J. M., Streitlien, K., Barrett, D. S., and Triantafyllou, M., S., 1998, "OScillating Foils of High Propulsive Efficiency", J. Fluid. Mech., **360**, pp. 41-72.

[33] Anderson, J. M., and Chhabra, N. K., 2002, "Maneuvering and Stability Performance of a Robotic Tuna", Integrative and Comparative Biology, **42**(5), pp. 1026-1031.

[34] Kumph, J. M., 2000, "Maneuvering of a Robotic Pike". MS thesis, Massachusetts Institute of Technology, Cambridge, MA.

[35] Yu, J., Tan, M., Wang, S. and Chen, E., 2004, "Development of a Biomimetics Robotic Fish and its Control Algorithm", IEEE Transactions on Systems, Man, and Cybernetics-Part B: Cybernetics, **34**(4).

[36] Read, D. A., Hover, F. S., 2003, "Forces on Oscillating Foils for Propulsion and Maneuvering", J. Fluids Struct.**17**, pp. 163-183.

[37] Bandyopadhyay, P., Donnelly, M. J., Nedderman, W. H., and Castano, J. M., 1977b, "A Dual Flapping Foil Maneuvering Device for Low-Speed Rigid Bodies", Third Int. Symp. Performance Enhancement for Marine Vehicles, Newport, RI.

[38] Czarnowski, J. T., 1997, *Exploring the Possibility of Placing Traditional Marine Vessels Under OScillating Foil Propulsion*, SM thesis, Dept. Ocean Eng., Massachusetts Institute of Technology, Cambridge, MA.

[39] Licht, S., Polidoro, V., Flores, M., Hover, F. S., Triantafyllou, M. S., 2004, "Design and Projected Performance of a Biomimetic Flapping Foil Autonomous Underwater Vehicle", IEEE Journal of Oceanic Engineering.**29**(3), pp. 786-794.

[40] Timoshenko, S., Young, D. H., and Weaver, W. Jr, 1974, *Vibration Problems in Engineering*, John Wiley & Sons.

[41] Graff, K. F., 1975, *Wave Motion in Elastic Solids*, Dover Publications, Inc., New York.

[42] Lythgoe, J., and Lythgoe, G., 1992, *Fishes of The Sea*, MIT Press, Cambridge, Massachusetts.

[43] Nelson, J., 1976, *Fishes of The World*, John Wiley & Sons.